IMAGE FUSION FOR RADIOSURGERY TREATMENTS OF ARTERIOVENOUS MALFORMATIONS

by

YANIC BERCIER

Department of Physics,
Medical Physics Unit,
McGill University, Montreal
May 2002

A thesis submitted to the
Faculty of Graduate Studies and Research
in partial fulfilment of the requirements
of the degree of Doctor of Philosophy

National Library
of Canada

Acquisitions and
Bibliographic Services

395 Wellington Street
Ottawa ON K1A 0N4
Canada

Bibliothèque nationale
du Canada

Acquisisitons et
services bibliographiques

395, rue Wellington
Ottawa ON K1A 0N4
Canada

Your file Votre référence
ISBN: 0-612-88423-6
Our file Notre référence
ISBN: 0-612-88423-6

The author has granted a non-exclusive licence allowing the National Library of Canada to reproduce, loan, distribute or sell copies of this thesis in microform, paper or electronic formats.

The author retains ownership of the copyright in this thesis. Neither the thesis nor substantial extracts from it may be printed or otherwise reproduced without the author's permission.

L'auteur a accordé une licence non exclusive permettant à la Bibliothèque nationale du Canada de reproduire, prêter, distribuer ou vendre des copies de cette thèse sous la forme de microfiche/film, de reproduction sur papier ou sur format électronique.

L'auteur conserve la propriété du droit d'auteur qui protège cette thèse. Ni la thèse ni des extraits substantiels de celle-ci ne doivent être imprimés ou aturement reproduits sans son autorisation.

In compliance with the Canadian Privacy Act some supporting forms may have been removed from this dissertation.

While these forms may be included in the document page count, their removal does not represent any loss of content from the dissertation.

Conformément à la loi canadienne sur la protection de la vie privée, quelques formulaires secondaires ont été enlevés de ce manuscrit.

Bien que ces formulaires aient inclus dans la pagination, il n'y aura aucun contenu manquant.

Canada

Abstract

An interactive 3D target localisation and delineation tool has been developed for radiosurgery planning of arteriovenous malformations (AVMs). With this system, magnetic resonance (MR), MR angiography (MRA) and computed tomography (CT) volumes can be fused in stereotactic space. Stereotactic angiography (SA) images can be linked to the MRA volume by recovering the SA acquisition geometry. The MRA and SA images can be correlated (1) by ray-tracing through the MRA volume with the recovered SA acquisition geometry and overlaying the images onto the SA images and (2) by localising the AVM onto a volume rendered representation of the MRA with a 3D cursor and projecting its position onto the SA images. Target contours can then be drawn on the MRA/MR/CT images and simultaneously projected onto the SA images.

The plans of patients who had previously undergone radiosurgery at our institution employing SA images for localisation and MR images for delineation were investigated. MRA datasets were also acquired at the time of MR scanning employing the 3D TOF technique. Some ray-traced MRA images correlated well visually with the SA images, others presented inconsistencies which suggest that MRA should be used only as complement to SA images.

The role of the different modalities (MRA, MR and SA) in the definition of target volumes is investigated by defining the target contours with different combinations of modalities within the interactive system. The target volumes drawn with different modalities were compared to a reference volume, drawn using MRA, MR and SA images, and presented underestimation and overestimation of target volumes ranging from 20% to 92% and from 3% to 40%.

The dosimetric implications of image fusion for target delineation are investigated by retrospective evaluation of the dose coverage of the reference target volume by the original treatment plan. Target coverage inferior to 60% of the reference target volumes by the original treatment plans was obtained for the patients. Treatment plan optimisation was performed to evaluate the possible dosimetric improvements resulting from image fusion for AVM target delineation. The plans were improved by employing three, eight and four isocentres for the 3 patients, and resulted in target coverage equal or superior to 98% for all three patients.

Résumé

Un outil pour la localisation et la délimitation tri-dimensionelle (3D) de cibles a été dévelopé pour la planification radiochirurgicale de malformations artérioveneuses (MAVs). Avec ce système, des volumes de résonance magnétique (RM), de RM angiographique (RMA) et de tomodensitométrie (TD) peuvent être fusionés en espace stéréotactique. Des images d'angiographie stéréotactique (AS) peuvent être liées au volume RMA en déterminant la géométrie de projection des images AS. Les images RMA et AS peuvent être corrélées (1) en simulant des projections à travers le volume RMA avec la géométrie de projection des images AS et en superposant les images simulées sur les images AS, (2) en localisant la MAV sur une représentation 3D du volume de RMA avec un curseur 3D et en projetant sa position sur les images AS. Les contours de la cible peuvent ensuite être traçés sur les images RMA/RM/TD et simultanément projetés sur les images AS.

Les plans de patients qui avaient antérieurement subit une radiochirurgie à notre institution en utilisant des images AS et RM pour la localisation et la délimitation de la cible respectivement ont été étudiés. Des images de RMA ont aussi été prises lors de l'examen RM avec la technique TOF 3D. Certaines projections de RMA simulées corrélaient bien avec les images AS, d'autres ont présenté des différences par rapport aux images AS ce qui suggère que les images RMA doivent être utilisées seulement comme compléments aux images AS.

Le rôle des différentes modalités (RMA, RM et AS) pour la définition de volumes cibles est étudié en définissant les contours de la cible avec différentes combinaisons de modalités avec le système interactif. Les volumes cibles définits avec différentes modalités ont été comparés à un volume référence, définit avec les images RMA, RM et AS, et ont présenté des sous-estimations et des sur-estimations de volumes cibles de 20% à 92% et de 3% à 40%.

Les implications dosimétriques de la fusion d'images pour la délimitation de la cible sont étudiées par évaluation rétrospective de la couverture de la dose sur le volume cible de référence par le plan original. Pour les trois patients, moins de 60% des volumes cibles de référence ont été couverts par le plan original. Les plans ont ensuite été optimisés pour évaluer les améliorations dosimétriques résultants de la fusion d'images pour la délimitation de cibles MAVs. Les plans ont été améliorés en utilisant trois, huit et quatres isocentres pour les trois patients. Avec ces plans, les cibles ont été couvertes à 98% ou plus pour les trois patients.

Original Contribution

A multimodality image fusion and interactive localisation and delineation system for radiosurgery treatments of arteriovenous malformations (AVM) has been developed. Within this interactive system, 2D stereotactic angiography (SA) images can be linked to the fused 3D MRA/MR/CT datasets by recovering the SA acquisition geometry in order to correlate the 3D and 2D datasets. The MRA and SA images can be correlated (1) by ray-tracing through the MRA volume with the recovered SA acquisition geometry and overlaying the images onto the SA images and (2) by localising the AVM onto a volume rendered representation of the MRA with a 3D cursor and projecting its position onto the SA images. Target contours can then be drawn on the MRA/MR/CT images and simultaneously projected onto the SA images.

Ray-traced MRA images, acquired with the SA projection geometry, and SA images are correlated. Our findings suggest that MRA images cannot be used as an alternative, but rather a complement to SA images. A quantitative investigation of the influence of the significance of the various modalities (MRA, MR and SA) for the interactive definition of target volumes is presented. Three patient cases are presented for which the target contours are drawn with the interactive image fusion system introduced above. Various combinations of datasets were employed for target definition and the resulting volumes were compared to the reference target volume (drawn after fusion of all datasets). Our findings present underestimation and overestimation of target volumes respectively ranging from 20% to 92% and from 3% to 40% of the target volume. The role of each modality in the target delineation process is demonstrated by quantitative analysis.

The dosimetric implications of the use of image fusion for AVM target delineation is presented. The treatment delivered to the patient was studied employing the reference target volume drawn within the interactive system with all modalities. Differences in target volume coverage and surrounding tissue sparing were evaluated employing the reference target volume. Our findings present coverage inferior to 60% of the reference target volumes by the original treatment plans for all three patients. Treatment plan optimisation was performed in order to evaluate the outcome of employing all imaging modalities for AVM target delineation within the developed system. The optimised plans present coverage equal or superior to 98% of the reference target volumes.

Acknowledgements

I would like to express my gratitude to Dr. Dimitre Hristov, my thesis supervisor, for his support and freedom provided throughout this research. He has allowed me to fulfil my thesis goals with great satisfaction.

I am truly grateful to Dr. Ervin Podgorsak for his consideration for and attention to graduate students of the Medical Physics Unit at McGill University. He has provided a challenging and rewarding environment for graduate students to pursue their research. He was also a great partner in numerous boxing rounds.

I am also very grateful to Dr. Caron, M.D., without whom the clinical results in this thesis would not have been completed. He was very patient and his time was greatly appreciated. I would also like to thank Horacio Patrocinio, M.Sc., for his help with treatment planning as well as discussions on radiosurgery in the past years. His experience in and interest for the subject were greatly appreciated. I would like to extend my appreciation to Dr. Souhami, M.D., for his expertise in clinical dosimetry.

I am also grateful to all my colleagues at the Montreal General Hospital. They provided a great amount of support, distractions and many laughs over the past years. In particular, I thank François DeBlois and Wamied Abdel-Rahman for their computer expertise. I would also like to thank Fadi, Renée-Xavière, Marylène, Kamen, Edwin, Kristin, Jennifer, Will, Tony, Alexandre and Philippe. I also thank Gennaro Durante and Nagi Sharoubim for discussions on diagnostic radiology and on corporate affairs. I also thank Margery Knewstubb and Caroline Gauvreau for their administrative help.

I would like to extend my gratitude to my parents, Françine and Jean, and my sister Karine for their love, support, patience and understanding in the past years of my graduate work. I could never thank them enough. I also thank Arie, Bart and Remy of Quo Vadis for memorable moments writing and recording music, performing shows and touring during the past ten years. I would also like to thank my extended family (grand-parents, aunts and uncles, cousins) as well as all my friends for their support.

Financial support for the research presented in this thesis was provided by the Medical Research Council of Canada and is also gratefully acknowledged.

List of Figures

List of Tables

Table of Contents

Chapter 1

Introduction

1.1 Arteriovenous Malformations

In the normal human blood circulation, the blood vessels originate from the heart and consist of a branching arrangement of arteries of continually decreasing size which feed into a capillary bed before exiting through small veins, which increase in size prior to returning to the heart. The capillary bed serves an important purpose. Its vascular resistance slows the flow of blood considerably to allow perfusion of oxygen and nutrients to surrounding tissue. In some cases, the vessels comprising the capillary bed of the brain become malformed during embryonic development and prohibit the opportunity for blood to properly perfuse into the surrounding tissue. Such malformations are termed *arteriovenous malformations* (AVMs).

There are three anatomic components of AVMs that are significant in understanding the anatomy and the treatment of the lesions: (1) the arterial feeders, (2) the nidus and (3) the venous outlow (Figure 1). The nidus represents the tangled conglomerate of weakened and enlarged capillary vessels which serve as direct shunts for blood flow between the high-pressure feeding arterial system and the low pressure draining venous system. The high flow shunting of blood within the AVM without an intervening capillary bed causes the fragile dilated vessels in the nidus to become structurally abnormal and fatigued, to enlarge further, and to possibly rupture. The size of an AVM, denoted as the maximum nidus diameter D, ranges from 1 to 10 cm. Clinical descriptions of AVM size include small ($D < 3$ cm), medium ($3 < D < 6$ cm) and large ($D > 6$ cm) [1]. Small AVMs have been shown to rupture more frequently than larger AVMs.

AVMs are present in approximately 0.14% of the population [1, 2]. Small AVMs account for 30% of the afflicted population, medium AVMs account for 60% and large AVMs account for 10% [1]. Since AVMs differ in size, location and degree of shunting, the symptoms vary (Figure 2) and become clinically apparent at different ages (Figure 3, Figure 4). Spontaneous bleeding, or hemorrhage, is the most common symptom of AVMs (50%), after which are seizures (25%) [3]. The annual risk of AVM hemorrhage is from 2 to 4% per year [4]. Once the AVM has bled, the annual risk of recurrent hemorrhage increases to 6% for the first year and increases 2% yearly for subsequent years [2]. Approximately 80% of all AVMs become symptomatic by the end of the fourth decade of life [2]. AVMs pose a significant risk and represent a major life threat when left untreated [3]. A long-term follow-up of persons

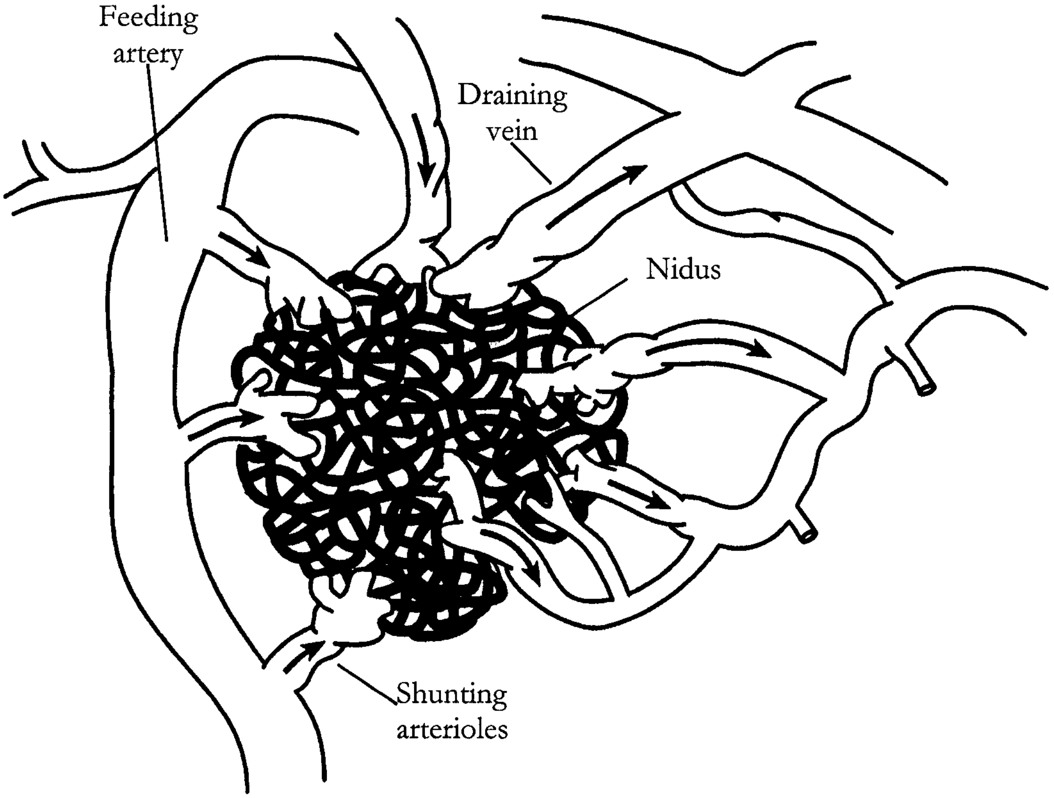

Figure 1. Schematic diagram of an AVM (with modifications from [1]). The nidus is illustrated as the tangled conglomerate of vessels.

without interventions indicates a mortality rate of 17% to 19% and a severe disability rate of 20% to 29% over a 15 year to 20 year period [3].

The main objective in treating AVMs is to remove the AVM completely and permanently [3, 5] in a way that (1) the threat of intracranial hemorrhage is eliminated, (2) neurological function is preserved and (3) complications from the treatment are avoided [6]. The three major modalities for the treatment of AVMs are surgery, endovacular embolisation and stereotactic radiosurgery (SR) [5].

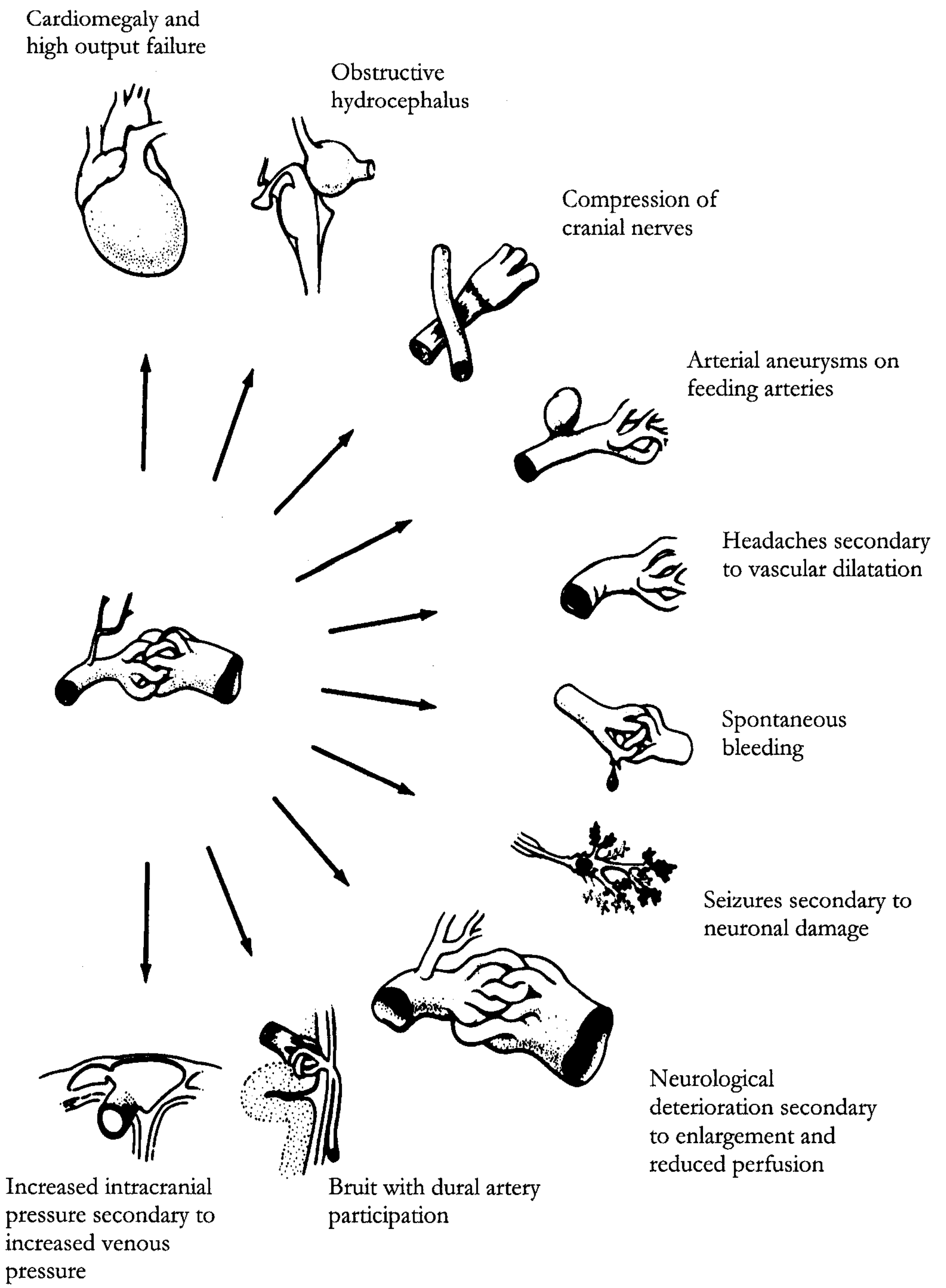

Figure 2. Principal mechanisms for neurologic symptoms of cerebral AVMs (with modifications from [2]). The AVM, illustrated in the middle, can induce a series of symptoms as pointed to by the arrows.

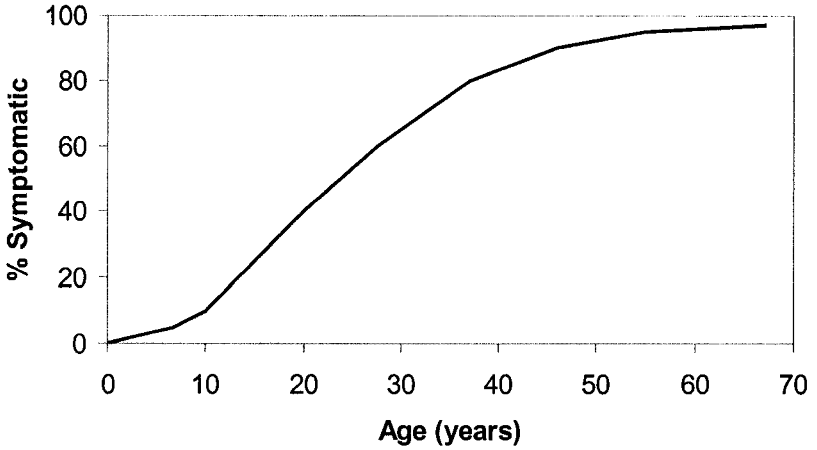

Figure 3. Percent incidence of symptoms of cerebral AVMs related to age at which they usually appear [2]. It can be seen that approximately 80% of all AVMs become symptomatic by the fourth decade of life.

In surgery, the first step in the resection of the lesion is the identification of the major arterial feeders [1]. Once the feeders are identified, the surgeon carefully dissects around the volumetric boundary of the AVM, isolating the lesion from the normal brain [1]. Surgery has the advantages of immediate protection from the risk of hemorrhage [6] and cure rates generally exceeding 95% for small AVMs [7]. However, the disadvantages remain the invasiveness of the procedure [8], the possibility of immediate complications [8], the need of general anesthesia and a lengthy recovery time [1]. The risk of treatment-related morbidity is of the order of 5% and mortality of the order of 1% [7]. For reasons including inaccessibility, size, and patient safety, some AVMs, particularly large AVMs, cannot be removed surgically and must therefore be managed by embolisation or radiosurgery.

The role of embolisation in the treatment of AVMs is reserved for problematic AVMs not readily accessible by surgery or that pose a high risk to patient safety [1]. In embolisation, a chemical or mechanical agent (embolic agent) is delivered to the AVM via the arterial feeders in an attempt to occlude the nidus and redirect blood flow to normal adjacent regions of the brain. The embolic agents, such as silicon spheres, balloons, polyvinyl alcohol, microcoils and acrylic glue [9] are selectively injected via an arterial feeder and permeate a nidus volume

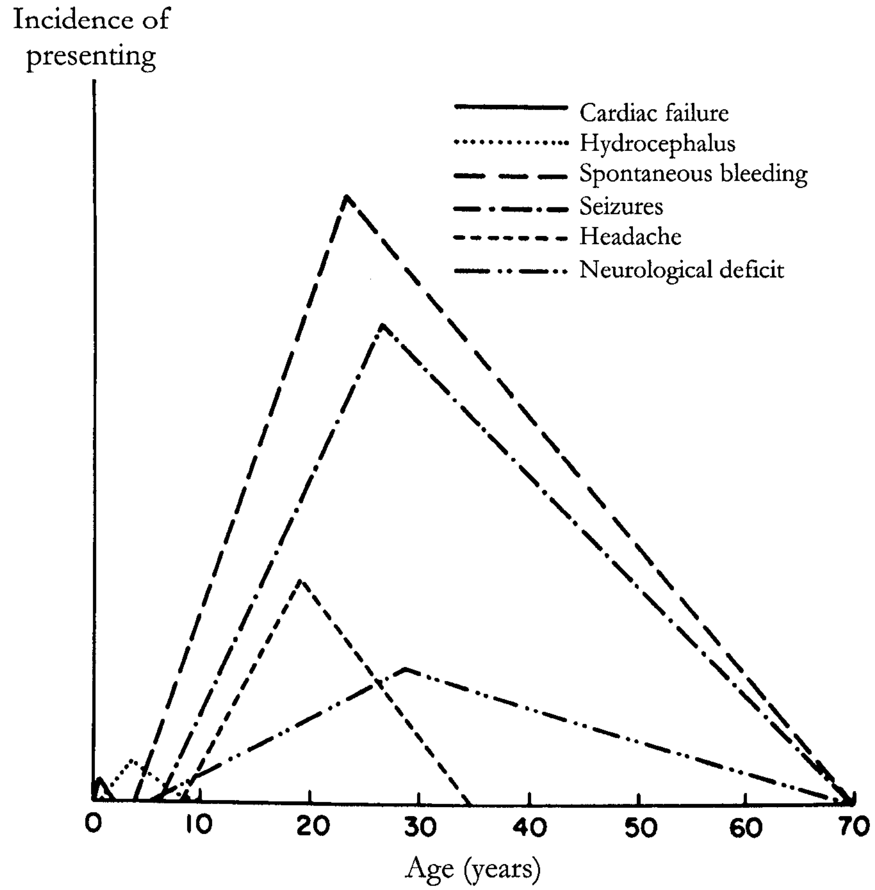

Figure 4. Estimated rate of first appearance of symptoms correlated with the age at which they appear (with modifications from [2]). It can be seen that spontaneous bleeding is the most common symptom of AVMs peaking at approximately 25 years old.

dependent on the agent volume, injection pressure and arterial flow [1]. Embolisation procedures have morbidity rates of approximately 11% and mortality rates of approximately 3.5% [3]. Some complications occur at the time of embolisation and are the result of occlusion of normal vessels by the embolic material, while others, such as hemorrhages, occur after a delay of hours to days after embolisation [3]. Unfortunately, total obliteration of the nidus is seldom achieved [3, 5] since the nidus of most AVMs contain portions that are fed by arteries not amenable to embolisation [3]. Thus, this technique is mostly performed to reduce the size or flow of the AVM in preparation for surgery or radiosurgery [3, 5].

Stereotactic radiosurgery, which is a non-invasive approach to AVM therapy [6], is a brain irradiation technique in which narrow beams of ionising radiation are focused onto a small, stereotactically localised target [10]. Its goal is to deliver a single high radiation dose to the target volume, without affecting the surrounding brain tissues [11, 12]. Successful radiosurgery requires accurate target volume determination, accurate spatial dose delivery in the target volume and a very sharp dose fall-off in regions outside the target [1, 11]. The technique is particularly useful in the treatment of areas of the brain which are inaccessible by conventional surgical means [10]. For AVMs which are situated in deep brain locations such as close to the brain stem or near critical organs such as the visual cortex, radiosurgery is especially useful due to its non-invasiveness [4]. The goal for radiosurgical treatment of AVMs is to produce an inflammatory reaction in the vessel walls of the malformation [1]. This reaction is initialised by the delivered high radiation dose which must conform to the nidus volume and exclude the adjacent draining veins and feeding arteries, keeping the target volume at a minimum [4]. Radiation injury to the AVM vessels, produced by the localised deposit of the large amount of energy into the lesion's tissue [1], causes endothelial cell damage and proliferation which leads to obliteration of the AVM [1, 4]. Complete AVM obliteration is obtained when blood flow through the AVM has ceased [1]. Radiosurgery has virtually no morbidity or disruption of the patient's life [13]. High cure rates of approximately 80% [7, 13] as well as low neurological complications of the order of 2% have been reported [13]. However, this treatment modality is progressive, indicating complete obliteration generally occurring over a latency interval of two to three years [6, 13]. Causes for incomplete AVM obliteration after radiosurgery include poor visualisation at the time of radiosurgery, which may be due to incomplete angiography [4], improper assessment of the 3D AVM shape [14, 15] as well as insufficient radiation dose delivered to the target volume [4].

1.2 Stereotactic radiosurgery procedure for AVMs

There are three main steps in the radiosurgery procedure. The first step of AVM radiosurgery is the target localisation. Conventional stereotactic angiography (SA), has been the routine method for AVM localisation [16], as well as for the determination of the nidus diameter [17]. Recent promising studies of other techniques for cerebral vascular disease localisation include the use of magnetic resonance angiography (MRA) [12, 18-22] and computed tomography angiography (CTA) [23-27]. Most studies indicate that both modalities give insufficient results to be used alone [20, 22, 24] but give complementary information [26] which, particularly for large lesions, should be employed as a complement to SA [12, 18, 25]. However, some centres, such as the University of Wisconsin Hospital and Clinics, no longer routinely perform SA before AVM radiosurgery but instead employ MRA for target localisation [12]. During all imaging and treatment procedures, a rigid frame is fixed to the patient's head establishing a coordinate system employed for the determination of the AVM position. For each modality, a series of fiducial marker plates is attached to the frame during imaging in order to determine the frame position within the image datasets. Figure 5a illustrates the SA projection geometry with the frame and localiser box.

In addition to target localisation, critical structures are localised and delineated with magnetic resonance (MR) and/or computed tomography (CT). A common method of critical structure localisation and delineation is to anatomically fuse MR to CT [28-32] in order to combine the data in a common image space. The CT volume data, employed for dose distribution calculations, is acquired with the localiser box and fused with the anatomy information provided by the MR data.

After the target and critical structures have been properly localised, the treatment planning follows. The planning is conventionally accomplished with the use of MR and/or CT datasets also acquired with the frame and modality compatible localisers. MR is particularly useful in relating the AVM to the surfaces of the brain, the ventricular system and anatomic regions of the brain such as critical organs [3]. The surfaces of the brain are employed for the determination of the AVM depth within the brain in order to calculate dose distributions. The isodose lines of the radiation distribution are employed to evaluate the effect of the plan on organs at risk near the target, which are visible on the MR and/or CT images (Figure 5b). The dose volume histogram (DVH) is a useful tool to evaluate dose distributions [33]. A (cumulative) DVH graphs the fractional volume of an organ that receives a dose greater than or equal to a specified dose. DVHs are useful in the assessment of tumor volume coverage as well as for the evaluation of the dose delivered to healthy tissue surrounding the target [33]. Since DVHs allow quantitative evaluations of treatment plans, they are employed to compare plans in order to determine the beneficial plan for the patient to be treated [33]. After a plan has decided upon, the physician prescribes the dose to be delivered to the patient.

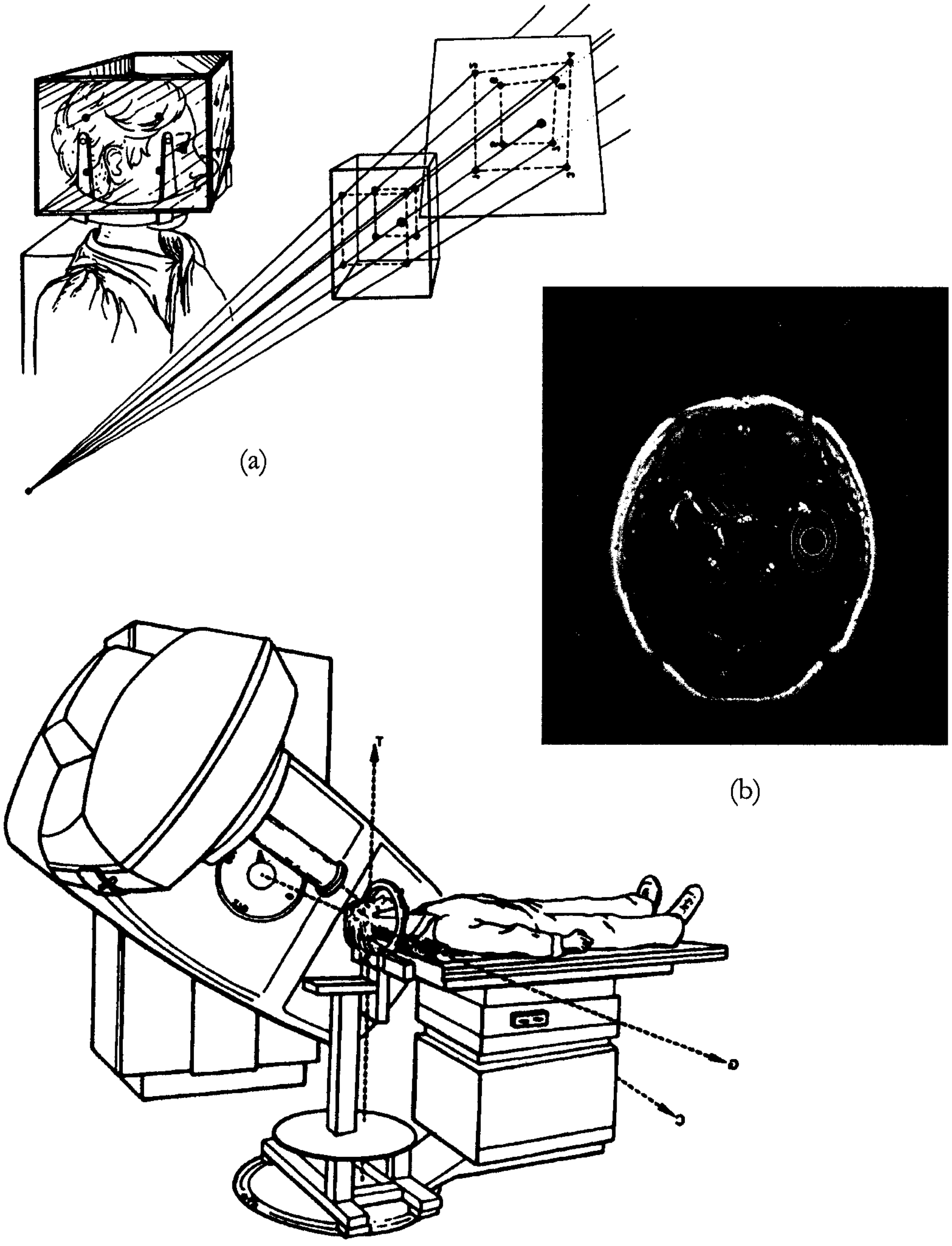

(a)

(b)

(c)

Figure 5. Three steps of radiosurgery procedure. SA projection geometry for target localisation (Step 1) is illustrated in (a) [34]. An MR image with isodose lines for treatment planning (Step 2) is shown in (b), along with the slice fiducial markers obtained from the MR compatible localiser box. Treatment delivery (Step 3) by LINAC is illustrated in (c) [34].

The final step of AVM radiosugery involves the delivery of the radiation dose. The major radiation devices include linear accelerators (LINACs) and gamma knife units [33] which deliver megavoltage x-rays and ^{60}Co gamma rays respectively [3]. Both devices require the use of a stereotactic frame. In the case of LINAC beam delivery, the patient is immobilised on the treatment couch with the target at the LINAC's isocentre (Figure 5c). Each technique, which currently include multiple non-coplanar converging arcs, dynamic stereotactic radiosurgery and conical rotation, is characterised by a particular set of individual rotational motions of the LINAC gantry and the couch from given start to given stop angles [33]. In the case of gamma knife beam delivery, the frame is secured into an appropriate collimator helmet and immobilising assembly. The couch, which advances the patient into the unit at the start of the irradiation, is retracted once the treatment time has elapsed [33].

1.3 AVM Localisation

A crucial step in the radiosurgery procedure is the AVM localisation. As mentioned previously, the modality most widely used for localisation is SA. However, CT/CTA and MR/MRA have adjunct roles because they can each offer their own unique features not present in SA.

1.3.1 SA

The necessary information for localisation with SA images is obtained by acquiring two x-ray subtraction images. During the SA procedure, a non-contrast x-ray image is acquired (Figure 6). Contrast images demonstrating the arterial and venous phases of the AVM [27] are obtained by injecting a contrast medium agent into the patient. Some of these images are chosen for subtraction from the corresponding non-contrast images (Figure 6). The location and diameter of the nidus are then determined, with the use of the orthogonal subtraction images, by a multidisciplinary medical team.

For small, spherically shaped AVMs, the modality is generally quite reliable for the delineation of the nidus [27] with anterior-posterior (AP) and lateral (LAT) projections. SA also provides useful information regarding the distribution of arterial feeding vessels and the venous drainage pattern [27]. However, since this modality presents 2D projections of 3D shapes, there are certain limitations with regard to the determination of the three-dimensional shape of

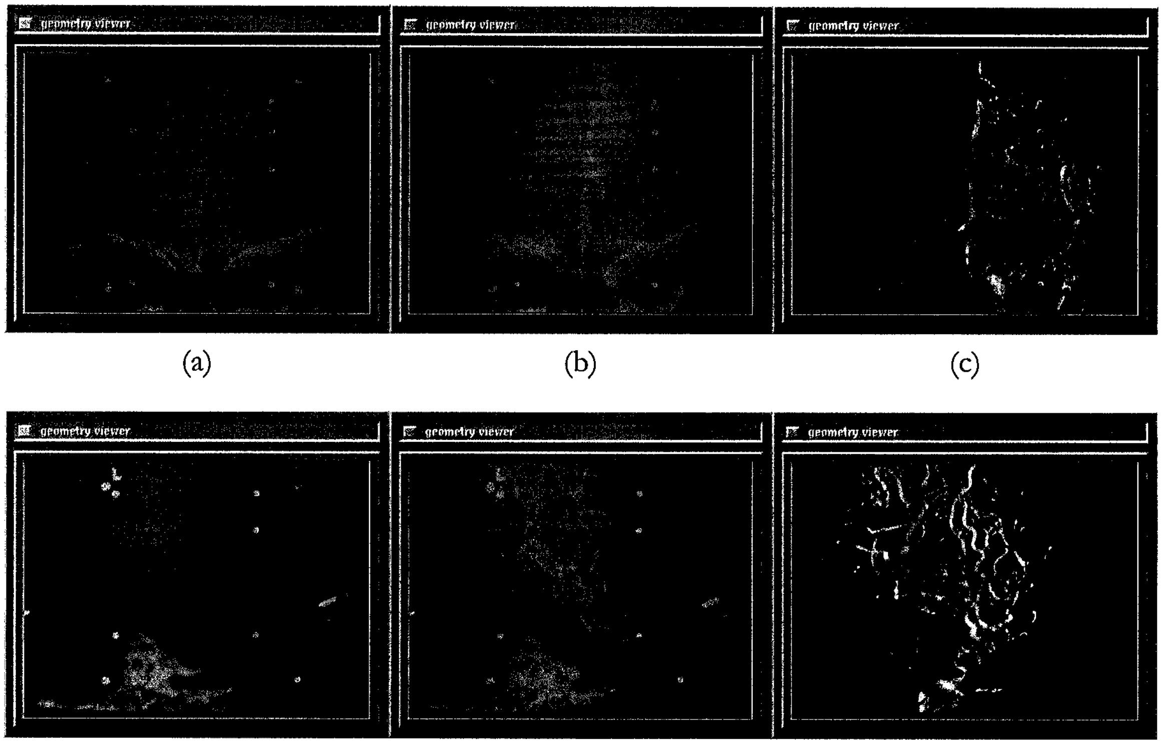

(a) (b) (c)

(d) (e) (f)

Figure 6. Orthogonal projection SA images. The non-contrast images (a) and (d), the contrast images (b) and (e) as well as the subtracted images (c) and (f) are illustrated.

large, complexly shaped or obliquely oriented AVMs [4, 12, 16, 17, 27, 35, 36], as shown in Figure 7. Another disadvantage is the invasiveness of the modality, which demands more medical personnel for the imaging. Significant changes in the target delineation can also occur since the images of the nidus on the different projections are not acquired simultaneously [17]. It is also difficult to delineate the feeding arteries, the nidus and the draining veins precisely, since they frequently fill with the contrast agent almost simultaneously and therefore they can overlap on the projected angiographic images [17].

1.3.2 CT/CTA

Another AVM localisation modality is CT. Contrary to conventional x-ray projection systems, CT provides cross-sectional tomographic images of an object. These images, which are reconstructed from x-ray projections taken at several different angles through the desired

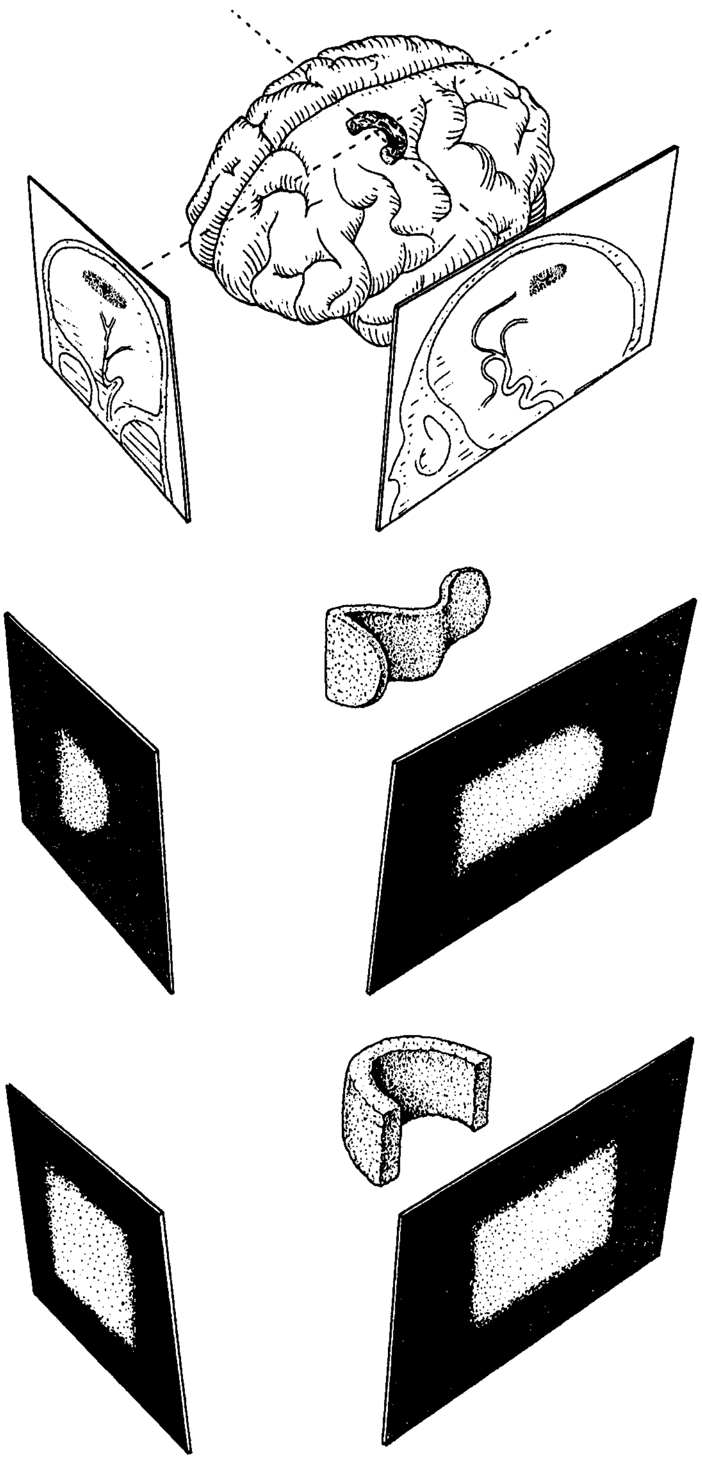

Figure 7. Irregularly shaped AVMs [17]. AVM projections for three sample shapes, as they would be seen on SA images, contain insufficient information for delineation if used alone.

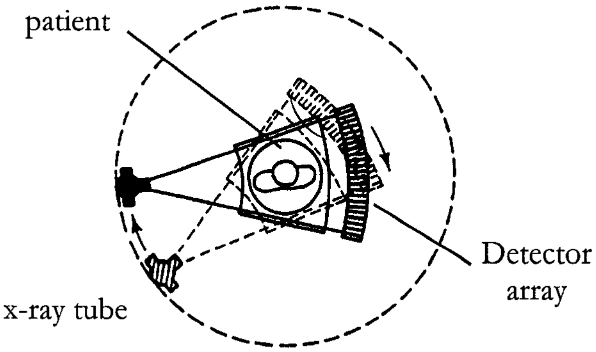

Figure 8. CT scanning geometry (with modifications from [37]). As the x-ray tube and detector array rotate, samples are taken at different angles through the object and are employed to reconstruct the images.

object slice as illustrated in Figure 8, produce a volumetric representation of the object linear attenuation coefficient [38].

Helical x-ray CT with rapid injection of contrast medium and angiographic reconstruction (CTA) is a recently developed technique [26]. The technique involves a scout scanning which is subtracted from the contrast scanning to produce angiographic data. An advantage of this modality over conventional angiography (SA) is the 3D information obtained which may be useful for large complexly shaped AVMs. CTA also has several advantages over MRA which include shorter scanning times, lower cost, better depiction of slower flow nidus and veins and availability for patients for whom MR is contraindicated [26]. CTA, contrary to SA, lacks temporal information, which is a major drawback [26]. It also involves longer post-processing time and fails to detect certain feeding arteries, presumably due to their smaller diameter compared to veins [26]. Another drawback to CTA is the invasiveness of the technique, which demands more medical personnel for the imaging.

1.3.3 MR

MR uses exterior magnetic fields, both static and in the form of time-dependent encoding gradients, and excitation radio-frequency (RF) pulses to image objects. As the magnetic field selects the slice to be imaged, RF pulses excite individual magnetised protons within the selected slice [38]. This excitation causes transitions between the nuclear spin states of the protons of the excited system [38, 39]. The system returns to equilibrium at a negative exponential rate by emitting electromagnetic quanta, the number of which is proportional to the amount of excited protons in the sample [38]. These quanta, which are detected by RF antennas, are the sampling signals employed to reconstruct MR images [38]. The reconstructed images are a function of proton density and tissue relaxation times [40] instead of linear attenuation coefficient as in x-ray modalities.

The major advantage of MR, when compared to CT, is its superior ability to differentiate and characterise soft tissues [40]. MR also has the advantage of imaging in the axial, sagittal or coronal slice orientations, unlike CT which is limited to axial images. Since there is no ionising radiation involved, no radiation dose is given to the patient. The disadvantages include longer sampling times with respect to CT as well as long post-processing times. MR is not involved in the localisation of AVMs but is particularly useful in relating the AVM to the surfaces of the brain, the ventricular system and anatomic regions of the brain such as critical organs [3]. However, MRI may yield inaccurate spatial information which may result from (1) system-related distortions, such as magnetic field inhomogeneities or gradient field nonlinearities, and (2) object-induced distortions, such as magnetic susceptibility and chemical shift artefacts [40-42] which are unique for every session [43]. Distortion effects and geometric shifts of a few millimeters have been reported [44-46]. Concerns about the geometric fidelity of MR have led to the development of distortion correction methods [42, 43, 47, 48] which have reduced global shifts to approximately 0.5 to 1 mm [41]. These distortions must be taken into consideration when imaging with this modality.

1.3.4 MRA

MRA is an MR application which provides volumetric vascular datasets allowing 3D visualisation and localisation of vascular objects. The two main techniques, which are both non-invasive, are time-of-flight (TOF) and phase contrast (PC).

The TOF technique is based on the inflow/outflow effect [49]. The MRA acquisition begins by applying many rapid RF pulses [49] that, due to the negative exponential rate of the system returning to equilibrium [39], cause the rate at which nuclei return to a steady state to decrease with each RF pulse. With fewer quanta being emitted, saturation occurs in which sampling becomes minimal [12, 50]. The flowing blood, which is also saturated, moves out of the imaging plane and fresh blood now flows into the slice [12, 50]. Another RF pulse is then triggered and a signal is received originating mostly from the fresh blood which moved into the imaging plane since the rest of the static tissue of the slice has remained saturated [12, 50] (Figure 9). The signal received, which increases with the amount of fresh blood, therefore augments as blood flow velocity increases [12, 49, 50].

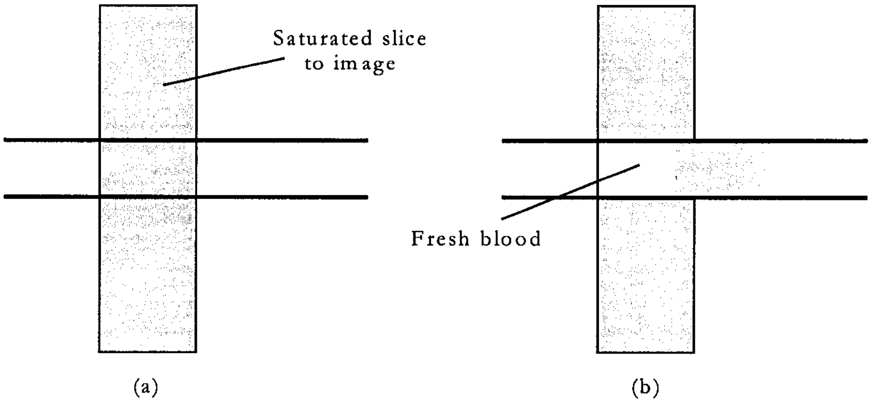

Figure 9. TOF imaging physics. The slice to be imaged becomes saturated due to the application of many rapid RF pulses, as shown in (a). The saturated blood flows out of the slice as fresh bloods flows into it, as shown in (b). Another RF pulse is applied to which only the fresh blood responds, since the static tissue of the slice has remained saturated.

There are two types of TOF imaging, the first being 3D TOF and the second being 2D TOF. The 3D TOF technique, which corresponds to volumetric acquisition, excites thick slabs of tissue to produce thin slices and therefore small voxels [50]. Volumetric sampling provides high resolution with good signal-to-noise ratio (SNR) ideal for looking at small vessels [50] and fast flow [12], such as the nidus and the feeding arteries of the AVM [12, 16]. However, the background suppression obtained by this technique is fairly poor [12]. The 2D TOF technique, which involves multiple 2D acquisitions, employs slices that are thin compared to the 3D slab thickness but are relatively thick compared to the effective 3D slice thickness [50]. Despite the poor SNR due to the thin sequential 2D slices, 2D TOF produces maximal flow/stationary tissue contrast in each slice [50]. The method is suited for acquiring data over a long segment of vessel without saturation effects and for the investigation of slow flow [50], which is particularly useful for the definition of the large draining veins of the AVM [16].

The PC technique is based on velocity-induced phase shifts [49]. This acquisition applies bipolar velocity encoding gradients along each orthogonal direction (3D) [12, 49]. As the positive portion of the bipolar gradient is applied, the stationary and moving spins accumulate a phase shift [12]. As the negative portion of the bipolar gradient is applied, the stationary spins return to their initial phase resulting in a zero phase accumulation, however, moving spins only partially return to their original phases resulting in a net phase shift [12]. Therefore, the stationary tissue remains unchanged and the signal phase of the moving blood becomes linearly proportional to the component of flow velocity in the direction of the gradient [12]. In principle, only four measurements are required: one reference with no velocity sensitivity and three sensitive to velocity along each orthogonal direction [12]. Subtraction of each velocity sensitive image from the reference eliminates the static tissue signal [50] which results in a velocity-only image for that direction [12].

There are two types of PC imaging, the first being 3D PC and the second being 2D PC. The 3D PC technique results in thin slices with excellent background suppression. The technique can provide quantitative data regarding flow velocity and direction [12]. However, the acquisition times for 3D PC are long. The 2D PC technique, on the other hand, results in a single thick section projection which is a definite disadvantage. However, the acquisition times are short and the background suppression is considered adequate.

An advantage of MRA over conventional angiography (SA) is the 3D information obtained which may be useful for large complexly shaped AVMs [26]. It also has several advantages over CTA such as the non-invasiveness of the technique and the ability to image a volume in axial, sagittal and coronal orientation. Since no x-rays are involved, no dose is delivered to the patient. However, MRA lacks temporal information, which is not the case with the SA images [26]. Since the anatomical data of MR and the vascular data of MRA provide important complementary information, MR techniques have assumed a growing role in AVM treatment planning [12].

1.4 Dynamic stereotactic radiosurgery

After the AVM has been localised, a treatment plan must be determined for the chosen dose delivery technique. Dynamic stereotactic radiosurgery, developed by Podgorsak *et al.* [11], is the treatment technique employed at the McGill University Health Centre, as well as at many other centres worldwide [33], and is therefore described in this section. The technique employs an isocentric linac with the patient positioned in the supine position on the treatment couch, as shown in Figure 5 [33]. A circular cone is attached to the LINAC head in order to produce a circular radiation beam [33]. The frame is secured to the couch allowing the gantry and couch to continually rotate simultaneously during treatment [33]. The gantry rotates 300° from $\theta_{initial} = 30^\circ$ to $\theta_{final} = 330^\circ$, while the couch rotates 150° from $\phi_{initial} = 75^\circ$ to

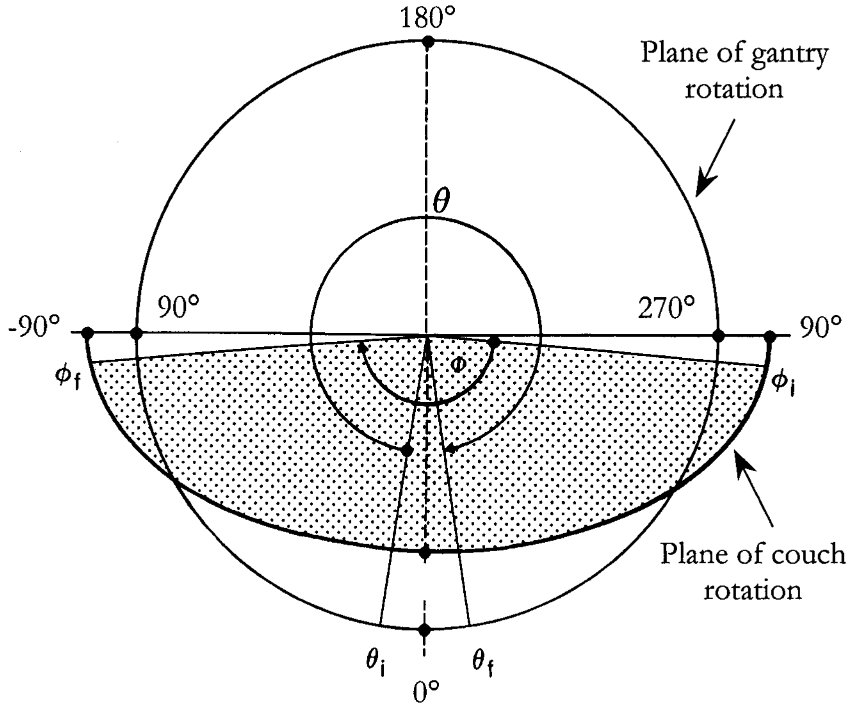

Figure 10. Schematic representation of gantry and couch motion (with modifications from [11]). The gantry angle is θ and the couch angle is ϕ. The gantry and couch rotate simultaneously and continuously, the gantry from $\theta_{initial} = 30^\circ$ to $\theta_{final} = 330^\circ$ and the couch from $\phi_{initial} = 75^\circ$ to $\phi_{final} = -75^\circ$ [11].

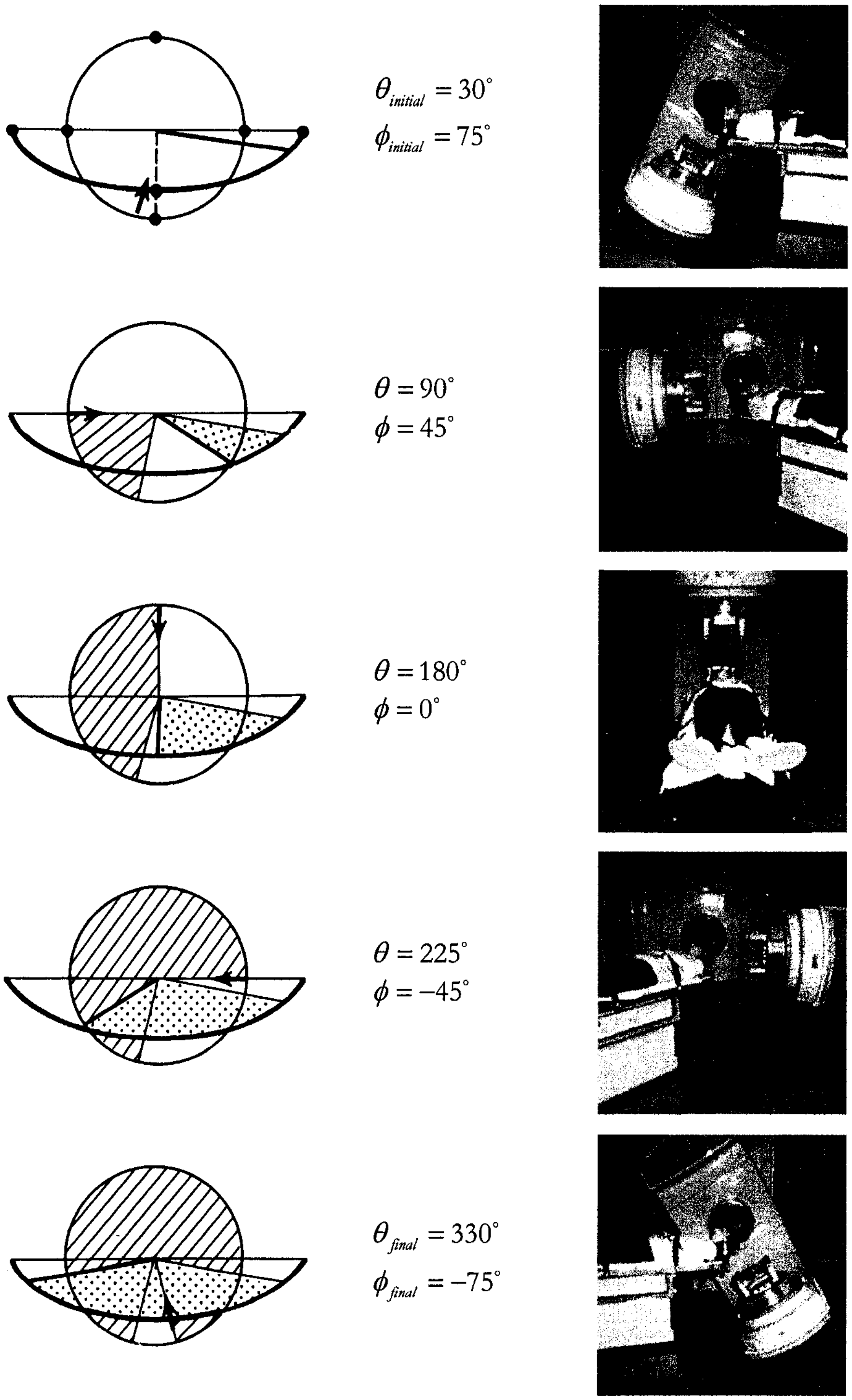

Figure 11. Several positions of linac and couch during the dynamic radiosurgery treatment (with modifications from [11]). The gantry angle θ and couch angle ϕ are defined in Figure 10.

$\phi_{final} = -75^{\circ}$ [11], as shown in Figure 10 and Figure 11. Therefore, to each degree of couch rotation corresponds to two degrees of gantry rotation [33]. The beam entry trace on the patient's head is similar to that of a baseball seam, as shown in Figure 12 [33].

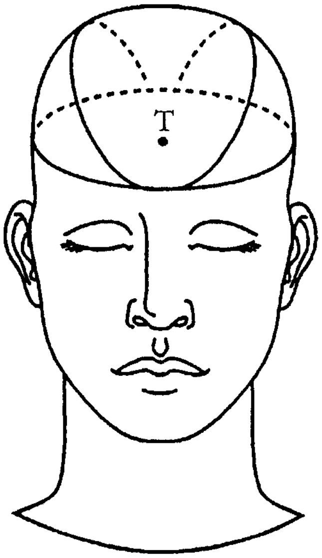

Figure 12. Beam entry points on patient's skull for dynamic radiosurgery (with modifications from [33]). The target is denoted as T. As can be seen, the trace resembles that of a baseball seam [33].

1.5 Available techniques for AVM localisation and delineation

Several methods have been developed for vascular lesion localisation and delineation. The techniques introduced by Tercier *et al.* [51] enable delineation of the target on the CT anatomical volume and projection of the target contours onto the SA images, and vice-versa, for correlation with the target extent on the SA images [51]. However, the method lacks in providing consistency checks between the vascular volumes and the SA projections prior to the contour projection onto SA images or backprojection into the anatomical volumes. Inconsistencies between the datasets may arise from MR distortions, frame slippage or other image artefacts. Considerable inconsistencies may result in excluding the vascular volume from the localisation and delineation process and therefore consistency checks are an important step of the localisation and delineation process. Certain techniques, such as parallel ray-tracing [19, 20, 52-54] as well as parallel [55] and perspective [56, 57] volume rendering of vascular volumes at different angles, have been performed in order to get additional information and to compare the MRA volume to the SA images. However, since these projections are not performed with the SA projection geometry, the SA images and projected MRA/CTA images cannot be easily correlated in order to detect inconsistencies. Projection simulations with SA projection geometry have been performed for the purpose of neurosurgery planning with tomographic anatomical volumes [58] and for the purpose of radiosurgery planning for patient alignment verification [59, 60]. However, they do not employ vascular volumes for 3D target delineation and therefore do not provide consistency checks between such volumes and SA images as part of the treatment planning.

Several studies on the use of MRA for AVM radiosurgery planning with the techniques mentioned above have been conducted [18, 61-68]. Of these studies, some groups [61, 67, 68] performed a qualitative comparison of MRA and SA for AVM localisation. Other groups [63, 65, 66] compared MRA techniques to SA by estimating AVM target volumes. Other groups [18, 62, 64] have studied the dosimetric implications of using MRA for treatment planning.

1.5.1 Qualitative comparison of MRA and SA for AVM localisation

Petereit *et al.* [61] compared nidus volumes obtained from 2D PC, 3D TOF MRA and SA images. PC MRA was acquired at five different flow velocities in order to obtain images which selectively demonstrate arterial and venous components of the AVM. 2D PC was preferred over TOF to estimate flow velocity due the latter's insensitivity to slow flow. The velocity estimation of PC MRA was correlated to that of SA. 3D TOF was acquired for nidus volume estimation since TOF has higher spatial resolution than does PC MRA. Their conclusions were that 2D PC and 3D TOF MRA are equal or superior to SA for flow velocity estimation visualisation of the nidus respectively.

Farb *et al.* [68] compared contrast-enhanced MR images to 3D TOF MRA and SA images. The contrast-enhanced MR images include the injection of a contrast media in order to obtain both anatomical and vascular information in a single dataset. Perspective and parallel projections were obtained at 15° increments over 180°. Neuroradiologists graded the contrast-enhanced MR and TOF MRA as poor, moderate or equivalent as compared to SA images, for the depiction of the feeding arteries, the nidus and the draining veins. In most cases, the TOF images were graded as poor in comparison to the SA images, whereas the contrast-enhanced MR images were graded as equivalent to SA images. Particular difficulty in determining the size of the nidus was found when using TOF MRA.

Dobson *et al.* [67] compared 2D TOF and 2D PC MRA images to SA images to define the appearance of AVMs. Their results showed that MRA demonstrated major feeding vessels and multiple intra-lesional vessels in all AVMs. However, a lack in detail demonstration of the feeding vessels was found. The 2D TOF images displayed a confusing superposition of multiple arteries and draining veins. More selective definition can be obtained from 2D PC, however, this technique is more time consuming and the authors find it to have little extra diagnostic benefit.

1.5.2 AVM target volume estimates by comparison of MRA and SA

Essig *et al.* [66] compared dynamic tagging MRA (dMRA), which demonstrates time-dependent flow through the AVM, to 3D TOF MRA as well as to SA by estimating AVM target volumes. The two MRA techniques were compared to SA in order to evaluate their usefulness. Out of twenty patients, dMRA was assessed for twelve patients. In five patients, dMRA could not be evaluated because of susceptibility artefacts due to steel screws and pins on the stereotactic frame. In these patients, the quality of TOF MRA was between good and moderate. In another three patients with a nidus diameter smaller than 1 cm, dMRA failed to demonstrate the nidus because of limitations of spatial resolution. In two of these patients, TOF MRA was not able to demonstrate the nidus. Of the twelve patients which had dMRA and TOF MRA, dMRA was found to be superior to TOF MRA in the detection and localisation of the AVM nidus for only four patients. They concluded that dMRA can demonstrate AVM characteristics reliably for AVMs larger than 1 cm and that this technique is superior to TOF MRA.

Mukherji *et al.* [65] compared the sensitivity of magnitude contrast (MC) MRA to gradient-echo (GRE) MR to SA by comparing estimates of target volumes. For the MC technique, projection images as well as source images, which are images of a volume reconstructed from the projection images, were compared to GRE and SA images. Out of thirty-three patient cases diagnosed with SA images, the sensitivity of the projection, source and GRE images to detect large AVMs (diameter larger than 1 cm) was 95%, 100% and 100% respectively. For small AVMs (diameter smaller than 1 cm), the sensitivity was 27%, 50% and 67% respectively. The authors concluded that GRE MR and MC MRA images reliably demonstrate AVMs larger than 1 cm.

Warren *et al.* [63] compared target volumes defined by SA to those defined with three MRA methods: 1) an MR-SA technique, 2) a contrast-enhanced (CE) TOF technique and 3) a non-CE TOF technique. The MR-SA technique involved the acquisition of a single thick slice between 6 and 10 cm which is subtracted from a second single thick slice obtained with injection of contrast. For the MRA techniques, AVM size was measured in all three directions. The AVMs were awarded scores depending on the largest size measured and the scores were compared to the other techniques. Of forty patients, CE MRA proved to be the most reliable and accurate of the three MRA techniques for AVM nidus size. The sensitivity for correct AVM score was 97.6%, 92.7% and 82.9% for CE MRA, MR-SA and non-CE MRA techniques respectively. The authors concluded that CE MRA offers significant advantages for AVM target volume definition but that SA x-ray images remain to be the standard for vascular imaging.

1.5.3 Dosimetric implications of using MRA for treatment planning

Bednarz *et al.* [18] conducted a twenty-two patient study in which nidus contours drawn on the SA images were backprojected onto the TOF MRA images and vice-versa. Radiosurgery treatment plans were designed based on SA, and modified accordingly, employing the information provided by the TOF MRA. In 12 cases, the initial treatment plans were modified after including MRA in the treatment planning process. The mean coverage of the MRA nidus by the SA-based plans was 93% with a mean nidus volume of 2.4 cm^3. In two of the twelve cases, MRA revealed irregularly-shaped nidi which correlated well with SA and showed that the SA-based acceptable plans undertreated 27% of the MRA nidus for the first case and 18% for the second. In the remaining ten cases, TOF MRA did not demonstrate the nidus due to surgical clip artefacts and presence of embolisation glue. The results suggested that MRA alone could not be used for AVM radiosurgery.

Ehricke *et al.* [62] compared treatment plans based on MRA alone and SA alone by delineating the target on MRA images and projecting the contours onto sagittal, axial and coronal parallel projections through the MRA volume. They reported that their MRA based approach allowed accurate delineation of target vasculature, but that SA provides additional information such as arterial and venous flow.

Kondziolka *et al.* [64] evaluated the treatment plans of twenty-eight patients obtained with contrast-enhanced (CE) TOF MRA and SA. The treatment plans were optimised employing the MRA images, and the isodose lines were projected onto the SA images in order to correlate them with the target extent on the SA images and the plans were modified accordingly. In twenty-four patients, the MRA plans fit the SA defined nidi and were therefore found to be acceptable. In sixteen patients, the MRA images provided additional information not present on the SA images. In three patients, in which SA overestimated the size of the nidus, the MRA-based plans were found to be superior to the SA-based plans. Dose volume histograms (DVHs) were not computed independently for MRA versus SA plans for a quantitative comparison and therefore, the plans were judged to be acceptable by visual inspection. Since MRA provides 3D information not presented in SA, multiple isocentres were necessary to increase the dose conformity. The number of isocentres ranged between two and ten. AVMs appeared more spherical on the SA images and often were irradiated with one or two isocentres.

1.5.4 Drawbacks of previous methods

The studies mentioned above [18, 61-68] compared MRA and SA images for AVM radiosurgery planning, however, they contain many drawbacks.

1. No direct vasculature correlation was performed as part of the planning in order to provide consistency checks between the datasets. Inconsistencies between the MRA and SA datasets may arise from MR distortions, frame slippage between or during image acquisitions, or other image artefacts, which, if detected, may result in significant modifications to the treatment plan.

2. The technique of drawing contours on the SA images and backprojecting them into the MRA volume does not allow the physician to interactively correlate the datasets and

modify the contours as they are drawn, and cannot always completely reconstruct non-convex volumes [51], which may result in contours that contain appreciable amounts of normal tissue [59, 60].

3. In some of the above studies [18, 61, 62], target volumes were not delineated using different combinations of modalities in order to evaluate the influence and importance of each modality for the target delineation process. The target volume was determined for each imaging technique and compared to that obtained from the other techniques and therefore, image fusion was not included in the studies.
4. The treatment plan studies mentioned above only gave qualitative results since plans were judged to be acceptable only by visual inspection. A thorough evaluation of the treatment plans by computation of DVHs was not performed.

1.6 Thesis objectives and outline

The aim of this project was to correlate MRA, MR and SA for radiosurgery treatments of AVMs. The objectives were:

1. To develop an image fusion and localisation system for radiosurgery treatments of AVMs in order to correlate MRA, MR and SA during target localisation and 3D delineation.
2. To study the effect of the use of image fusion with multiple modalities on the definition of target volumes for patients who had previously undergone radiosurgery for AVMs.
3. To replan patients which had previously undergone radiosurgery for AVMs with the target volumes obtained from the system in order to quantify the dosimetric implications of the difference in target volumes.

The thesis is organised as follows.

Chapter one has given an introduction on AVMs and stereotactic radiosurgery. Imaging modalities for localisation of AVMs were also discussed.

In the second chapter, the principles and functionality of an interactive image fusion and localisation system are presented. The system provides tools for volume fusion as well as methods for the correlation of 3D and 2D datasets for 3D target localisation and delineation. Within this system, MRA/MR/CTA/CT volumes are first fused. The SA projection geometry is then recovered in order to link the 3D datasets to the 2D images. The MRA and SA images are then correlated (1) by ray-tracing through the MRA images with the SA projection geometry and overlaying the images onto the SA images and (2) by delineating target in the MRA (or MR/CTA/CT) volumes and simultaneously projecting the contours onto the SA images. The results of an experiment with a specially designed phantom for system validation are presented.

Chapter three presents examples of 2D SA MRA correlation.

Chapter four presents a study on the effect of using multiple imaging modalities on the definition of target volumes. Within the system, target contours were drawn employing different combinations of imaging modalities in order to quantify the differences in target volumes. Target contours were drawn employing (1) MR, (2) MR and SA, (3) SA, (4) MR and MRA and (5) MR, MRA and SA.

The fifth chapter presents an evaluation of the treatment delivered to patients who had previously undergone radiosurgery. The delivered treatment was evaluated using the target volumes determined with MR, MRA and SA images in the previous chapter. The dosimetric implications of the difference in target volumes, due to the use of the 3D information of the interactive system, were evaluated and quantified by the computation of DVHs.

The sixth chapter concludes the thesis by summarising the work presented in this thesis as well as by discussing future research directions.

Aspects of this work have been published in conference proceedings [69-71].

Chapter 2

Image Fusion and Localisation System

2.1 Introduction

This chapter presents the software developed for image fusion and localisation of AVMs for radiosurgery. The software supports both the Leksell and Olivier-Bertrand-Tipal (OBT) stereotactic coordinate system commonly used for radiosurgery and neurosurgery, respectively. Both coordinate systems, which are established by fixing a rigid frame to the patient's head during all imaging procedures and the radiosurgery treatment (Figure 13) and identify all points within the frame coordinate space. The frame also provides a rigid base for immobilisation of the patient during imaging and treatment procedures. Fiducial marker plates exist for each modality and are attached to the frame during imaging in order to determine the frame position within the datasets. In the examples of the following sections, the Leksell frame is employed, however, the methods are similar for the OBT frame.

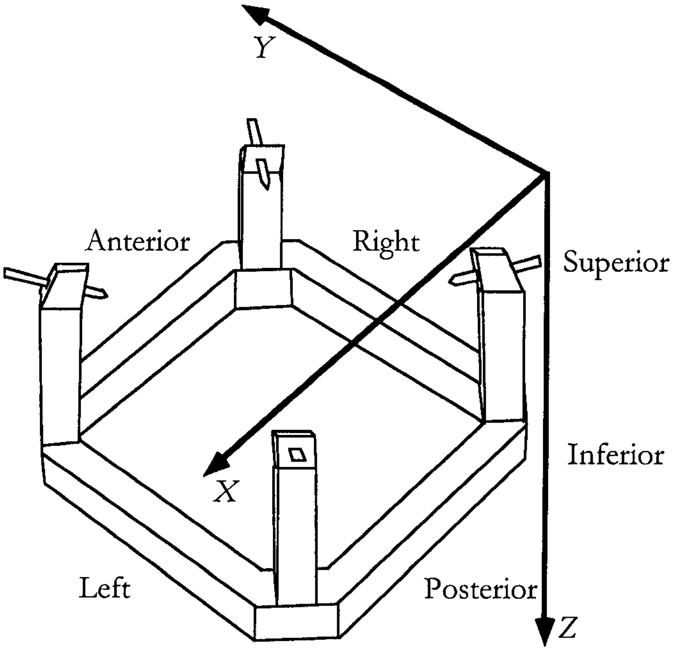

Figure 13. The Leksell stereotactic frame with posts and pins for head attachment. The convention for the coordinate system is depicted with the centre of the frame located at 100 mm from the origin along all three axes.

The three main modules of the software are illustrated in Figure 14. The Volume Registration and Reformatting module fuses the MRA/MR/CT volumes. From a pair of SA images, the SA Projection Geometry Determination module determines the perspective projection geometry for the SA acquisition. The Correlation module correlates the datasets in the following steps. In the first step, MRA and SA data is correlated by ray tracing through the MRA volume and overlaying the SA and ray-traced MRA projection images. The datasets can also be correlated by backprojecting the contours, drawn on SA images, into the MRA volume. Target localisation and 3D delineation is then performed within the MRA/MR/CT volumes with feedback from the simultaneous contour projections onto the SA images.

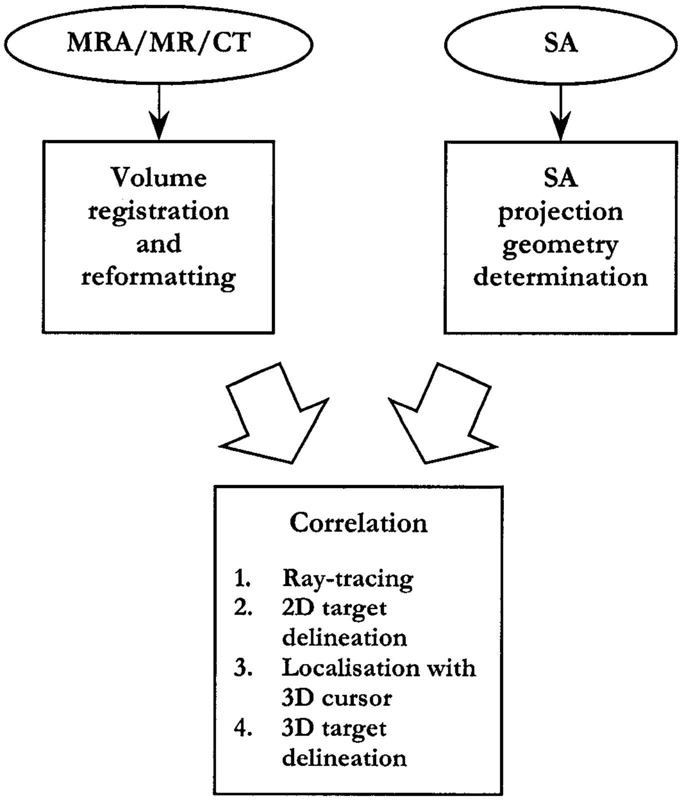

Figure 14. Three main modules of system.

2.2 Volume registration and reformatting

In order to fuse the 3D datasets, the images are registered and reformatted in stereotactic space defined by the stereotactic frame.

2.2.1 Registration

Image registration is executed to determine the image location and orientation in frame space and is performed by generating slice dependent frame transformation matrices $(FTM)_s$ which convert image coordinates (u,v) of slice s to frame space coordinates (x,y,z) [58].

$$\begin{bmatrix} x & y & z \end{bmatrix} = \begin{bmatrix} u & v & 1 \end{bmatrix} \cdot (FTM)_s \tag{1}$$

The $FTMs$ are calculated in the following way. The CT and MR localisers contain a set of N-shaped bars (Figure 15a). The Leksell frame space coordinates of the vertical rods are given in Figure 15b. The N-shaped bars, when imaged axially, give three collinear image points. With three bars on each frame attachment, nine points are obtained on each image (Figure 16). The nine markers are selected by the user and are defined in image space coordinates as (u_i, v_i), where $i \in \{1,2,...,8,9\}$.

The 3D frame space coordinates (x_i, y_i, z_i) of the middle fiducial marker of each N-shaped bar cross-section are determined using ratios with respect to the extremity markers (Figure 17) [58, 72]. The frame space coordinates of the three middle fiducial markers (x_1, y_1, z_1), (x_2, y_2, z_2) and (x_3, y_3, z_3), along with their corresponding image coordinates (u_1, v_1), (u_2, v_2) and (u_3, v_3), are used to determine the frame transformation matrix FTM. From Eq. (1), the FTM of slice s, $(FTM)_s$, is obtained by the following equation [58].

$$(FTM)_s = \begin{bmatrix} u_1 & v_1 & 1 \\ u_2 & v_2 & 1 \\ u_3 & v_3 & 1 \end{bmatrix}^{-1} \begin{bmatrix} x_1 & y_1 & z_1 \\ x_2 & y_2 & z_2 \\ x_3 & y_3 & z_3 \end{bmatrix} \tag{2}$$

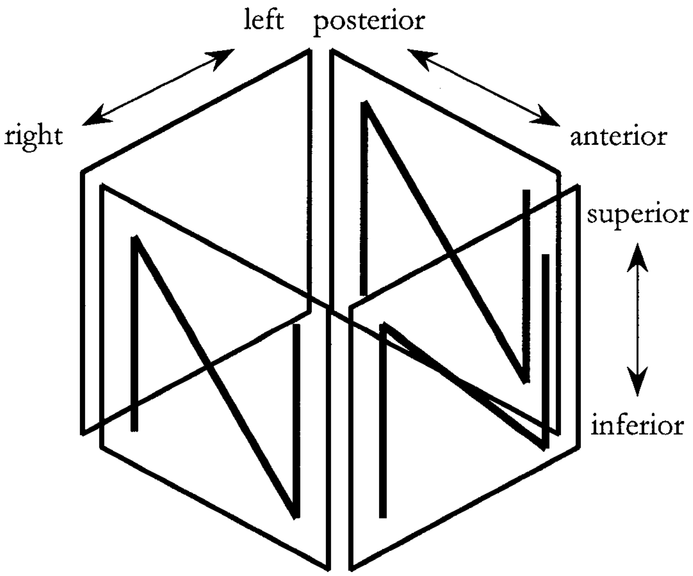

(a)

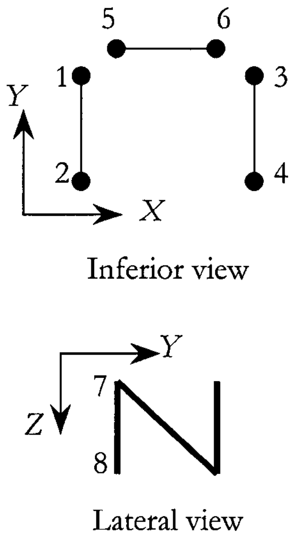

Point	x (mm)	y (mm)	z (mm)
1	5	160	---
2	5	40	---
3	195	160	---
4	195	40	---
5	40	215	---
6	160	215	---
7	---	---	40
8	---	---	160

(b)

Figure 15. Leksell MR/CT localiser. The N-shaped bars on the localiser box are illustrated in (a). The frame space coordinates of vertical rods are given in (b).

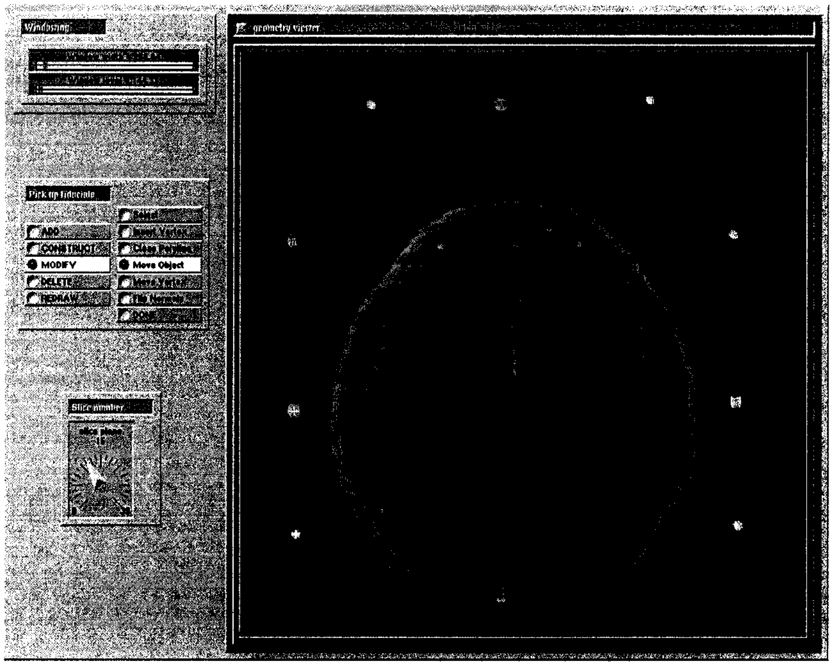

Figure 16. Panel for fiducial marker selection. The nine fiducial markers can be observed on the image slice.

2.2.2 Volume reformatting

After registration, the 3D datasets are fused by reformatting the datasets in frame space. Reformatting is necessary in our implementation in order to obtain the regular voxel array required for ray-tracing in the first step of the Correlation module.

With voxel sizes (v_x, v_y, v_z) in millimetres supplied by the user, a regular voxel array is built by interpolation for each dataset. A common reformatting extent in stereotactic space is used for all datasets to be reformatted. The intensity of each voxel (i, j, k) is interpolated from the pixel values of the slices of the original dataset and the *FTMs* of these slices. For each voxel (i, j, k) within the reformatting extent, which correspond to (x_i, y_j, z_k) in frame space coordinates, the nearest two slices that bracket the voxel, shown in dotted format in Figure 18, are determined. This is accomplished in two steps.

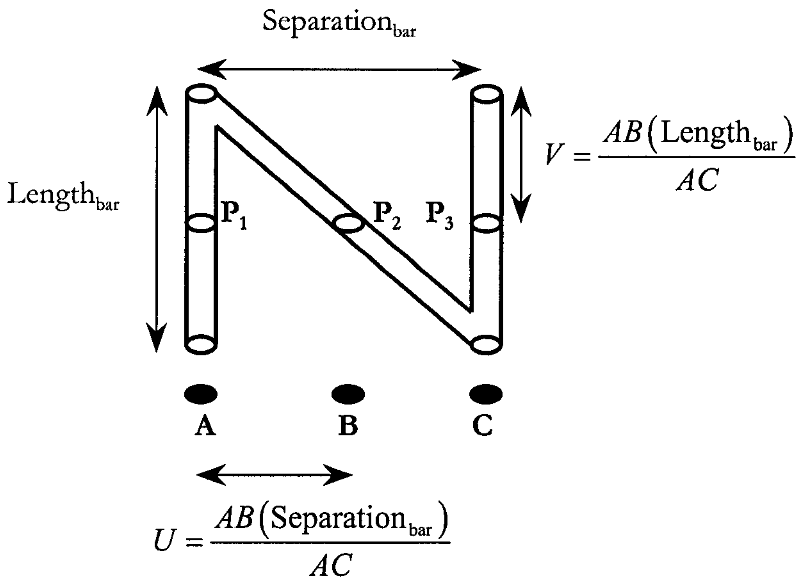

Figure 17. MR/CT fiducial marker geometry. The relative position of the middle fiducial marker of the N-shaped bar cross-section between the vertical bars allows the determination of the image slice orientation within the coordinate system defined by the frame. P$_1$, P$_2$ and P$_3$ are the points of intersection of the image plane with the rods. A, B and C are the position of the points of intersection on the image. Length$_{\text{bar}}$ and Separation$_{\text{bar}}$ are the bar length and bar separation in frame space. V denotes the distance along the Z axis between the middle fiducial marker and the rod extremity. U denotes the distance along X or Y (depending on the localiser box face) between the middle fiducial marker and the rod extremity.

1. For each slice s, the image coordinates (u_s, v_s) of the intersection of the slices with the line parallel to the Z axis passing through (x_i, y_j) in frame space are determined employing the first two equations of the system described by Eqs. (1) and (2).

$$x_i = u \cdot (F_{11})_s + v \cdot (F_{21})_s + (F_{31})_s \qquad (3)$$

$$y_j = u \cdot (F_{12})_s + v \cdot (F_{22})_s + (F_{32})_s \qquad (4)$$

The above system of two equations is therefore employed to solve for the two unknowns u_s and v_s.

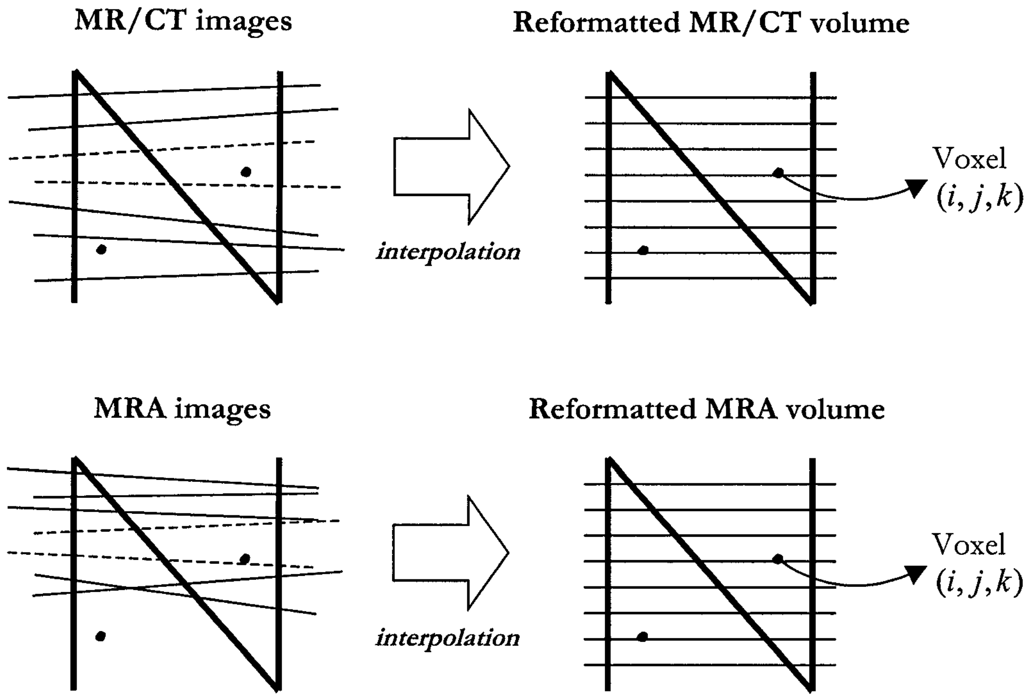

Figure 18. Slice orientation in frame space before and after reformatting (interpolation). The image slices may be arbitrarily oriented in frame space due to subtle patient movement or scanning imperfections. After reformatting, a regular voxel array is obtained. For voxel (i,j,k), the nearest two slices which bracket the voxel are illustrated in dotted format. Points, which are not between two slices, are padded with zeros.

2. From Eq. (1), the z_s value corresponding to the image coordinates (u_s, v_s) obtained in (1) above, is determined for each slice s.

3. By comparing the z_s values of the (u_s, v_s) coordinates, the slices that bracket the voxel (x_i, y_j, z_k) are determined (Figure 19).

The interpolation proceeds as follows.

1. Since the image coordinates obtained in (1) above do not directly correspond to a pixel node, as shown in Figure 19, the intensity at the image coordinates is obtained by performing a 2D bilinear interpolation [73] between the four surrounding pixels (Figure 19).

2. The voxel intensity is then determined by performing a linear interpolation [73] along Z, using the distances between the slices and the voxel (Figure 19).

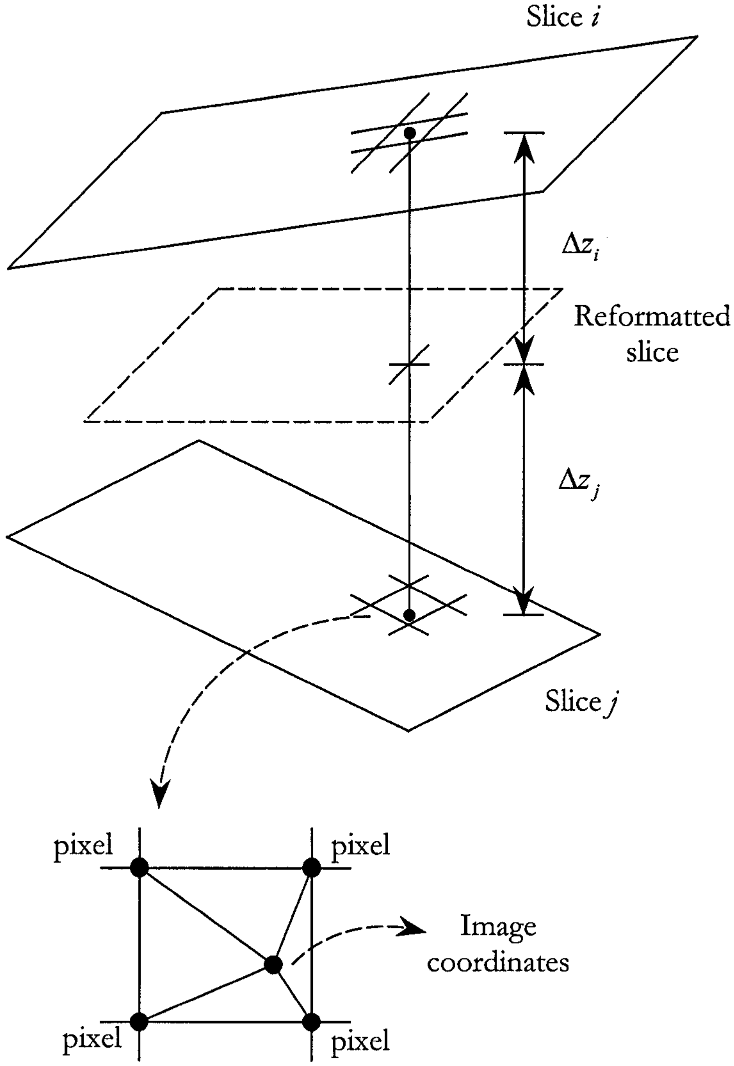

Figure 19. Interpolation procedure. The voxel intensity is obtained by interpolating between the slices that bracket the voxel. A bilinear interpolation is performed in order to get the image coordinate intensity for each slice. The voxel intensity is then determined by performing a linear interpolation along Z between the two image coordinate intensities, using the distances between the slices and the voxel.

Points which are not between two slices are padded with zeros. Since the reformatting extents are the same for both reformatted volumes, voxel (i, j, k) of the reformatted MRA/CTA volume data corresponds to voxel (i, j, k) of the reformatted MR/CT volume data. The fusion between the volumes is therefore complete.

The frame space coordinates (x_i, y_j, z_k) corresponding to voxel (i, j, k) of the reformatted volume are determined by the use of the volume transformation matrix VTM.

$$\begin{bmatrix} x & y & z & 1 \end{bmatrix} = \begin{bmatrix} i & j & k & 1 \end{bmatrix} \cdot VTM \tag{5}$$

The VTM, a 4x4 matrix, accounts for translation, rotation and scaling between frame space and image space. Since the reformatted volume is aligned with the frame, the VTM is given by

$$VTM = \begin{bmatrix} \mathrm{v}_x & 0 & 0 & 0 \\ 0 & \mathrm{v}_y & 0 & 0 \\ 0 & 0 & \mathrm{v}_z & 0 \\ x_{\min} & y_{\min} & z_{\min} & 1 \end{bmatrix} \tag{6}$$

In the above expression, $(x_{\min}, y_{\min}, z_{\min})$ represents the minimum of the (X, Y, Z) reformatting extent in frame space. The reformatting voxel sizes (v_x, v_y, v_z) determine the scaling between the two spaces.

Since fusion is performed employing fiducial markers without taking into account anatomic information, the localisers must by firmly attached to the frame in order to ensure consistency.

2.3 SA projection geometry determination

This module allows the determination of the SA projection geometry for both the anterior-posterior (AP) and lateral (LAT) SA projections. These projection geometries are needed for the Correlation module.

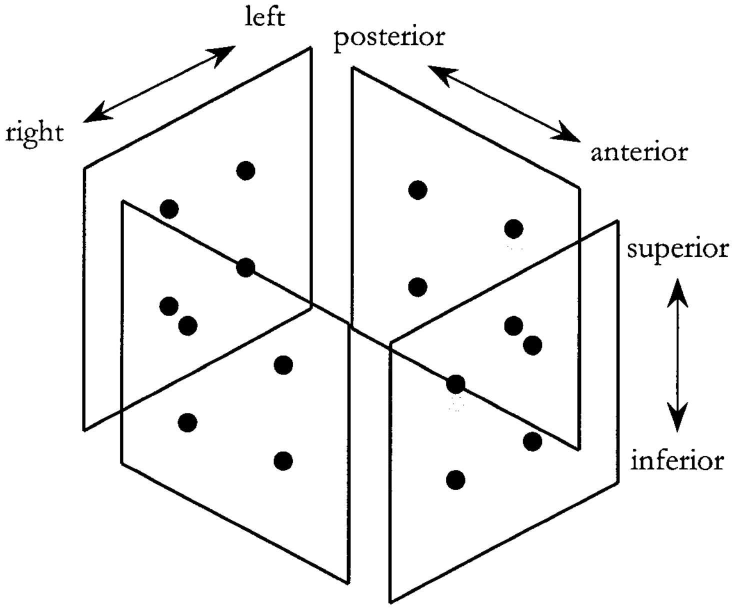

(a)

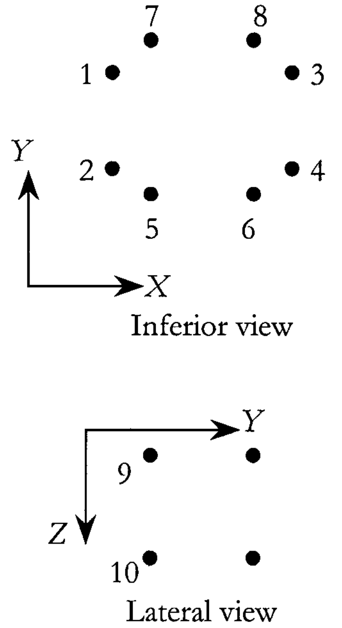

Point	x (mm)	y (mm)	z (mm)
1	4	135	---
2	4	65	---
3	196	135	---
4	196	65	---
5	67.5	-16	---
6	132.5	-16	---
7	67.5	216	---
8	132.5	216	---
9	---	---	65
10	---	---	135

(b)

Figure 20. Leksell SA localiser. The lead beads on the localiser box are illustrated in (a). A fifth bead, illustrated in shaded form, is found on the anterior plate as well as on the left plate for box face identification on the projection images. The frame space coordinates of the beads are given in (b).

The SA localiser contains a series of lead beads on each side of the frame attachment (Figure 20a). The frame space coordinates of the beads are given in Figure 20b. The lead beads, when projected onto the image plane, give eight image points (Figure 21). The eight user-selected markers have image space coordinates as (u_i, v_i). These image coordinates are employed to determine a transformation matrix which defines the perspective projection geometry by relating 3D frame coordinates to their projected positions in the image plane [58] (Figure 22). Accounting for perspective magnification, the 4x3 matrix transforms frame space coordinates into image coordinates according to the following equations.

$$[\alpha u \quad \alpha v \quad \alpha] = [x \quad y \quad z \quad 1] \begin{bmatrix} M_{11} & M_{12} & M_{13} \\ M_{21} & M_{22} & M_{23} \\ M_{31} & M_{32} & M_{33} \\ M_{41} & M_{42} & M_{43} \end{bmatrix} \tag{7}$$

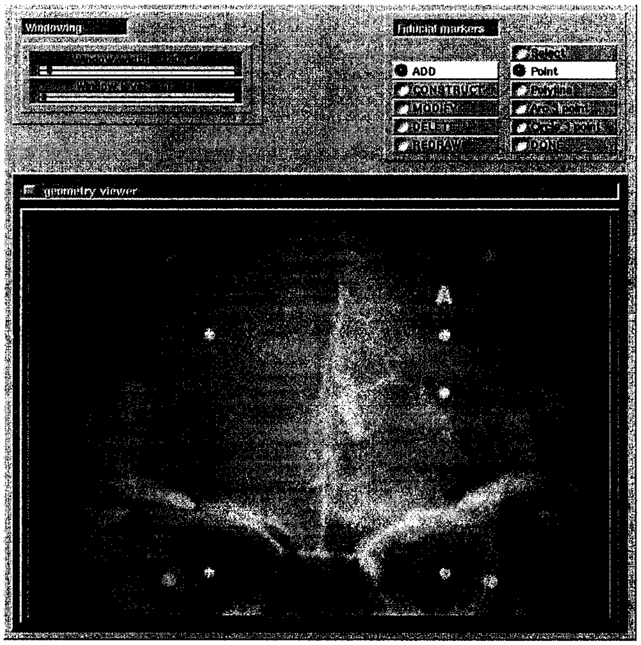

Figure 21. Panel for fiducial marker selection. The eight fiducial markers can be observed on the projection image.

In the above expression, the parameter α is a scaling factor between the two systems [58]. The image coordinates (u,v) are obtained by dividing through by α, the homogeneous coordinate [58]. Unlike tomographic images, projection images have image coordinates which cannot correspond to a single position in frame space since a single point in the image plane is the result of a many-to-one mapping of all points along the projected ray.

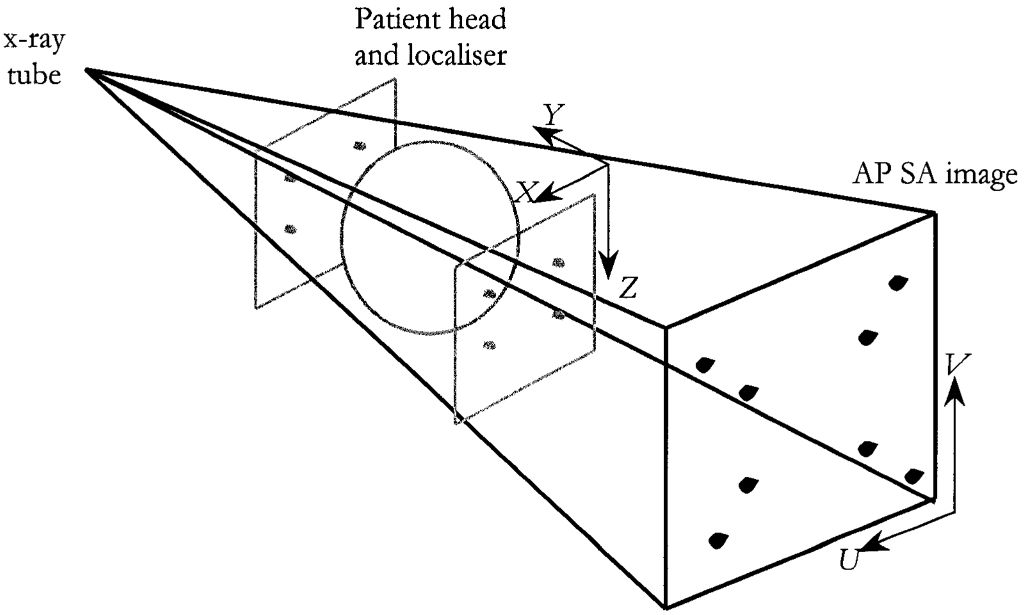

Figure 22. Perspective projection geometry. Of the eight points, the four obtained from the plate closest to the x-ray tube are more magnified than the four obtained from the plate on the opposite side.

The matrix multiplication above results in three separate equations. The α parameter is substituted into the first two, generating a system of two equations.

$$(M_{11} - uM_{13})x + (M_{21} - uM_{23})y + (M_{31} - uM_{33})z + M_{41} = uM_{43} \tag{8}$$

$$(M_{12} - vM_{13})x + (M_{22} - vM_{23})y + (M_{32} - vM_{33})z + M_{42} = vM_{43} \tag{9}$$

After division of Eqs. (8) and (9) by M_{43} (equivalent to setting M_{43} to unity), Eqs. (8) and (9) are rewritten for all eight fiducial markers in a single matrix form as:

$$\begin{bmatrix} u_1 \\ v_1 \\ \cdots \\ u_8 \\ v_8 \end{bmatrix} = \begin{bmatrix} x_1 & y_1 & z_1 & 1 & 0 & 0 & 0 & 0 & -u_1x_1 & -u_1y_1 & -u_1z_1 \\ 0 & 0 & 0 & 0 & x_1 & y_1 & z_1 & 1 & -v_1x_1 & -v_1y_1 & -v_1z_1 \\ & & & & \cdots & & & & & & \\ x_8 & y_8 & z_8 & 1 & 0 & 0 & 0 & 0 & -u_8x_8 & -u_8y_8 & -u_8z_8 \\ 0 & 0 & 0 & 0 & x_8 & y_8 & z_8 & 1 & -v_8x_8 & -v_8y_8 & -v_8z_8 \end{bmatrix} \cdot \begin{bmatrix} M_{11} \\ M_{21} \\ M_{31} \\ M_{41} \\ M_{12} \\ M_{22} \\ M_{32} \\ M_{42} \\ M_{13} \\ M_{23} \\ M_{33} \end{bmatrix} \qquad (10)$$

or in short form as:

$$A = BM \qquad (11)$$

In Eq. (10), the eight fiducial marker points and corresponding stereotactic coordinates are denoted as (u_i, v_i) and (x_i, y_i, z_i), respectively. Since there are sixteen equations and eleven unknowns, an over-determined system of equations is obtained and solved using a least-squares fit [73].

2.4 Correlation

This module correlates the 3D and 2D data by

1. ray-tracing through the reformatted MRA volume and comparing the resulting images with the SA images;

2. delineating the target on the two SA images and backprojecting the target contours into the MRA volume in order to reconstruct the target in 3D;

3. localising the AVM onto a 3D vasculature representation of the MRA volume with a 3D cursor and projecting the cursor position onto the SA images in order to compare the cursor projection with the target position on the SA images;

4. delineating the target in the MRA volume and projecting the target contours onto the SA images in order to compare the contour projections with the target extent on the SA images.

The ray-tracing element enables the examination of possible inconsistencies which could arise from MR distortions, SA distortions, frame slippage or other sources of image artefacts.

2.4.1 Ray-tracing

AP and LAT projection images of the reformatted MRA volume are obtained with the projection geometry used in the acquisition of the SA images determined by the SA projection geometry determination module (Figure 23).

The ray-tracing algorithm and interpolation scheme employed in this component were developed by Siddon [74] and Sherouse *et al.* [75], respectively, for simulating the acquisition of a radiographic image. Rather than considering individual voxels, the algorithm calculates the intersection points of rays with orthogonal sets of equally spaced, parallel planes [74] (Figure 24). The intersections are described as parametric values along the ray and are obtained as a subset of the intersections of the ray [74] (Figure 24). For each voxel intersection length, the corresponding voxel indices are obtained and the products of the intersected length and the particular voxel intensity are summed over all intersections to yield the radiological path [74] (Figure 24).

Since the resulting ray-traced MRA image must have the same characteristics as the SA images in order to correlate the images, pixel sizes, beam source position and orientation as well as image plane position and orientation must be determined and employed by the ray-tracing algorithm. Since these parameters are unknown, they are derived from the correspondence between a set of object features and a set of image features. The 4x3 projection transformation matrix of Eq. (7), relating object coordinates to projection image coordinates, describes the SA image acquisition geometry and therefore provides sufficient information to generate a matching view of the tomographic volume.

In order to perform the ray-tracing for every image coordinate (u,v), a ray vector is determined by specifying two points which correspond to the start and end of the ray path

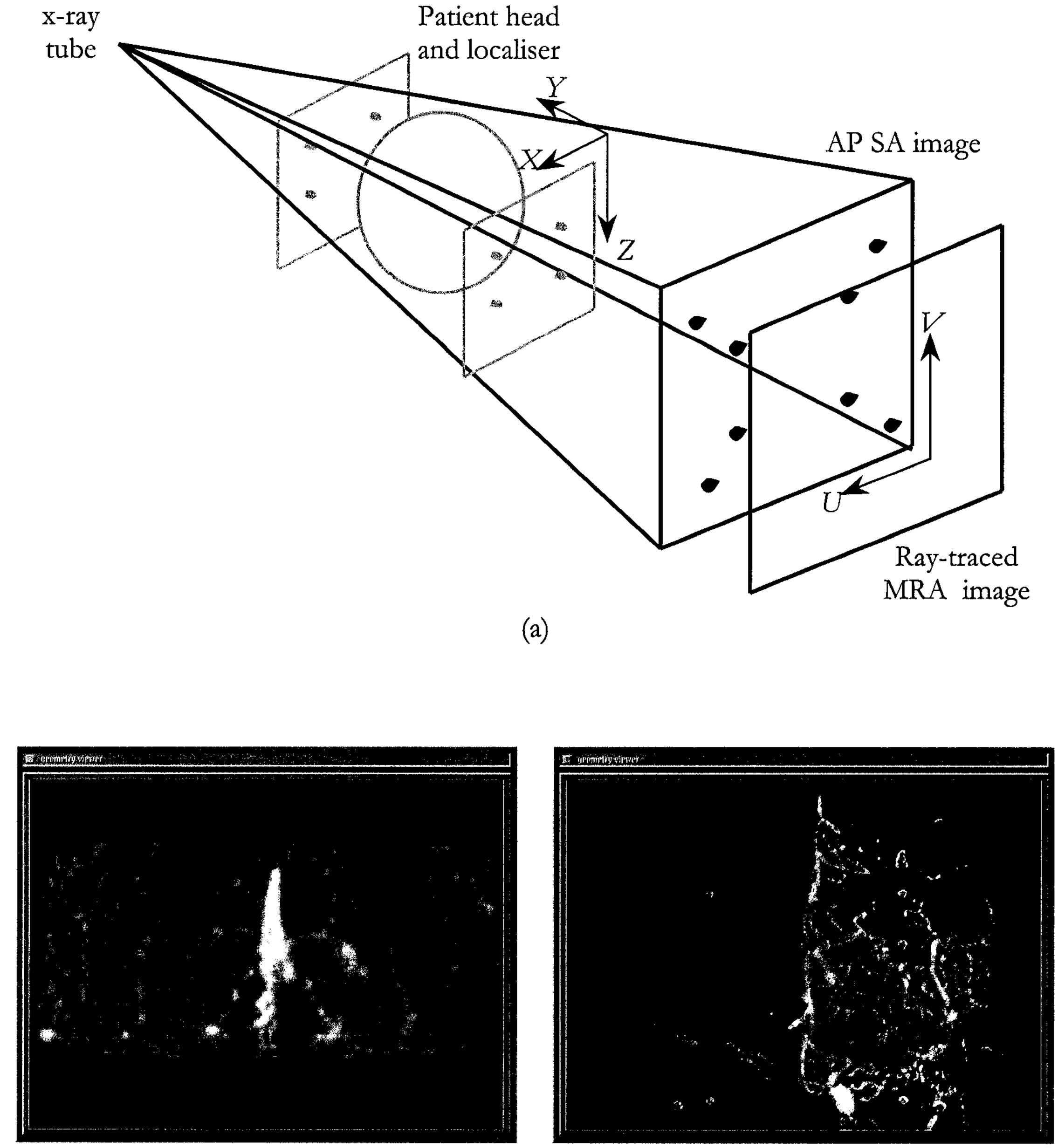

(a)

(b) (c)

Figure 23. Ray-tracing through the MRA volume. Employing the SA projection geometry illustrated in (a), the ray-traced MRA images (b) are correlated with the SA images (c). The correlation enables the examination of possible inconsistencies between the SA datasets and the reformatted MRA volume which could arise from MR distortions, frame slippage during the imaging procedure or other sources of image artefacts.

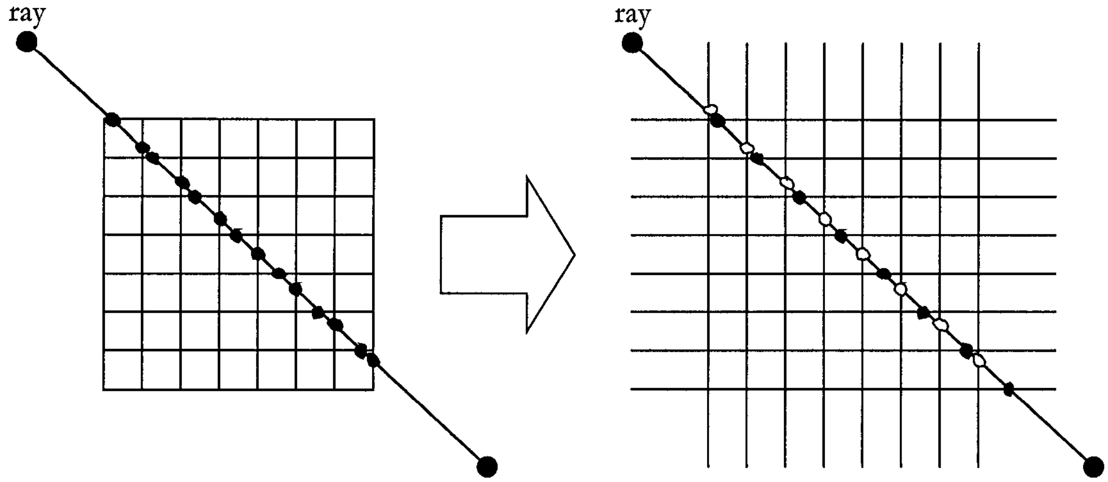

Figure 24. Ray-tracing algorithm [74]. The intersection of the ray with the voxels are a subset of the intersections of the ray with the lines [74]. The intersections of the ray with the lines are given by two equally spaced sets: one set for the horizontal lines (filled circles) and one set for the vertical lines (open circles) [74].

[74]. The two points are located outside the tomographic volume, and are chosen to be on the planes lying between the source and the tomographic volume and between the tomographic volume and image plane (Figure 25). For the Leksell frame, these planes are along XZ for the AP projection, as shown in Figure 22, and along YZ for the LAT projection. For pixel (u_i, v_i) of the AP projection, Eq. (8) and (9) are employed to determine the (x_{start}, z_{start}) and (x_{end}, z_{end}) coordinates at $Y_{start} = d - 1$ mm and $Y_{end} = e + 1$ mm respectively, where $Y = d$ mm and $Y = e$ mm are the plane equations of the first and last slice in frame space (Figure 25).

$$(M_{11} - u_i M_{13})x_{start,end} + (M_{31} - u_i M_{33})z_{start,end} = u_i - (M_{21} - u_i M_{23})Y_{start,end} - M_{41} \quad (12)$$

$$(M_{12} - v_i M_{13})x_{start,end} + (M_{32} - v_i M_{33})z_{start,end} = v_i - (M_{22} - v_i M_{23})Y_{start,end} - M_{42} \quad (13)$$

The above system of two equations is therefore employed to solve for the two unknowns x and z. Similarly for the LAT projection, the y and z coordinates are determined at $X_{start} = d - 1$ mm and $X_{end} = e + 1$ mm. The two points, p_{start} and p_{end}, are used as inputs

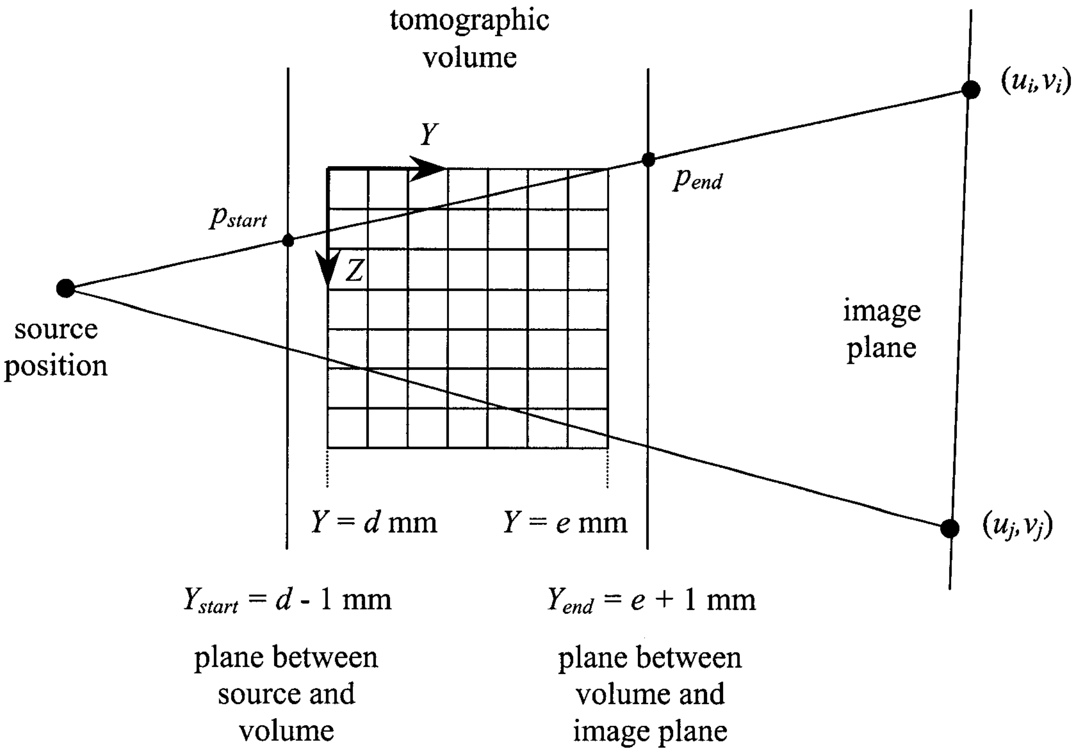

Figure 25. Ray-tracing projection geometry. For the AP projection, shown in the illustration, points p_{start} and p_{end} are located on the planes $Y_{start} = d - 1$ mm and $Y_{end} = e + 1$ mm, where $Y = d$ mm and $Y = e$ mm are the plane equations of the first and last slice along Y in frame space. Their coordinates are obtained with Eq. (12) and (13). Similarly for the LAT projection (not shown), the points p_{start} and p_{end} are located on the planes $X_{start} = d - 1$ mm and $X_{end} = e + 1$ mm in frame space and are determined by the same method.

to the ray-tracing algorithm [74] to proceed with a nearest neighbour, straight average, linear or trilinear interpolation [75]. The ray-traced images are overlaid onto the SA images with various user selected patterns (checkerboard) for inspection of consistency (Figure 26).

2.4.2 2D target delineation

If target delineation is performed on two 2D SA images (AP and LAT views), the contours are backprojected to a 3D dataset in order to determine the 3D shape of the target, necessary for 3D treatment planning. The backprojection is done using the projection geometry obtained in section 2.3.

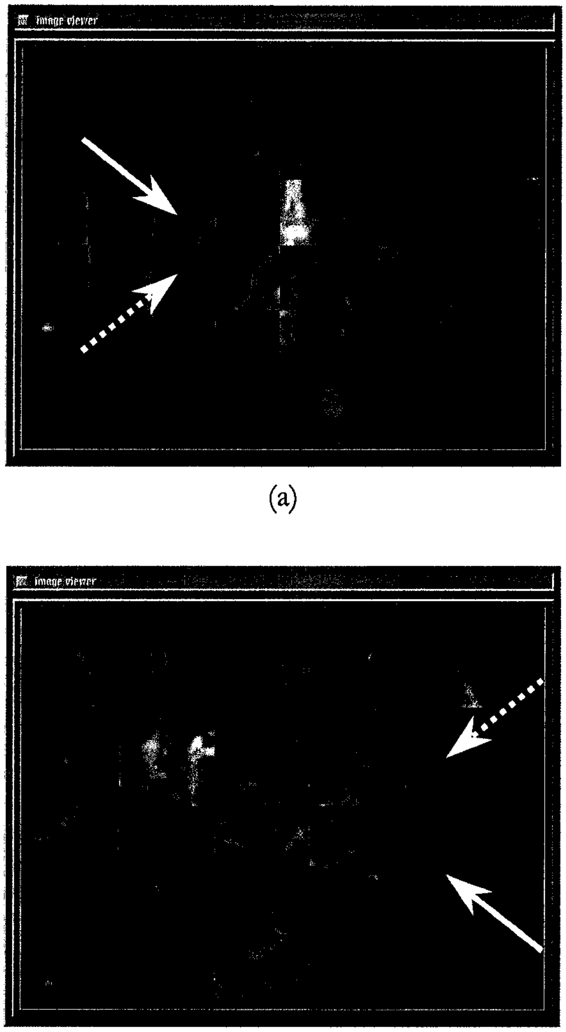

(a)

(b)

Figure 26. Ray-traced MRA images and SA images. The AP (a) and LAT (b) ray-traced images (solid arrows) are overlaid onto the AP (a) and LAT (b) SA images (dashed arrows) to check the consistency of the datasets.

For each projection , the target is delineated on the SA image and the contour is backprojected on each slice facing the corresponding SA image (Figure 27). A contour is backprojected in a manner similar to the one used for ray-tracing. For the Leksell AP projection shown in Figure 25, each point (u_i, v_i) of the SA target contour is backprojected onto each image slice of frame coordinates Y, between $Y = d$ mm and $Y = e$ mm, by determining the frame coordinates (x, z) with the use of Eqs. (12) and (13). When done for both projections, the

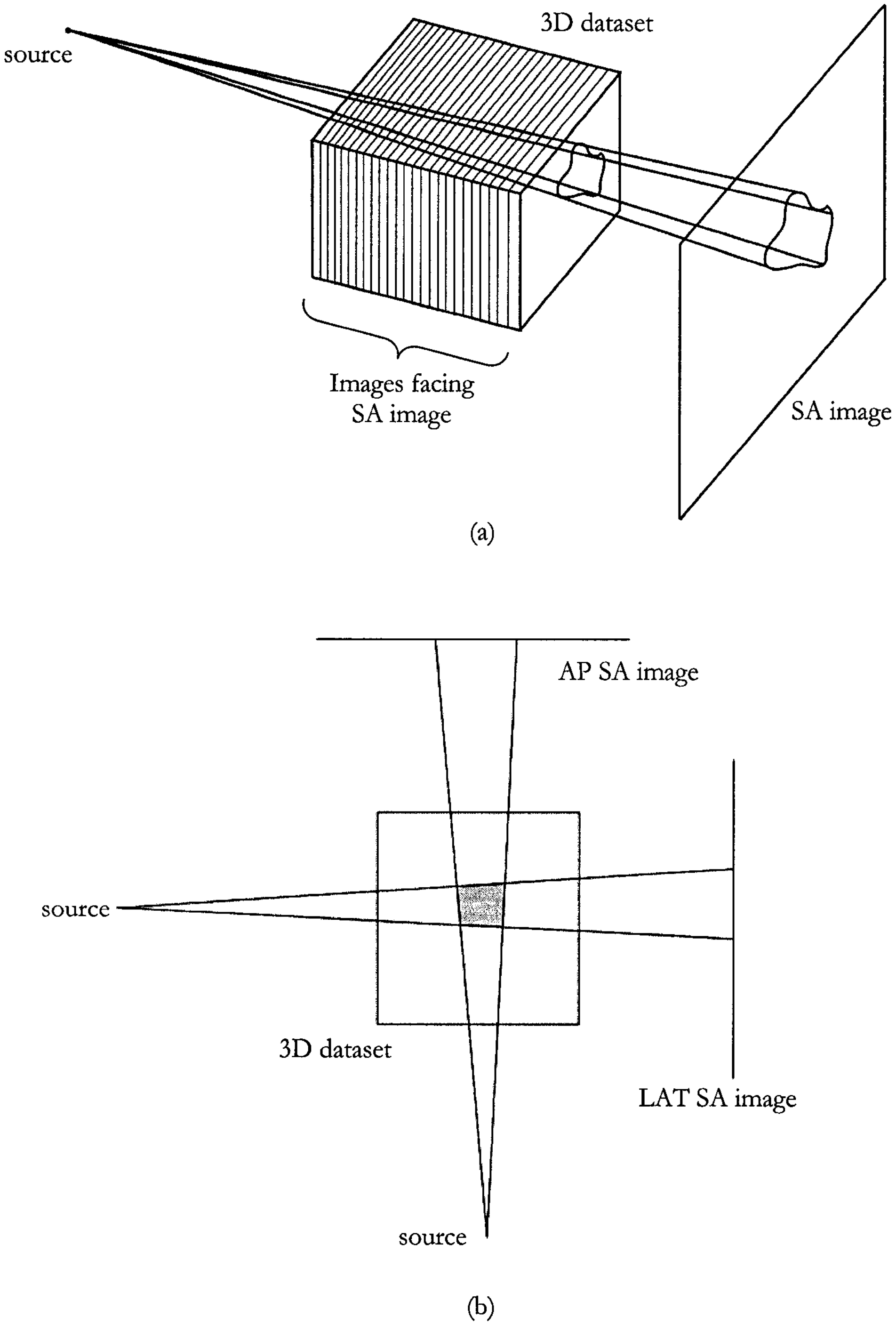

Figure 27. Backprojection of target contours drawn on SA images into 3D dataset. The target contour drawn on each SA image is backprojected on every image facing the corresponding SA image, as shown in the 3D view in (a). When done for both views (AP and LAT), the intersection of all contour backprojections define the 3D shape of the target, as shown in the top view in (b).

3D shape is reconstructed by intersecting the backprojected contours of the AP and LAT view.

2.4.3 3D target localisation

The AVM can be localised onto a volume rendered vasculature representation of the MRA volume with a 3D cursor (Figure 28). The cursor position in the MRA volume is projected onto the SA/ray-traced MRA images in order to compare the position of its projection with the target position on the SA images. The frame position (x, y, z) of the cursor is projected onto the image plane of the SA image employing the transformation matrix of Eq. (7).

2.4.4 3D target delineation

This step allows target delineation in 3D with the simultaneous use of the reformatted volumes as well as the SA and ray-traced MRA images. Target contours, which are drawn on the MRA volume, are concurrently visualised on the reformatted MR/CT volume and projected onto the SA images for correlation with the target extent on the SA images (Figure 29). Similarly, critical structure contours surrounding the AVM can be drawn on the MR/CT images, simultaneously visualised on the reformatted MRA volume, and simultaneously projected onto the SA images. Therefore, all vascular and anatomical information can be taken into account in the delineation process. This interactive process enables the user to modify contours accordingly as they are drawn on transverse, sagittal or coronal slices of the reformatted MRA volume.

Similar to the cursor projection, the frame position (x, y, z) of each contour point is projected onto the image plane of the SA image employing the transformation matrix of Eq. (7).

2.5 Validation

The system was implemented with the AVS 5.5 software (Advance Visual System Inc., Waltham, MA) running on a Pentium III processor (Intel Corporation, Santa Clara, CA) 800 MHz with 512 Megs of RAM. The underlying operational system is SuSE Linux 7.0 (SuSE Inc., California). The AVS software permits the programming of modules for specific tasks, which are then linked together in networks to complete application programs. This section

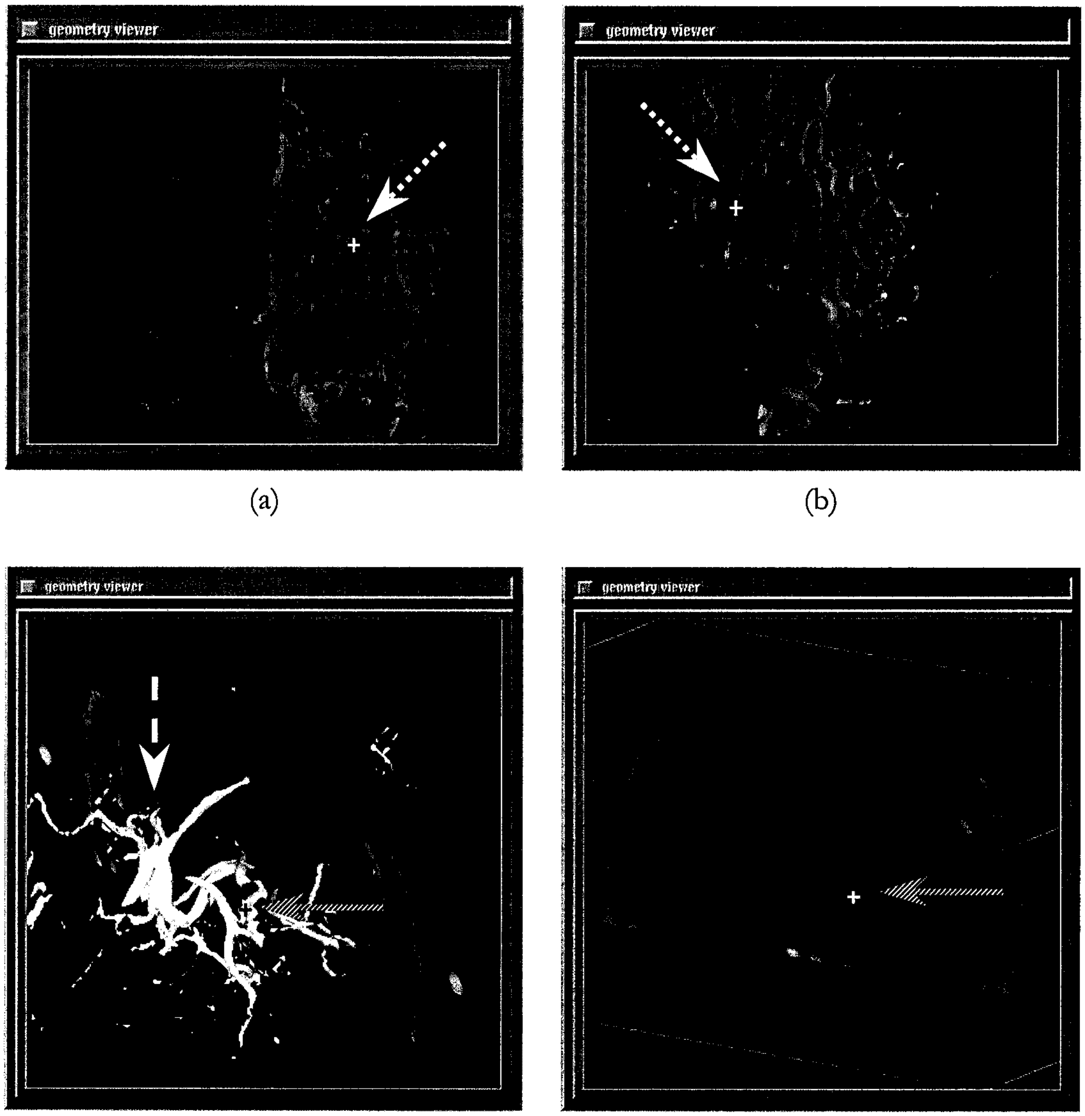

(a) (b)

(c) (d)

Figure 28. 3D target localisation with cursor and 3D vascular representation. The MR and SA images are shown in (d) and (a,b) respectively. The vasculature, shown in (c) by the long dashed arrow, is superposed onto the MRA images. A cursor (solid arrow) guides the physician within the fused volumes by projecting its position (dashed arrows) onto the SA images. The 3D vascular representation is removed for the delineation process.

validates the developed system tools described in the previous chapter. A phantom example is presented to validate the entire procedure.

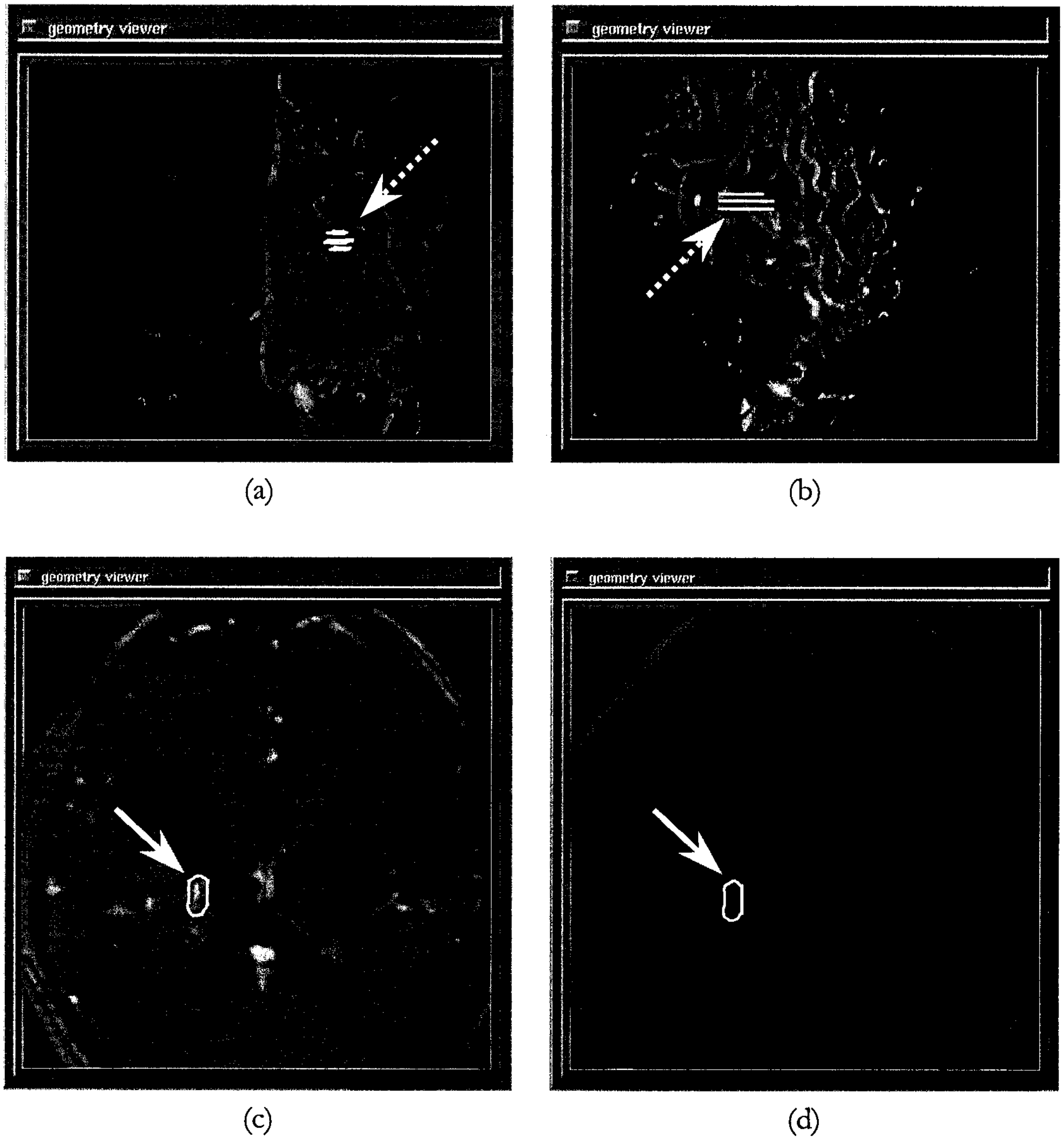

Figure 29. 3D target delineation. The contours, as well as their projections onto the SA images, are represented by the solid and dashed arrows respectively. The MRA, MR and SA images are shown in (c), (d) and (a,b) respectively. For the purpose of illustration, the contours were drawn on only three slices.

2.5.1 Quantitative validation

The volume localisation validation was performed only on the axial image orientation since FTMs are slice dependent and are defined for images in the image acquisition orientation.

The localisation uncertainty introduced by the user in the selection of the fiducial markers was evaluated by investigating the variability of the localisation results for 21 sets of 9 fiducial marker positions for one axial image. The marker positions were selected by seven users with 3 trials per user. Within the AVS environment, the marker selection probe provides subpixel accuracy in coordinate localisation. The precision of the localisation process was estimated by the standard deviation of the marker positions. The standard deviation was 0.3 pixels on an axial image of pixel size of 0.93 mm which corresponds to a value of 0.3 mm in frame space.

The accuracy of the volume localisation was evaluated by comparing results obtained with the developed environment to those obtained with a clinically used in-house treatment planning software [76, 77]. Since the fiducial markers are user-selected for both environments, the target locations are expected to differ by a small amount between the two environments. The process comparison was performed with ten prominent anatomical features by one user on axial images of a patient that was previously treated with radiosurgery at the MGH (Figure 30). The root mean square (RMS) error between the two environments was evaluated to be 0.7 mm in frame space for both the original images and reformatted images.

The accuracy of the SVD algorithm, employed for the determination of the SA projection geometry, was evaluated. For five predetermined projection geometries, the frame fiducial markers were projected and the known image coordinates of the projected fiducial markers were used by the SVD algorithm to recover the projection geometries (Eq. (10)). The RMS difference in marker positions as projected by the predetermined and the SVD-recovered projection geometries was calculated to be 0.02 pixels. This value, when backprojected onto the localiser box face closest to the image plane where the error is the greatest, corresponds to a frame space error of 0.02 mm.

The SA projection geometry determination uncertainty introduced by the user in the selection of the image fiducial markers was evaluated for 21 sets of 8 image fiducial marker positions, selected by seven users with 3 trials per user, for a given projection image. First, the projection geometry of each trial was determined. The average position of the respective image fiducial markers was then employed to determine the average projection geometry. The variability was evaluated by projecting the fiducial markers employing (1) the projection geometries and (2) the average projection geometry. The RMS difference in marker positions as projected by the

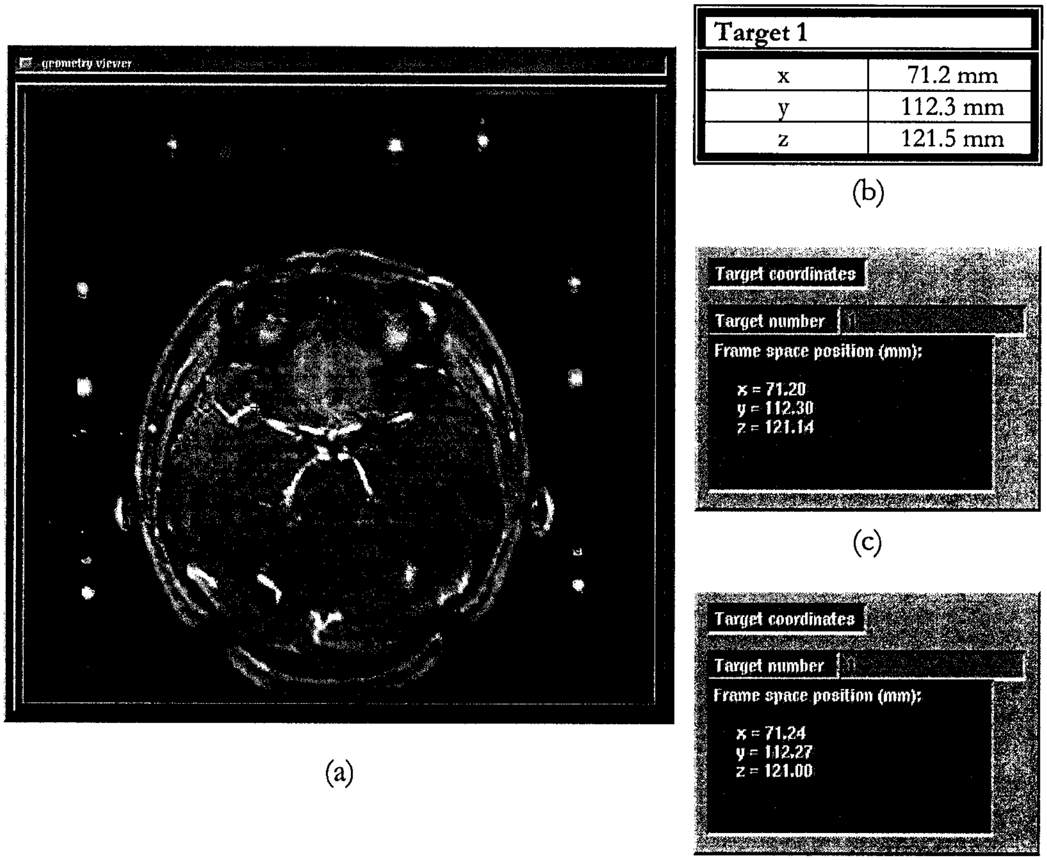

(a)

Target 1	
x	71.2 mm
y	112.3 mm
z	121.5 mm

(b)

Target coordinates

Target number 1

Frame space position (mm):

x = 71.20
y = 112.30
z = 121.14

(c)

Target coordinates

Target number 1

Frame space position (mm):

x = 71.24
y = 112.27
z = 121.00

(d)

Figure 30. The 3D localisation process comparison between the developed system and the clinically used in-house treatment planning software [76, 77]. A prominent anatomical feature, shown in (a), shows good agreement between the in-house treatment planning software (b) and the developed system with both initial (c) and reformatted (d) images.

determined projection geometry and the average projection geometry was calculated to be 0.2 pixels. This value was backprojected with the average projection geometry onto the localiser box face closest to the image plane where the error is the greatest. The value corresponds to a frame space error of 0.3 mm.

2.5.2 Illustrative validation: phantom example

The entire localising procedure was validated by simulating both 2D and 3D localisation with a specially designed phantom, illustrated in Figure 31a.

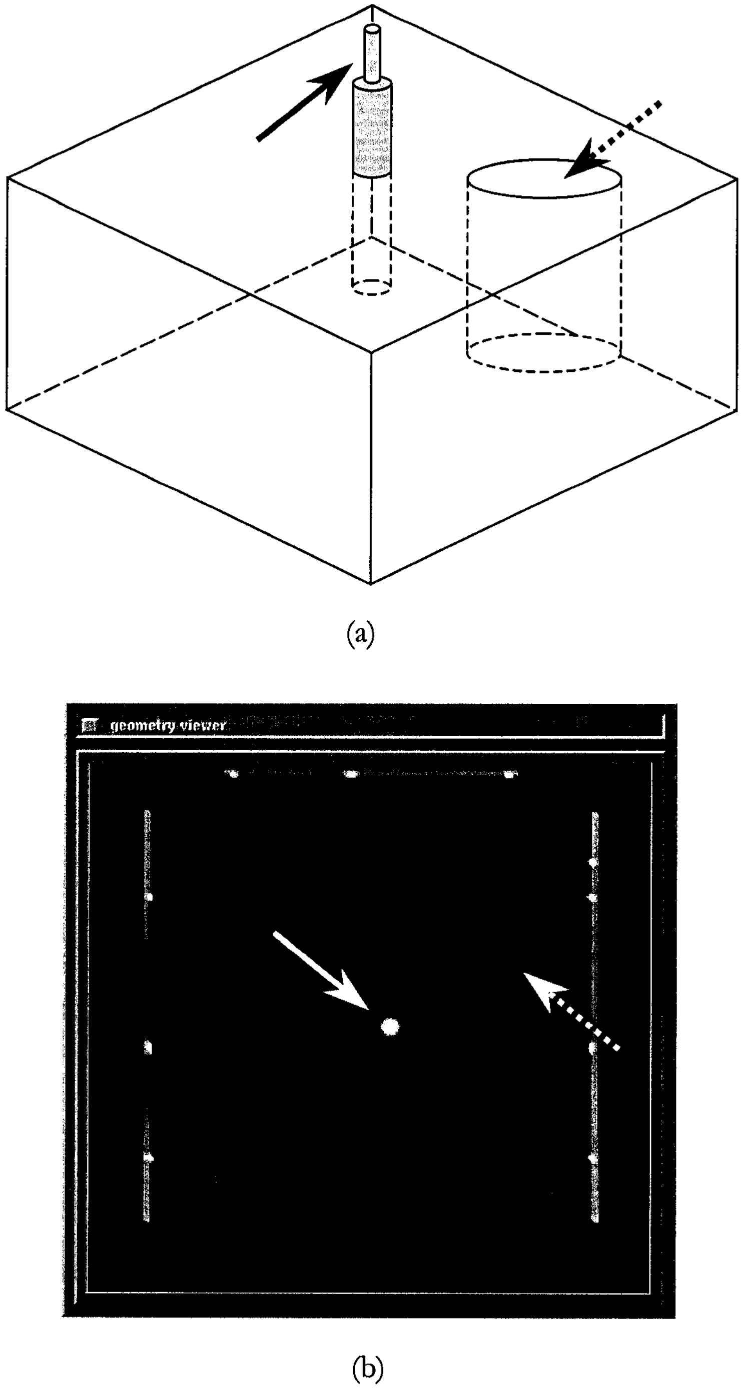

Figure 31. Validation phantom. The acrylic box, which was fixed to the stereotactic frame, contained an aluminium rod (solid arrow) as well as an air pocket (dashed arrow), as shown in (a), are visualised on CT images, as shown in (b).

A CT dataset (Figure 31b) was acquired with a PQ 5000 scanner (Picker Medical Systems, Cleveland, OH) and the conventional x-ray projection images were acquired with a Therasim 750 simulator (AECL, Kanata, Ontario), in order to compare 2D and 3D localisation of the aluminium rod tip in the acrylic box. The CT dataset had a pixel size of 1 mm by 1 mm with a slice thickness of 2 mm.

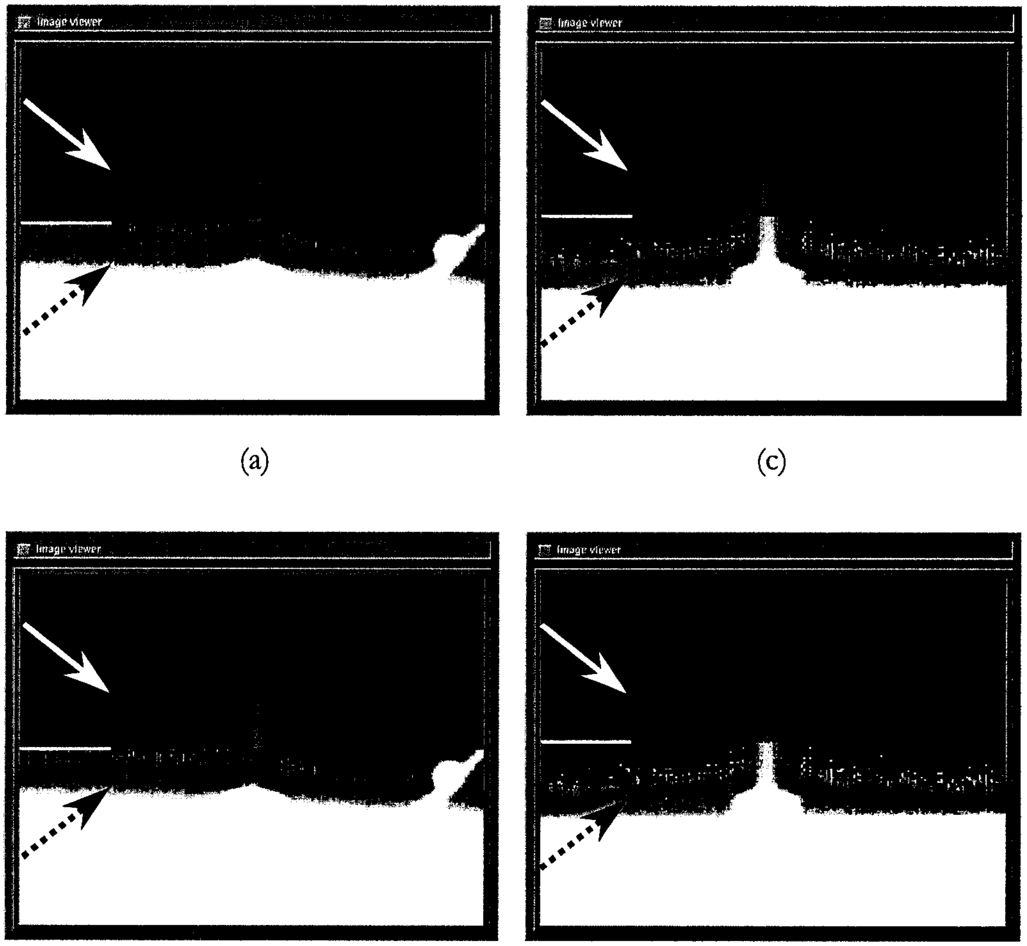

(a) (c)

(b) (d)

Figure 32. Ray-traced CT images and x-ray projection images. The ray-traced and x-ray projection images are shown by the solid and dashed arrows respectively. In the AP view shown in (a), the images correlated very well visually. However, the LAT view in (c) revealed an inconsistency between the images which was found to be due to an inaccuracy in the positioning of an N-shaped bar on the CT localiser box. The inaccuracy was fixed and the datasets were considered to be consistent, as shown in the AP (b) and LAT (d) views.

Ray-tracing was performed through the CT volume with the same projection geometry as the x-ray projections. As can be seen in Figure 32a, the AP ray-traced images correlate well visually with the AP x-ray projection images, however, the LAT view (Figure 32b) reveals an inconsistency between the ray-traced image and the x-ray projection image. A closer examination of the CT localiser box revealed an inaccuracy in the positioning of an N-shaped bar. The inconsistency in the localiser box was fixed and a second CT dataset was acquired. Ray-tracing was executed through the second CT volume, revealing that the datasets were consistent, as shown in Figure 32c and d. The rod tip was localised with the software at (109.2, 100.4, 65.9) mm within the initial volume and at (109.3, 100.5, 66.0) mm within the reformatted volume. The coordinates obtained with the software are in agreement with the coordinates obtained from manual localisation of the rod tip within the frame at (109.0, 100.5, 66.0) mm.

Given the ray-tracing results, the datasets were considered to be consistent and the aluminium rod as well as the air pocket were subsequently localised and delineated in 3D. The contours were drawn on the CT slices. Figure 33 and Figure 34 illustrate the delineation of the rod and the air pocket respectively. The results of Figure 33 are in agreement with the ray-tracing correlation. The contour projections of Figure 33 and Figure 34 illustrate good visual correlation between the CT and x-ray projection datasets. The phantom example has therefore validated the localisation and correlation procedures of the software.

2.6 Summary

In this chapter, the tools of the developed fusion and localisation system were presented and validated. The system consists of three modules: (1) Volume Registration and Reformatting, (2) SA projection geometry determination and (3) Correlation. The Volume Registration and Reformatting module fuses the 3D datasets. The SA projection geometry determination module determines the projection geometry of the SA images, employed in the Correlation module. The Correlation module correlates the 3D and 2D data by ray-tracing through the MRA volume and comparing the resulting images with the SA images, and by allowing 3D target localisation and delineation within the fused volumes and simultaneously projecting the target contours onto the SA images for visual feedback.

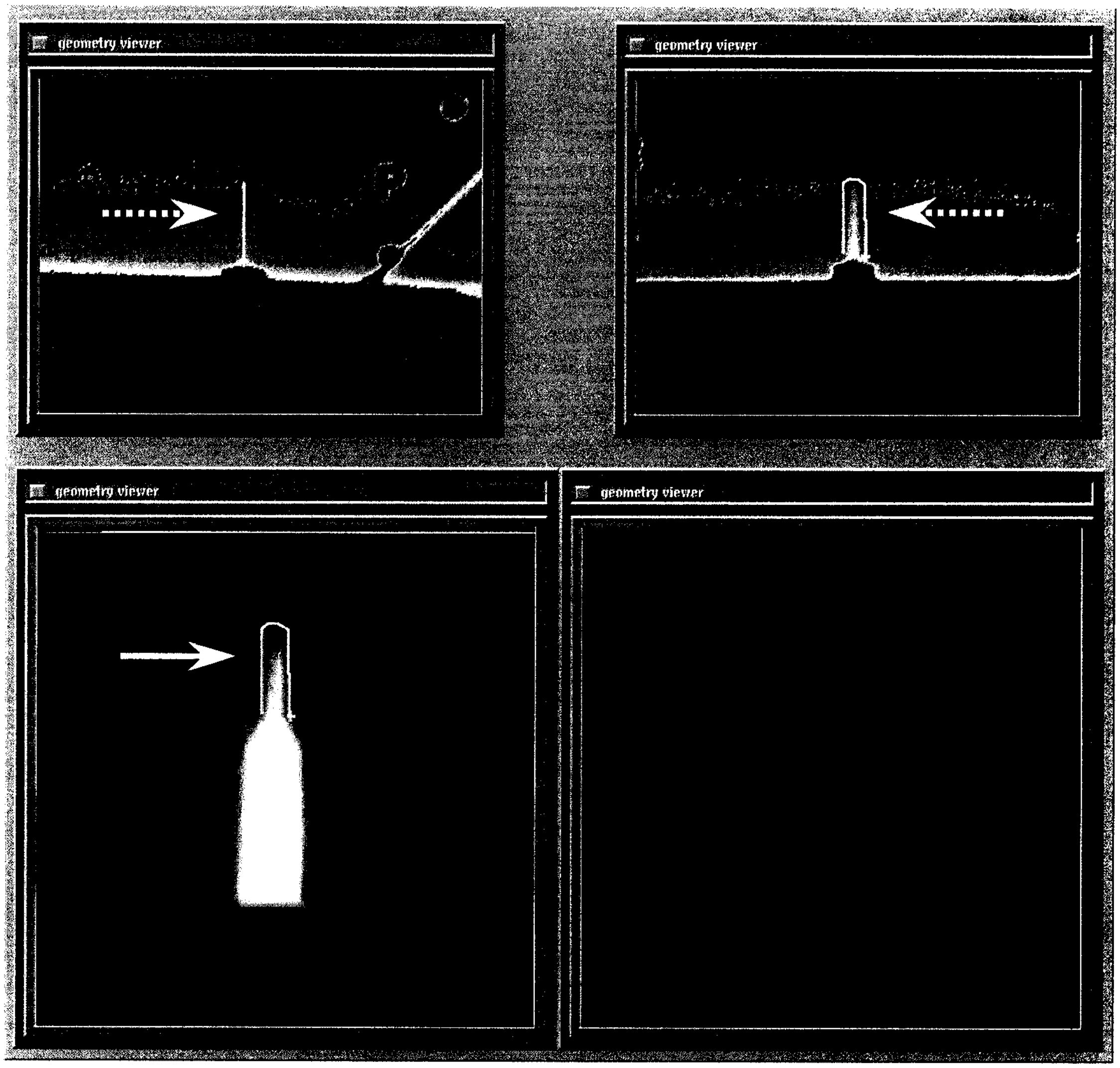

Figure 33. 3D target localisation and delineation panel. The contours (solid arrow) of the rod were drawn within the CT data (bottom left window) with continuous feedback from the visual correlation of the contour projections (dashed arrows) with the target extent on the x-ray projection images (top left and right windows). The bottom right window was not used for this example.

The 3D localisation uncertainty introduced by the user in the selection of the fiducial markers was evaluated to be 0.3 mm in frame space. The overall accuracy of the 3D localisation software was estimated to be 0.7 mm for the initial and reformatted images. The accuracy of the SVD algorithm was evaluated to be 0.02 mm in frame space. The uncertainty introduced

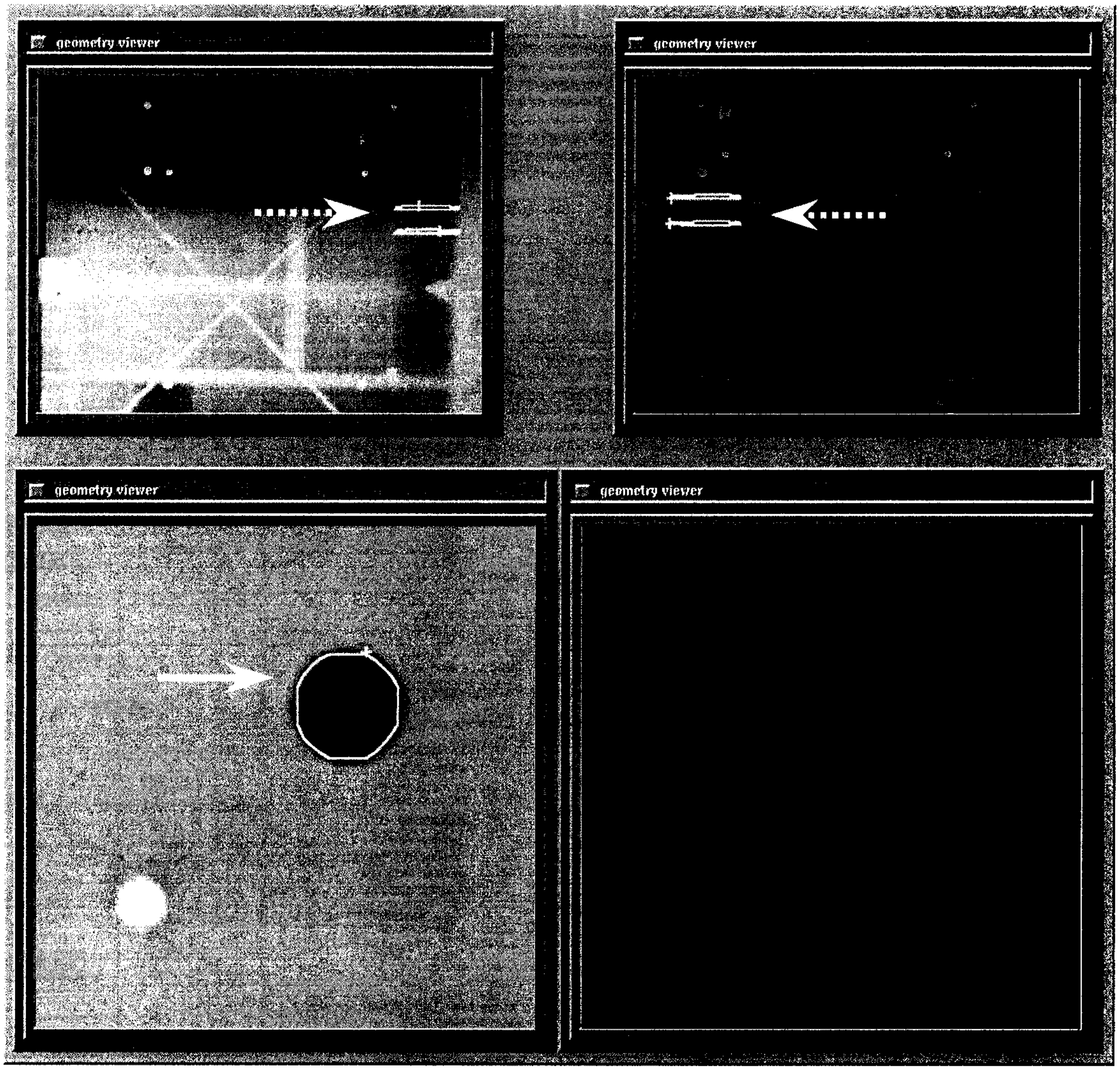

Figure 34. 3D target localisation and delineation panel. The contours (solid arrow) of the air pocket were drawn within the CT data (bottom left window) with visual correlation of the contour projections (dashed arrows) with the target extent on the x-ray projection images (top left and right windows). The bottom right window was not used for this example.

by the user in the selection of the image fiducial markers was evaluated to be 0.3 mm in frame space.

Chapter 3

Correlation of Ray-traced MRA and SA Images

3.1 Introduction

As described in Chapter 2, in order to detect inconsistencies between the 3D and 2D datasets, ray-tracing is performed through the MRA volume and the resulting images are compared to the SA images. Inconsistencies can arise from MR distortions, frame slippage or other image artefacts. Summed and maximum intensity traced images, taken along AP and LAT views, are presented for three patients. These patients had previously undergone radiosurgery and had been planned with the McGill technique employing SA and MR images without computer-assisted correlation methods discussed in Chapter 2. An MRA dataset was also acquired at the time of MR scanning employing the 3D TOF technique. In order to examine the capabilities to detect possible inconsistencies which could arise between the datasets, simulated shifts of the MRA volume in stereotactic space were performed and the ray-traced images and SA images were compared for the three patients.

3.2 Patient 1

This patient, a female of 25 years of age, had no previous surgery. The MR and MRA images had voxel sizes of $0.94 \times 0.94 \times 2\ mm^3$ and $0.94 \times 0.94 \times 1.3\ mm^3$, respectively. The ray-traced images and SA images are given in Figure 35. Thresholding of the MRA volume was done prior to ray-tracing in order to increase the quality of the ray-traced images. A comparison of the ray-traced MRA images and SA images of the patient is shown in Figure 36a and Figure 37a. The AP and LAT ray-traced images correlate very well visually with the AP and LAT SA images in the vicinity of the AVM. However, the ray-traced MRA images suggest a greater AVM volume. The vessels in the surrounding region of the AVM, which correlate very well visually as seen in Figure 36a and Figure 37a, can also be compared in order to provide additional information to the correlation process of the datasets.

In order to simulate inconsistencies which could arise between the datasets, the MRA volume was shifted within stereotactic space. The MRA volume was shifted 2 mm towards the left of the frame for the AP view and 2 mm towards the top of the frame for the LAT view, and ray-tracing was performed. As can be seen in Figure 36b and Figure 37b, the ray-traced MRA image do not correlate as well visually with the SA image in the vicinity of the AVM, as well as in the surrounding region.

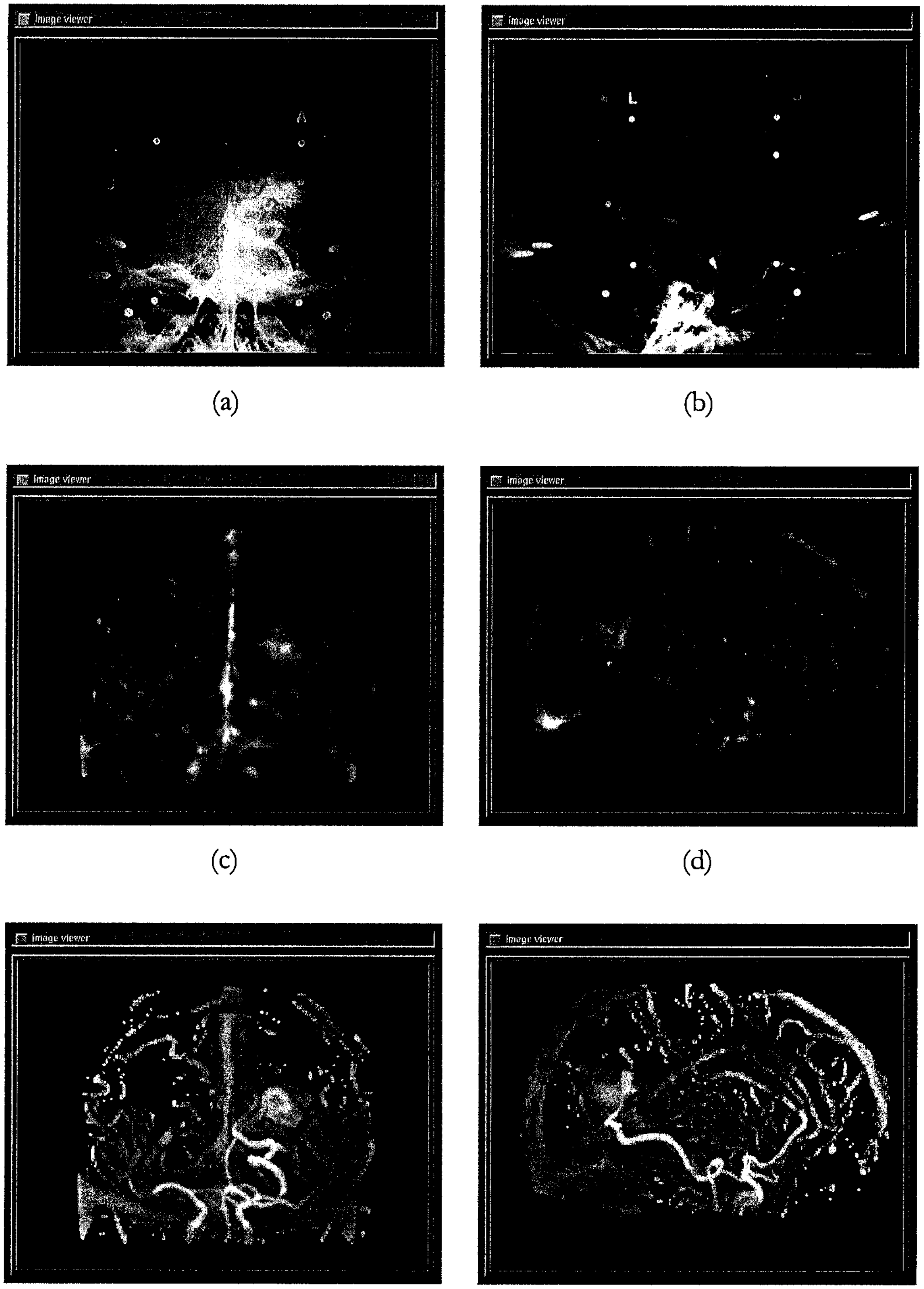

(a) (b)

(c) (d)

(e) (f)

Figure 35. SA and ray-traced MRA images for patient 1. The traced images obtained by the summing (c,d) and the maximum intensity (e,f) techniques are acquired with the projection geometry of the SA AP (a) and LAT (b) views.

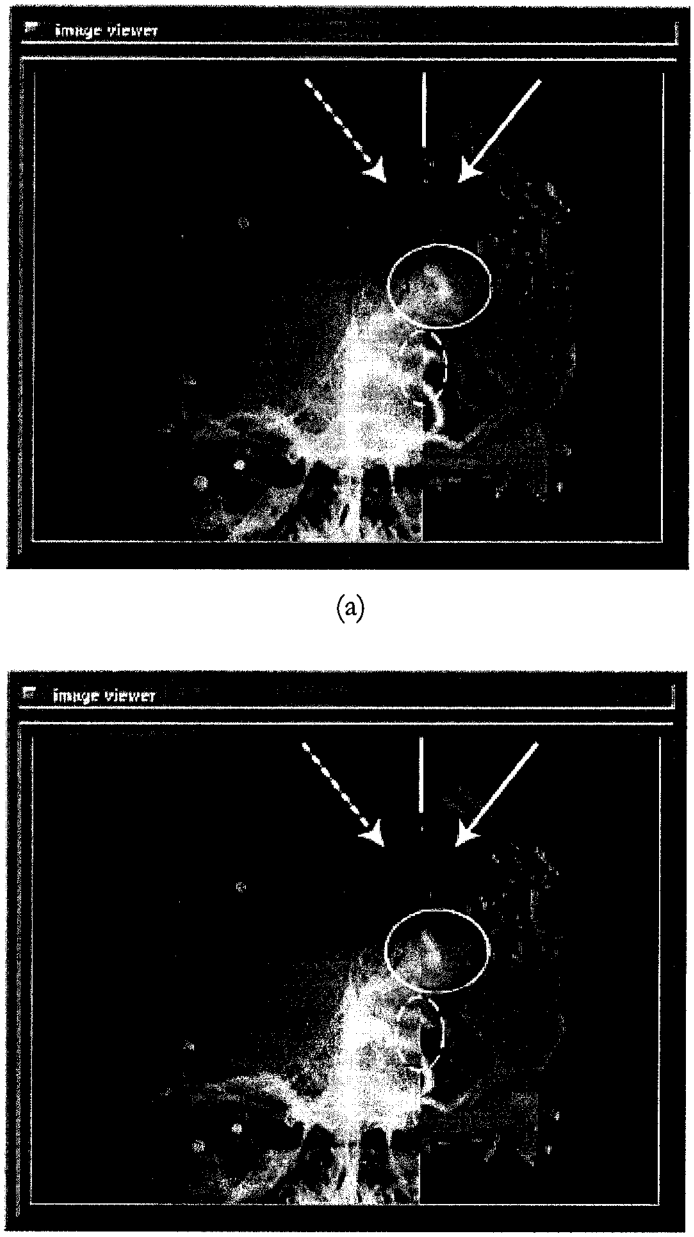

(a)

(b)

Figure 36. Comparison of ray-traced MRA images (solid arrows) and SA images (dashed arrows) for the AP view for patient 1. The datasets are considered to be consistent in the vicinity of the AVM (solid circle) and surrounding region (dashed circle) as shown in (a). However, the traced MRA images suggest a greater AVM volume. In (b), a simulated shift of the MRA volume of 2 mm towards the left of the frame was performed in order to evaluate the capabilities to detect inconsistencies between datasets. In this case, the images do not correlate as well visually (dashed circle).

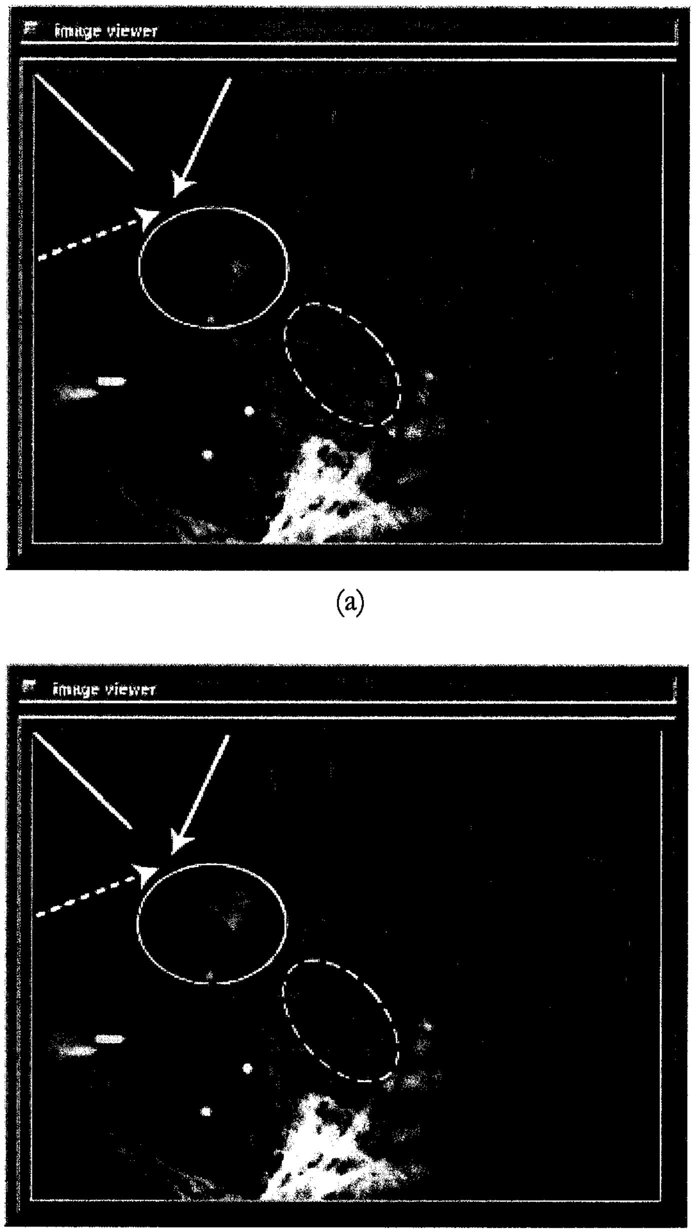

(a)

(b)

Figure 37. Comparison of ray-traced MRA images (solid arrows) and SA images (dashed arrows) for the LAT view for patient 1. The datasets are considered to be consistent in the vicinity of the AVM (solid circle) and surrounding region (dashed circle) as shown in (a). In (b), a simulated shift of the MRA volume of 2 mm towards the top of the frame was performed. In this case, the images do not correlate as well visually (dashed circle).

3.3 Patient 2

This patient, a female of 22 years of age, had no prior surgery. The MR and MRA images had voxel sizes of 0.94 x 0.94 x 2 mm^3 and 0.94 x 0.94 x 1.3 mm^3, respectively. The ray-traced images and SA images are given in Figure 38. Once again, thresholding of the MRA volume, was done prior to ray-tracing in order to increase the quality of the ray-traced images. A comparison of the ray-traced MRA images and SA images of the patient is shown in Figure 39a and Figure 40a. The AP and LAT ray-traced images correlate very well visually with the AP and LAT SA images in the vicinity of the AVM. The vessels in the surrounding region of the AVM do not correlate as well visually which can be due to an MR artefact, a distortion in the SA image (less probable), or another image artefact. Since the modalities offer different vasculature information, differences between the SA and ray-traced MRA images are visible.

In order to examine the capabilities to detect possible inconsistencies which could arise between the datasets, a simulated shift of the MRA volume in stereotactic space was performed. The MRA volume was shifted 2 mm towards the right of the frame for the AP view and 2 mm towards the bottom of the frame for the LAT view, and ray-tracing was then executed. As can be seen in Figure 39b and Figure 40b, the ray-traced MRA images do not correlate as well visually with the SA images in the vicinity of the AVM. Therefore, inconsistencies between MRA volumes and SA images, such as shifts of the MRA volume in frame space, can be detected.

3.4 Patient 3

This patient, a female of 40 years of age, had undergone neurosurgery prior to radiosurgery. During neurosurgery, adjacent feeding arteries on the brain surface were interrupted with permanent clips to gradually coagulate the entire vascular mass [78]. However, these metal clips produce artefacts on MR and MRA images (Figure 41) which were acquired with voxel sizes of 0.94 x 0.94 x 2 mm^3 and 0.94 x 0.94 x 1.3 mm^3, respectively. Nonetheless, ray-tracing was performed in order to compare the resulting images to the SA images (Figure 42). Once again, thresholding of the MRA volume was done prior to ray-tracing in order to increase the quality of the ray-traced images. A comparison of the ray-traced MRA images and SA images of the patient is shown in Figure 43a and Figure 44a. Due to the image artefacts, the AVM is not clearly visible on the ray-traced images. However, on the AP view, a vessel which is visible

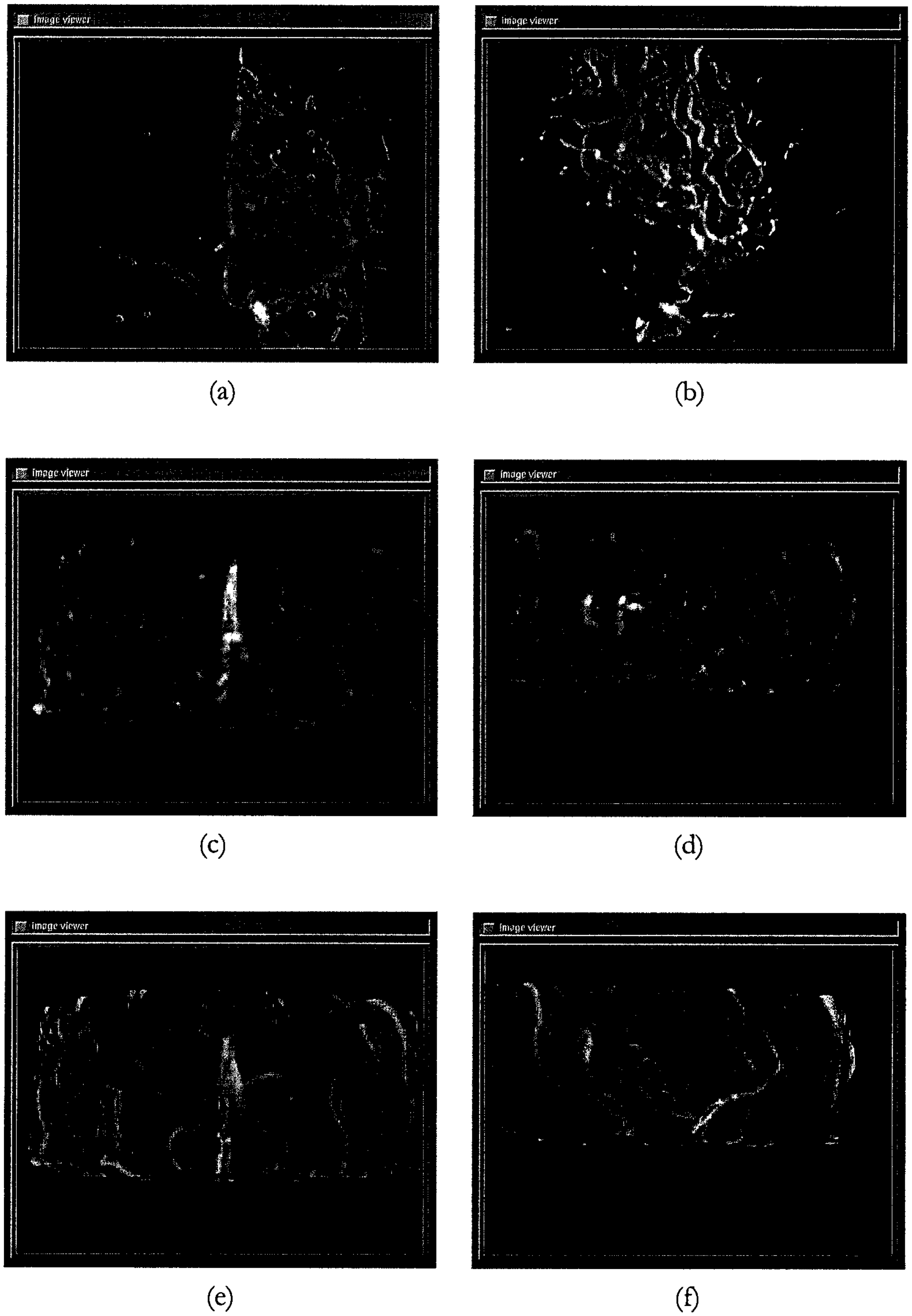

(a) (b)

(c) (d)

(e) (f)

Figure 38. SA and ray-traced MRA images for patient 2. The traced images obtained by the summing (c,d) and the maximum intensity (e,f) techniques are acquired with the projection geometry of the SA AP (a) and LAT (b) views.

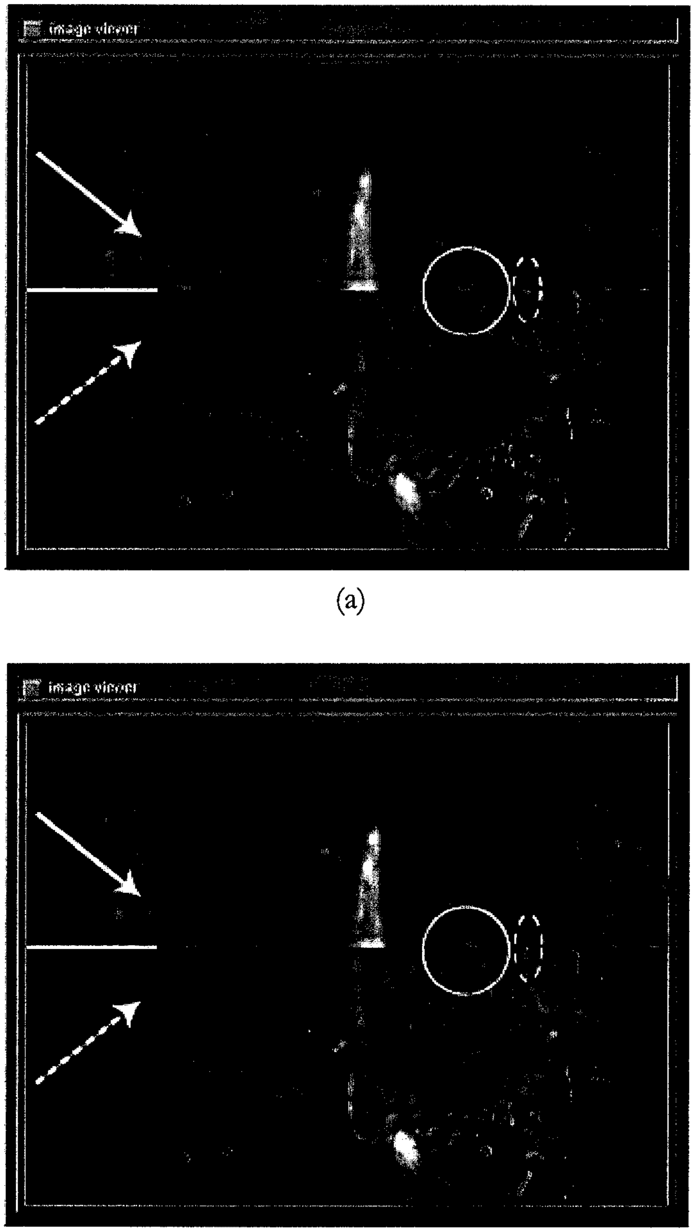

(a)

(b)

Figure 39. Comparison of ray-traced MRA images (solid arrows) and SA images (dashed arrows) for the AP view for patient 2. The datasets are considered to be consistent in the vicinity of the AVM, as shown inside the circular region in (a). However, the vessels in the surrounding region of the AVM do not correlate as well visually, which can be due to a MR artefact, or another image artefact. In (b), a simulated shift of the MRA volume of 2 mm towards the right of the frame was performed in order to evaluate the capabilities to detect inconsistencies between datasets. As can be seen, the images do not correlate as well visually in the vicinity of the AVM.

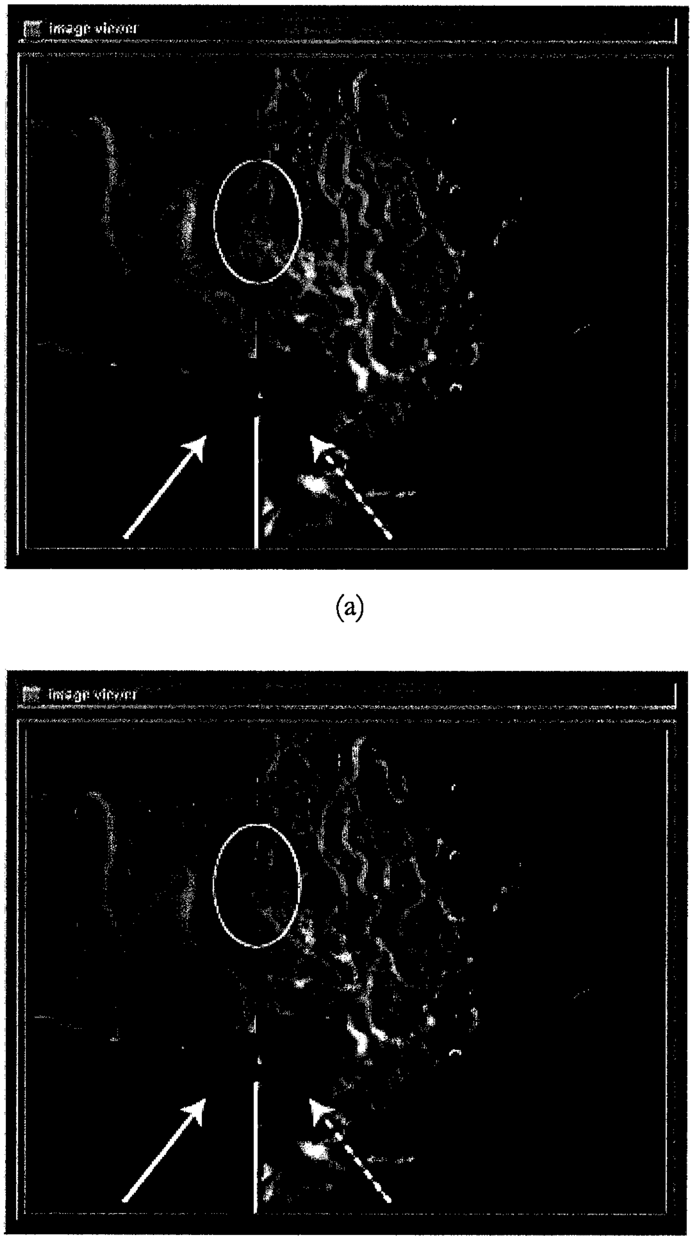

(a)

(b)

Figure 40. Comparison of ray-traced MRA images (solid arrows) and SA images (dashed arrows) for the LAT view for patient 2. The datasets are considered to be consistent in the vicinity of the AVM, as shown inside the circular region in (a). In (b), a simulated shift of the MRA volume of 2 mm towards the bottom of the frame was performed. In this case, the images do not correlate as well visually in the vicinity of the AVM.

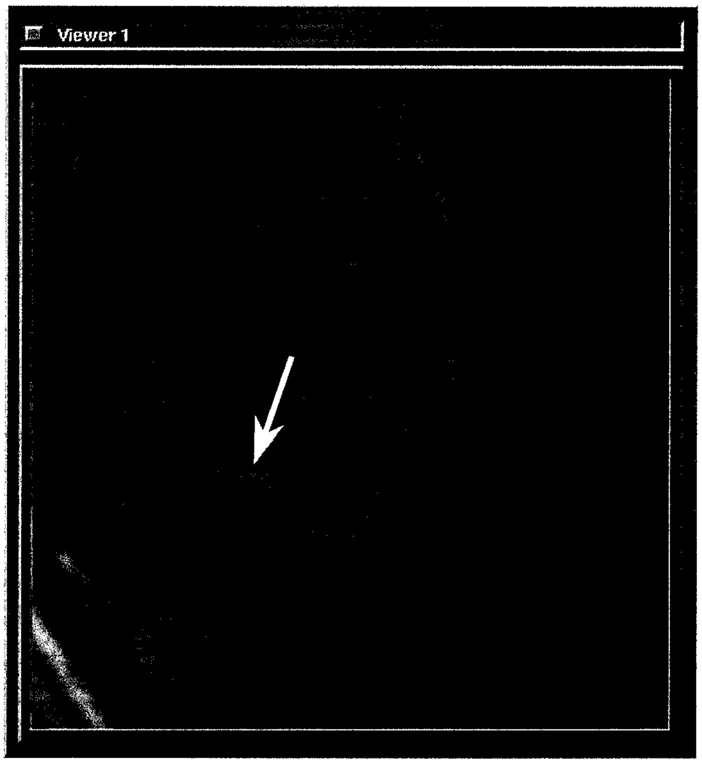

Figure 41. MRA images illustrating the MR artefact. The MR artefact is the dark region in the image, shown by the arrow.

on the ray-traced images in the lower region of the AVM correlates well with the vessel on the SA image. For the LAT view, the vessels in the surrounding region of the AVM correlate well.

In order to simulate inconsistencies which could arise between the datasets, the MRA volume was shifted within stereotactic space. The MRA volume was shifted 2 mm towards the bottom of the frame for both views, and ray-tracing was performed. For the AP view, Figure 43b illustrates that the lower region of the AVM does not correlate as well visually with the SA image, however, the shift is not easily detected since voxel information in the region of the AVM is minimal due to the MR artefacts. Figure 44b shows that the vessel in the LAT view in the surrounding region of the AVM does not correlate as well visually with the SA image. The MRA volume shift in frame space was detected mostly due to the vessels in the surrounding region of the AVM in the LAT view.

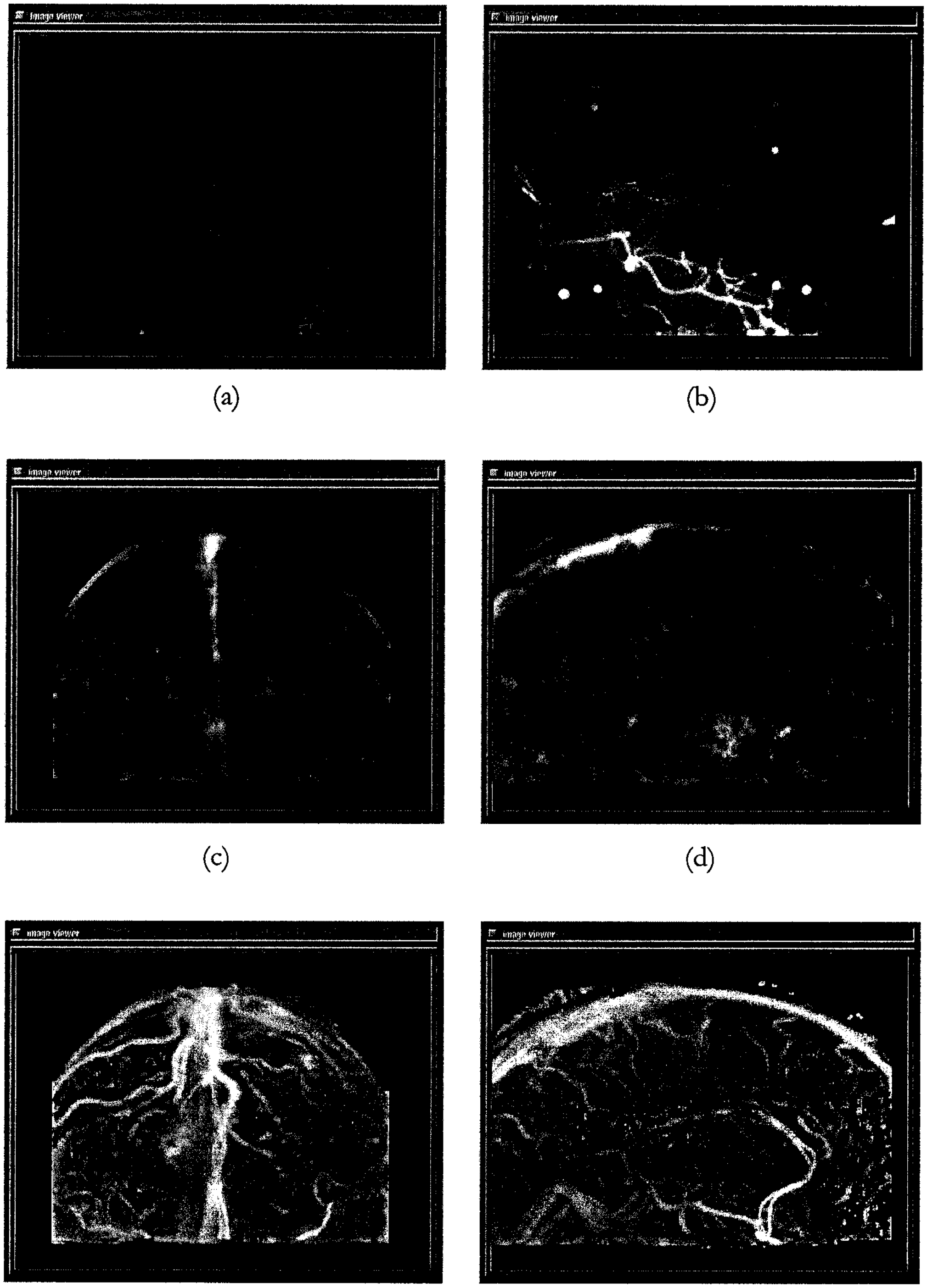

(a) (b)

(c) (d)

(e) (f)

Figure 42. SA and ray-traced MRA images for patient 3. The traced images obtained by the summing (c,d) and the maximum intensity (e,f) techniques are acquired with the projection geometry of the SA AP (a) and LAT (b) views.

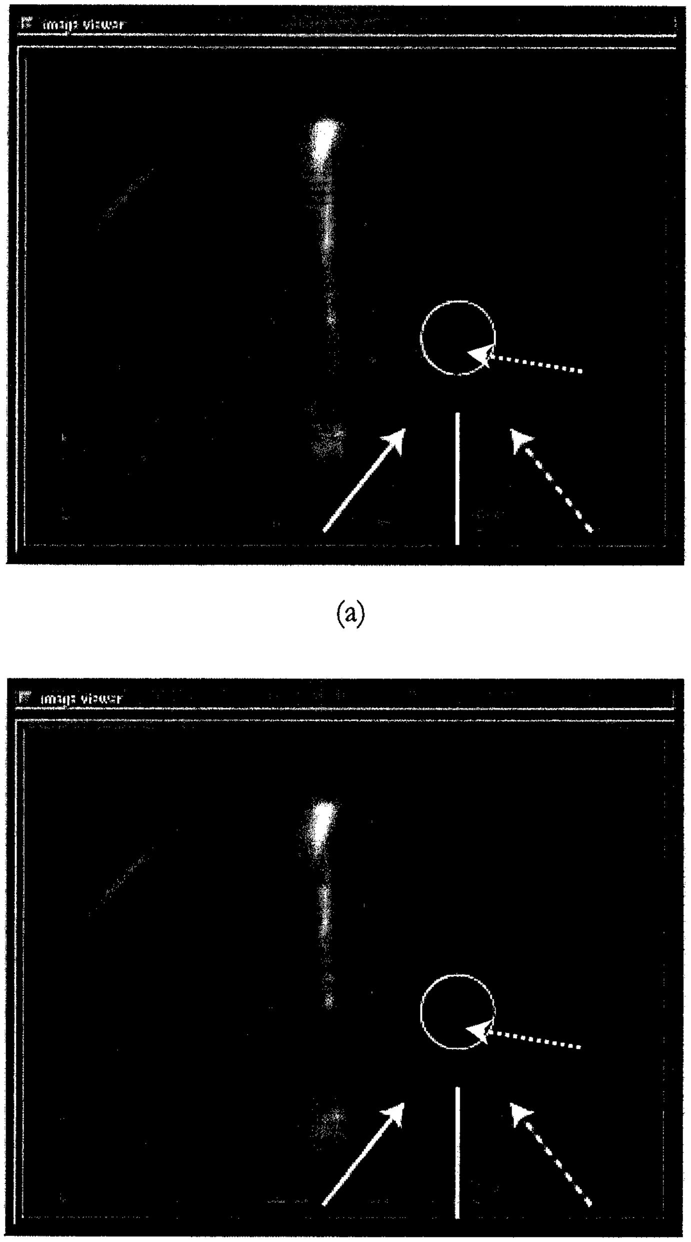

(a)

(b)

Figure 43. Comparison of ray-traced MRA images (solid arrows) and SA images (dashed arrows) for the AP view for patient 3. As shown in (a), the vessels in the vicinity of the AVM (solid circle) are not clearly visible on the ray-traced images due to the MR artefacts in the MRA images (Figure 41). However, a vessel, visible on the ray-traced images in the lower region of the AVM (dotted arrow), correlates well with the vessel on the SA image, however, the lack of voxel information in the region of the AVM due to the MR artefacts limits the visual clarity. In (b), a simulated shift of the MRA volume of 2 mm towards the bottom of the frame was performed in order to evaluate the capabilities to detect inconsistencies between datasets. The vessel in the lower region of the AVM does not correlate as well visually, however, the shift is not easily detected.

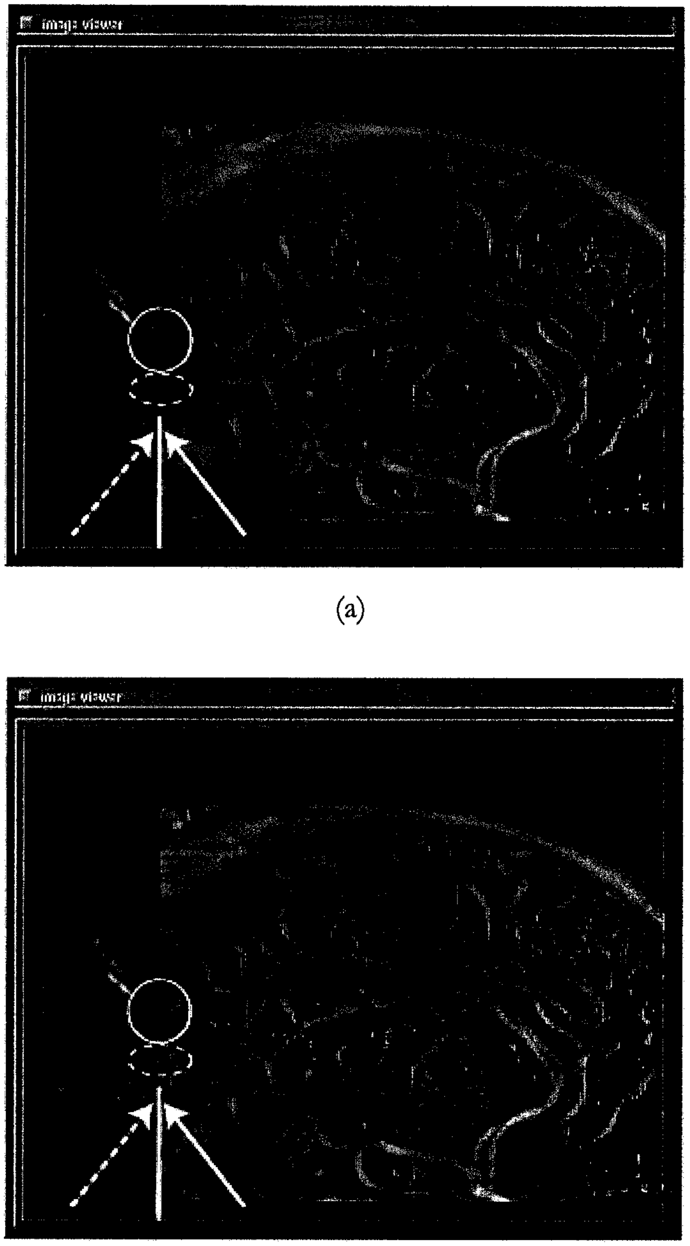

(a)

(b)

Figure 44. Comparison of ray-traced MRA images (solid arrows) and SA images (dashed arrows) for the LAT view for patient 3. As shown in (a), the vessels in the vicinity of the AVM (solid circle) are not clearly visible on the ray-traced images due to the MR artefacts in the MRA images (Figure 41). However, the datasets are considered to be consistent in the surrounding region of the AVM (dashed circle). In (b), a simulated shift of the MRA volume of 2 mm towards the bottom of the frame was performed in order to evaluate the capabilities to detect inconsistencies between datasets. In this case, the images do not correlate as well visually in the surrounding region of the AVM.

3.5 Summary

In this chapter, ray-traced MRA images and SA images were correlated to detect inconsistencies between the datasets. In order to evaluate the capabilities to detect possible inconsistencies which could arise between the datasets, simulated shifts in stereotactic space were applied to the MRA volume.

For two of the three patients, the ray-traced MRA images correlated well with the SA images, however, for one patient, the ray-traced MRA images suggested an AVM volume greater than that suggested by the SA images. For the third patient, voxel information in the region of the AVM was minimal due to artefacts in the MRA images. The correlation of ray-traced MRA and SA images can therefore reveal important information about the datasets prior to target localisation and delineation.

Chapter 4

Implications of Image Fusion on the Determination of Target Volumes

4.1 Introduction

This chapter presents clinical examples of the effect of employing multiple modalities on the definition of target volumes. For the three patients presented in the previous chapter, contours of the nidus were drawn by a neurosurgeon with different combinations of modalities in order to compare the target volumes. The delineation was performed by using (1) MR, (2) MR and SA, (3) SA, (4) MRA and MR and (5) MRA, MR and SA. Since the fifth case (5) employs all of the possible datasets, the target volume obtained with MRA, MR and SA is the reference volume to which the other four volumes are compared to. The overestimation and underestimation of the target volumes obtained with combinations (1) to (4) were evaluated for the three patients. Since target delineation is done manually, minor differences in volume (overestimation and underestimation) are introduced by the user due to reproducibility, however, these volume differences are considered to be insignificant with respect to the target volume. The centre of mass (COM) of each volume, which defines the target location, was evaluated for every volume. The COM of the reference volume was compared to the COM of the other volumes as well as to the previously obtained treatment target location (isocentre) determined with the method suggested by Henri *et al.* [58]. In order to illustrate the spatial distribution of the overestimation and underestimation in target volumes, the following steps have been done.

1. New 3D datasets were created with an intensity value of 0 for voxels outside the target contour and an intensity value of 1 for voxels inside the target contours, as shown in Figure 45.

2. Parallel ray-tracing was performed through the modified volumes (Figure 45) in order to get three projection images (one for each direction) for each volume. Since the intensity of the voxels inside (outside) the target contours equals 1 (0), the pixel intensity in the projection images illustrates the amount of voxels encountered along the path of each ray traced.

3. The ray-traced images were subtracted from the reference ray-traced image in order to determine the difference in the amount of voxels encountered by the ray path between the contours drawn with MRA, MR and SA and the contours drawn with a different

combination of modalities. Therefore, an underestimation in target volume is illustrated by positive pixel values whereas an overestimation is illustrated by negative pixel values.

Therefore, the location where the contours differ the most along the projection direction occur at the greatest pixel intensity absolute value. The difference in contours can then be observed on the corresponding image.

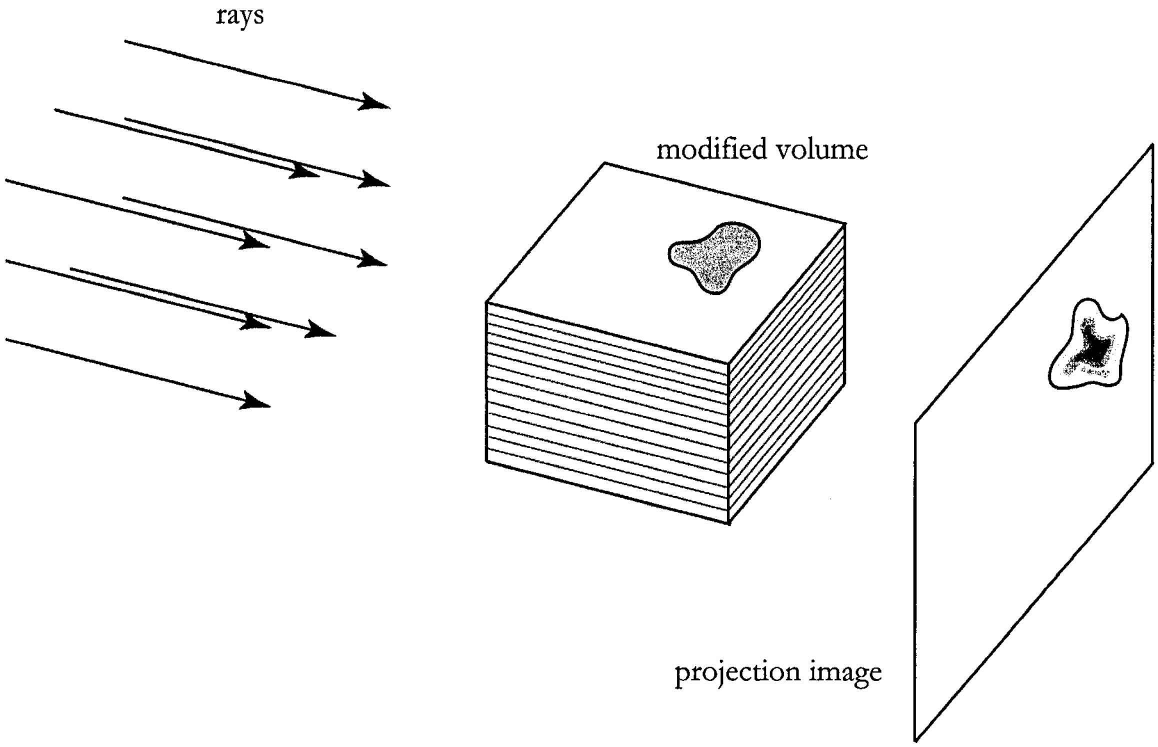

Figure 45. Ray-traced image through modified volume. The intensity of the voxels inside the target contours equals 1 (shaded area) and the intensity of the voxels outside the target contours equals 0 (white area). The pixel intensity in the projection images illustrates the amount of voxels encountered along the path of each ray traced.

4.2 Patient 1

For patient 1, the target volume comparison results are given in Table 1. A considerable underestimation in target volume is obtained when MRA images are not used in the delineation process. These results are in agreement with those of Bednarz *et al.* [18], which state that plans based on SA images do not completely cover the nidus as defined by the MRA images alone. The underestimation is maximal when SA contours are backprojected in order to reconstruct the target, once again illustrating the limitations of the technique. When MR and SA images are employed, the underestimation is much greater than with modality combinations which include MRA images. The MRA images therefore provide superior vasculature information than do the MR and SA images. The overestimation in target volumes obtained with the MR and SA images is negligible compared to the underestimation. Table 2 compares the COM of the reference target volume to that of the other target volumes as well as to the previously determined target location (treatment isocentre). As can be seen in the table, differences as small as 1.1 mm and as large as 4.8 mm were obtained. The target volume obtained with MRA and MR images, which gave (1) the least amount of underestimation and (2) the smallest difference in target location with respect to the reference, illustrates the usefulness of the MRA images for this patient. As for the previously determined target location, the coordinates are shown to be 4.8 mm off illustrating the limitations of the target localisation method and the usefulness of image fusion for this patient.

Table 1. Target volumes for patient 1. The reference volume is the one obtained with MRA, MR and SA. The overestimation and underestimation of target volumes for other modality combinations are given in columns 2 and 3.

Modalities employed	Volume (cm^3)	% Volume
MRA, MR and SA		
Reference	5.425	100.0
MR		
Overestimation	0.271	5.0
Underestimation	1.663	30.7
MR and SA		
Overestimation	0.157	2.9
Underestimation	2.096	38.6
SA		
Overestimation	0.65	12.0
Underestimation	2.256	41.6
MRA and MR		
Overestimation	0.276	5.1
Underestimation	1.223	22.5

Table 2. Target locations for patient 1. The volume obtained with MRA, MR and SA is considered to be the reference. The centre of mass (COM) of each volume was determined in order to evaluate the differences in target location. The reference target location is also compared to the previously determined target location (treatment isocentre).

Target localisation	Target location (x,y,z) in mm	RMS difference in mm
MRA, MR and SA (reference)	(80.9, 62.1, 89.6)	0.0
MR	(80.1, 62.1, 90.4)	1.1
MR and SA	(78.6, 62.1, 90.3)	2.4
SA	(78.2, 62.7, 91.7)	3.5
MRA and MR	(79.8, 62.2, 89.9)	1.1
Previously determined location	(77.3, 63.3, 92.5)	4.8

The projection images, described in the section 4.1, are illustrated in Figure 46. In general, an underestimation of the volumes, illustrated by positive pixel differences, is obtained. As can be seen in Figure 47 to Figure 51, the information provided by the modalities greatly influences the target delineation process. The contours drawn with MRA, MR and SA images cover a greater area than the ones drawn with (1) MR and SA, (2) MRA and MR, (3) MR and (4) SA images.

As can be seen in Figure 46a and Figure 47b, the contours drawn with MR and SA images underestimate the target volume by a considerable amount at the extremities along Y and in the upper X region. An overestimation of the target volume, on the other hand, is negligible (Table 1). The MRA images therefore provide vascular information which is not present on the MR and SA images. This can also be observed in Figure 48 in which additional tissue was included in the target volume at the extremities along Y and in the upper X region when MRA was added to the delineation process. Figure 48 also illustrates the results of Table 2 and Figure 46a in which the target volume COM was shifted towards the lower X region, resulting in an overall target location shift of 2.4 mm. The overestimation in target volume was negligible (Table 1). When the target was delineated with MRA and MR images, the lowest, yet considerable, underestimation of the target volume was obtained and was present at the extremities along Y and in the upper X region, as shown in Figure 46c and Figure 49.

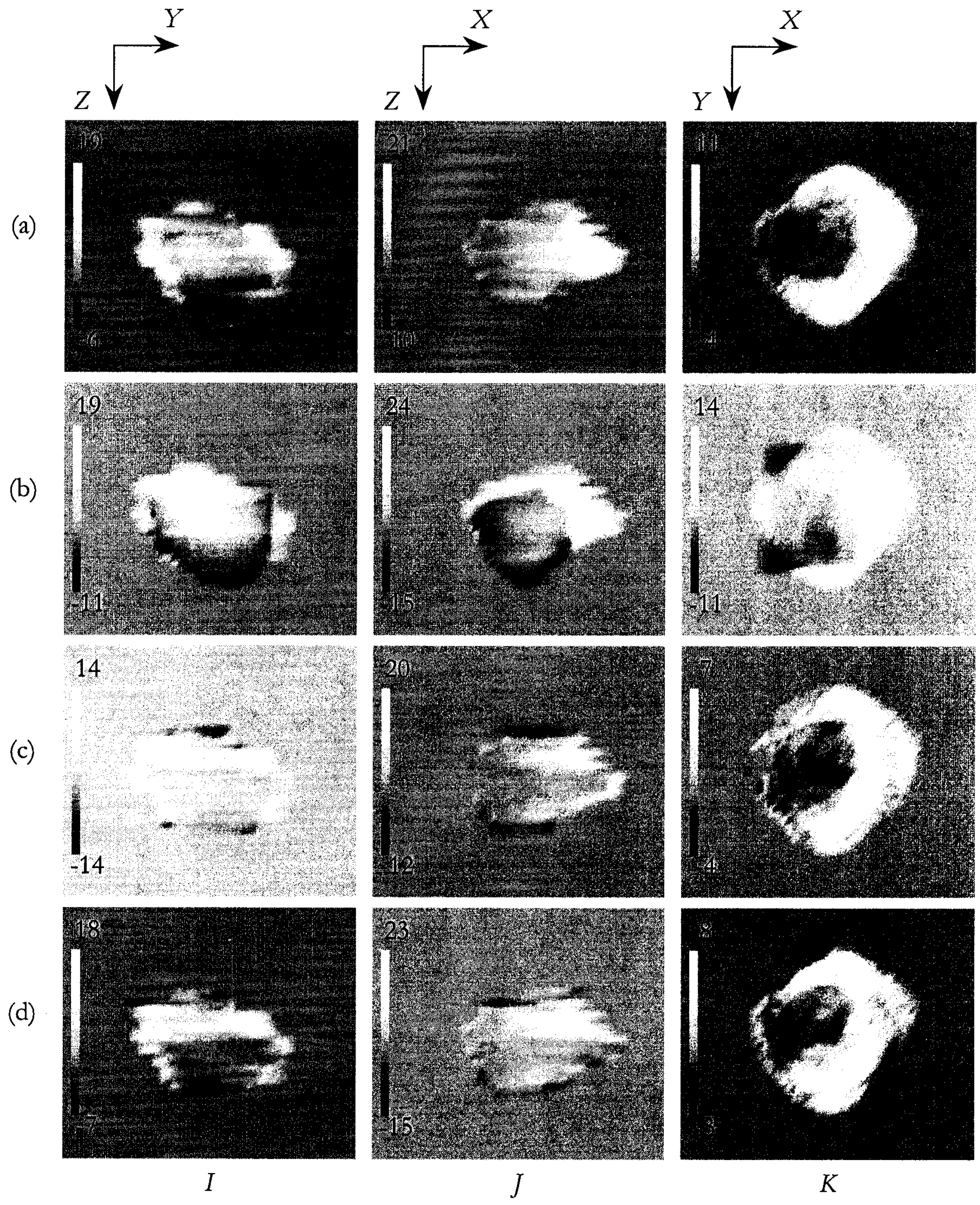

Figure 46. Subtracted ray-traced volumes for patient 1 along each orthogonal direction (I,J,K). The resulting images, obtained from subtraction of the (1) MR and SA, (2) SA, (3) MR and MRA and (4) MR ray-traced images from the reference ray-traced image, are given in rows (a), (b), (c) and (d) respectively. An underestimation in target volume is illustrated by the positive pixel values whereas an overestimation is illustrated by the negative pixel values. The stereotactic coordinate system (X,Y,Z) illustrates the regions of underestimation and overestimation.

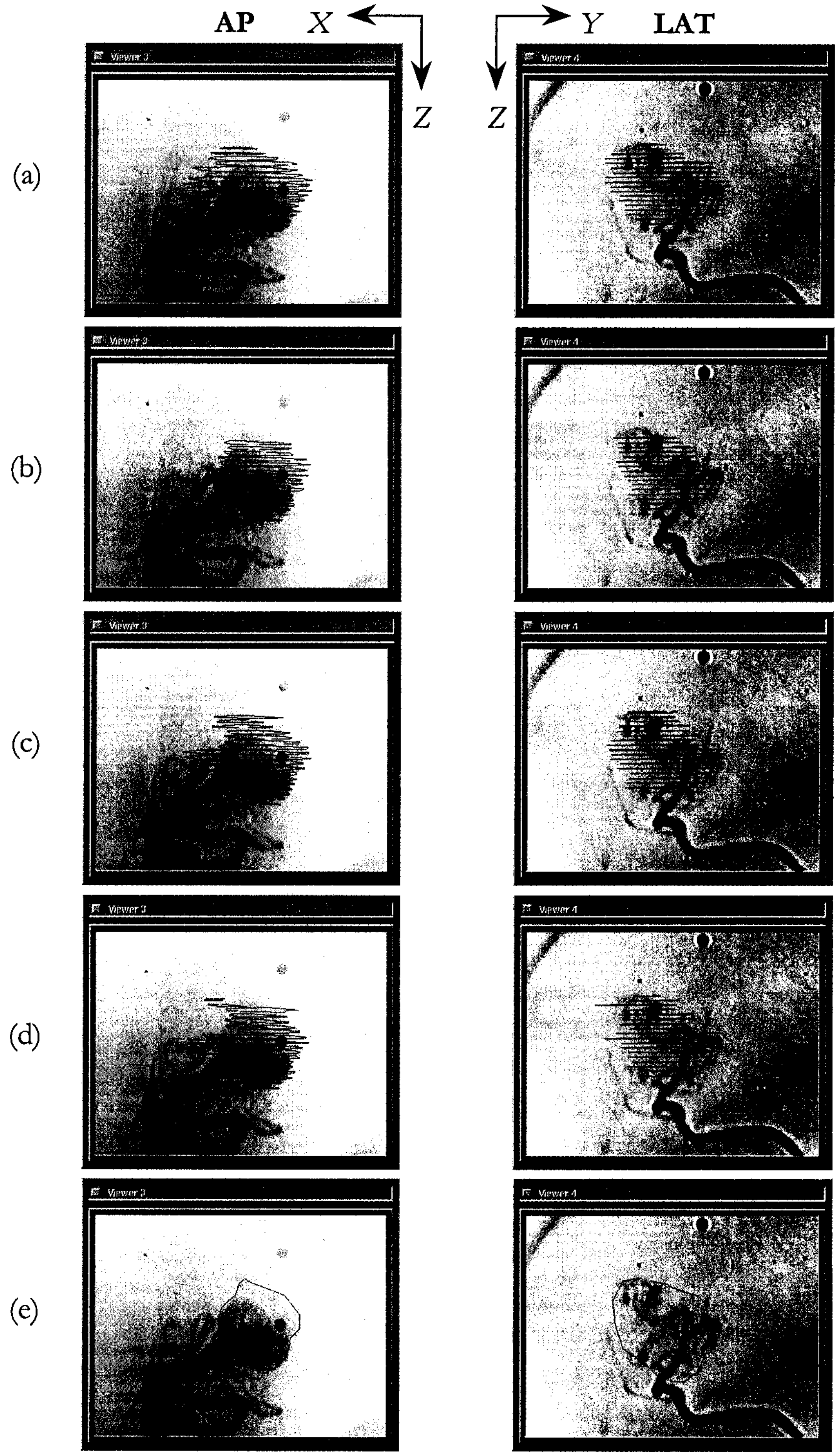

Figure 47. Comparison of contours on SA images. The contours drawn with (a) MRA, MR and SA, (b) MR and SA, (c) MRA and MR, (d) MR and (e) SA are shown for both views.

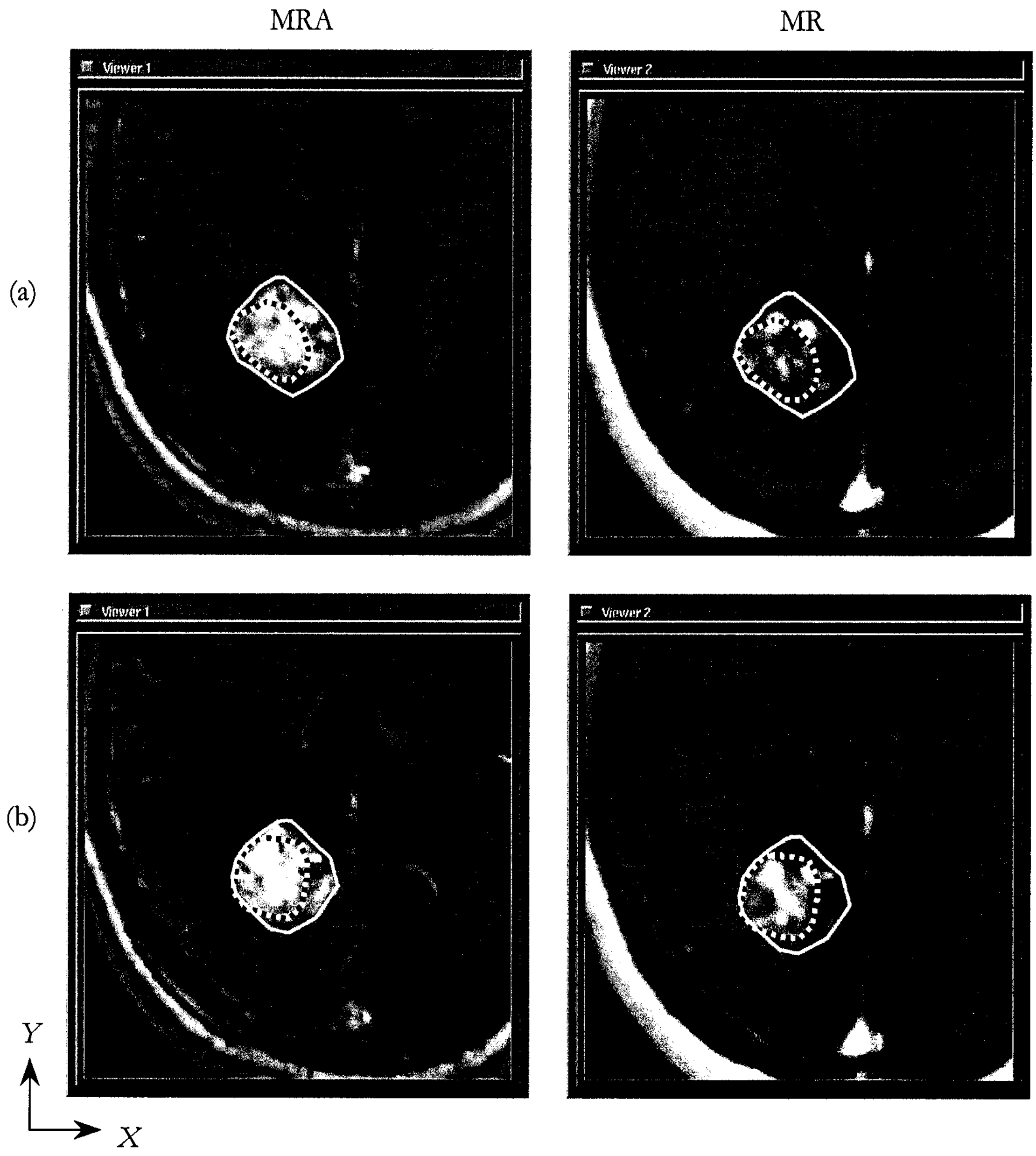

Figure 48. Comparison of contours on MRA and MR images. The contours drawn with (1) MRA, MR and SA and (2) MR and SA are illustrated as full and dashed lines respectively for two slices (a) and (b).

However, overestimation in target volume is negligible, as can be seen in Figure 49 and Table 1. The MRA images were therefore very useful in the target delineation process for this patient. As can be seen in Figure 49, the contours drawn on MRA and MR images seem

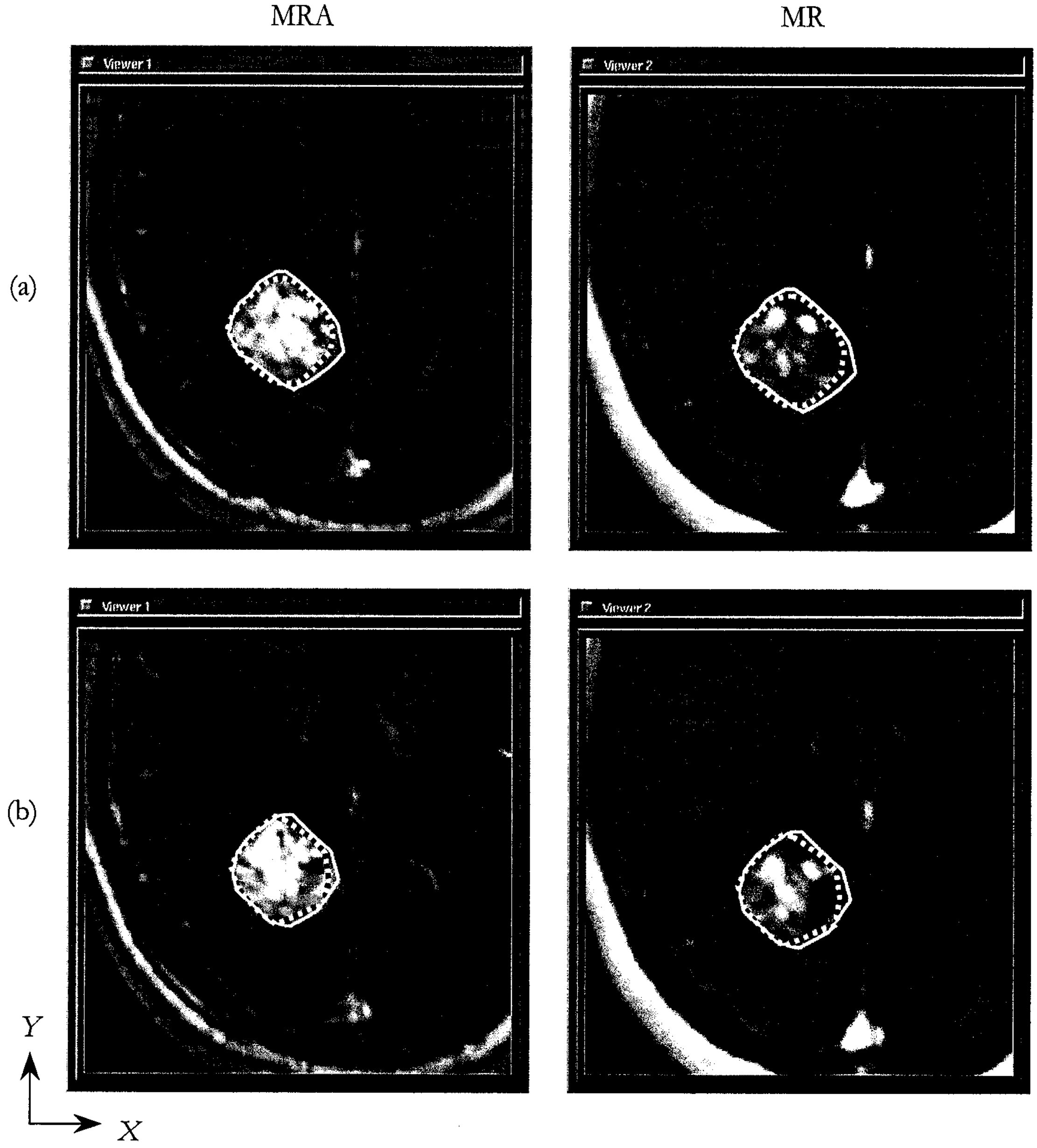

Figure 49. Comparison of contours on MRA and MR images. The contours drawn with (1) MRA, MR and SA and (2) MRA and MR are illustrated as full and dashed lines respectively for two slices (a) and (b).

centred on the reference contours. This confirms the difference in target volumes COMs resulting in a target location shift of 1.1 mm (Table 2).

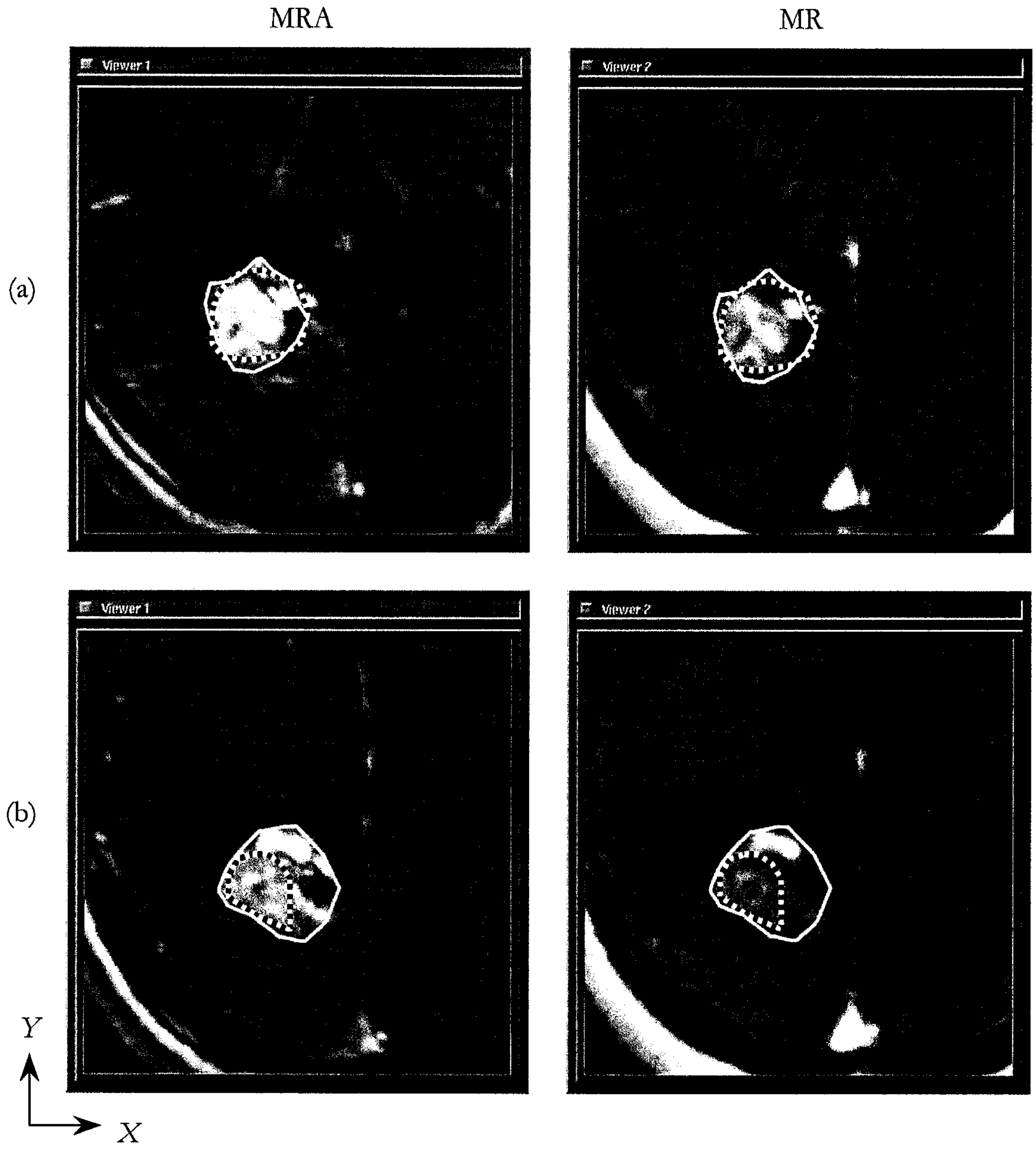

Figure 50. Comparison of contours on MRA and MR images. The contours drawn with (1) MRA, MR and SA and (2) MR are illustrated as full and dashed lines respectively for two slices (a) and (b).

As can be observed in Figure 47d, the contours drawn on MR images alone offers an underestimation in volume lower than the contours drawn with (1) MR and SA and (2) SA images, but yet considerable at the extremities along *Y* (Figure 46d). Some tissue, which was

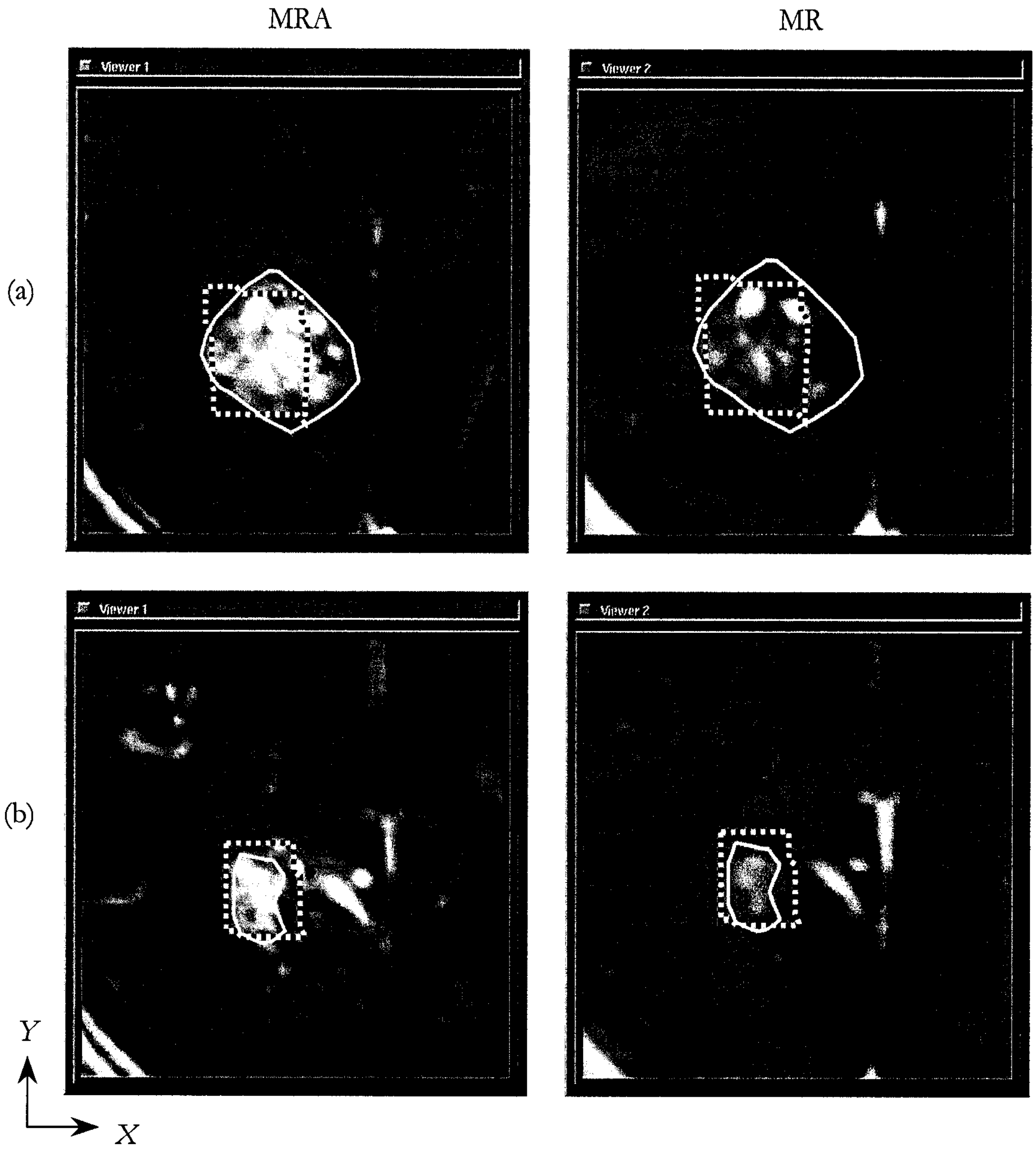

Figure 51. Comparison of contours on MRA and MR images. The contours drawn with (1) MRA, MR and SA and (2) SA are illustrated as full and dashed lines respectively for two slices (a) and (b).

excluded when MR and SA images were employed for the delineation process, was included when only MR images were used. Figure 50 illustrates the limitations of the delineation process employing MR images.

As can be seen in Figure 47e, the SA contours excluded tissue which was included when only MR images were employed for delineation. This tissue was included whenever SA images were not employed for the delineation process. For this patient, the SA images limited the analysis of target volumes when MRA images were not employed. In Figure 51, the overestimation and underestimation of the target volume are illustrated, showing the limitations of the backprojection technique. The underestimation is mostly obtained at the extremities along Y, in the upper X and the lower Z region while the overestimation was obtained mostly in the upper Z region, as can be seen in Figure 46b. This figure also confirms the shift in target volume COM with respect to the reference target volume COM given in Table 2.

For this patient, MRA was most useful in the delineation of the target volume. The MRA images increased the volume of the target as seen with the other modalities. The SA images were misleading when the MRA images were not employed for the delineation process. For this patient, the use of all modalities within the interactive fusion system was useful since, without it, considerable undercoverage of the target volume would be obtained.

4.3 Patient 2

For this patient, the target contours were drawn on (1) MRA, MR and SA, (2) MRA and MR, (3) MR and SA and (4) SA images. Due to the size of the target volume, the lesion was not visible on the MR images. The target volume comparison results are given in Table 3. Due to the differences in target volumes, the combination of MR, MRA and SA images is quite useful for the delineation process for this patient. Contrary to the results obtained for patient 2, when MRA images were employed without the SA images, greater overestimation of volume was obtained which suggests that the MRA images, when used alone, were misleading on the overall volume of the target. These results once again confirm those obtained by Bednarz *et al.* [18]. However, underestimation of the target volume is obtained in all cases. Table 4 compares the target locations and shows that differences of up to 2.7 mm were obtained when image fusion was not employed.

In Table 4, it can be seen that the differences between the centre of mass of the reference target volume and the other target volumes as well as with the previously determined target

Table 3. Target volumes for patient 2. The reference volume is the one obtained with MRA, MR and SA. The overestimation and underestimation of target volumes for other modality combinations are given in columns 2 and 3. For this patient, the AVM was not visible on MR alone.

Modalities employed	Volume (cm^3)	% Volume
MRA, MR and SA		
Reference	0.831	100.0
MR		
Overestimation	-----	-----
Underestimation	-----	-----
MR and SA		
Overestimation	0.150	18.1
Underestimation	0.250	30.1
SA		
Overestimation	0.255	30.7
Underestimation	0.316	38.0
MRA and MR		
Overestimation	0.327	39.4
Underestimation	0.167	20.1

Table 4. Target locations for patient 2. The volume obtained with MRA, MR and SA is considered to be the reference. The centre of mass (COM) of each volume was determined in order to evaluate the differences in target location. The reference target location is also compared to the previously determined target location (treatment isocentre). For this patient, the AVM was not visible on MR alone.

Target localisation	Target location (x,y,z) in mm	RMS difference in mm
MRA, MR and SA (reference)	(77.3, 79.5, 93.8)	0.0
MR	-----	-----
MR and SA	(76.4, 78.5, 94.7)	1.6
SA	(76.2, 79.1, 95.5)	2.1
MRA and MR	(77.3, 80.7, 94.6)	1.4
Previously determined location	(77.9, 80.7, 91.4)	2.7

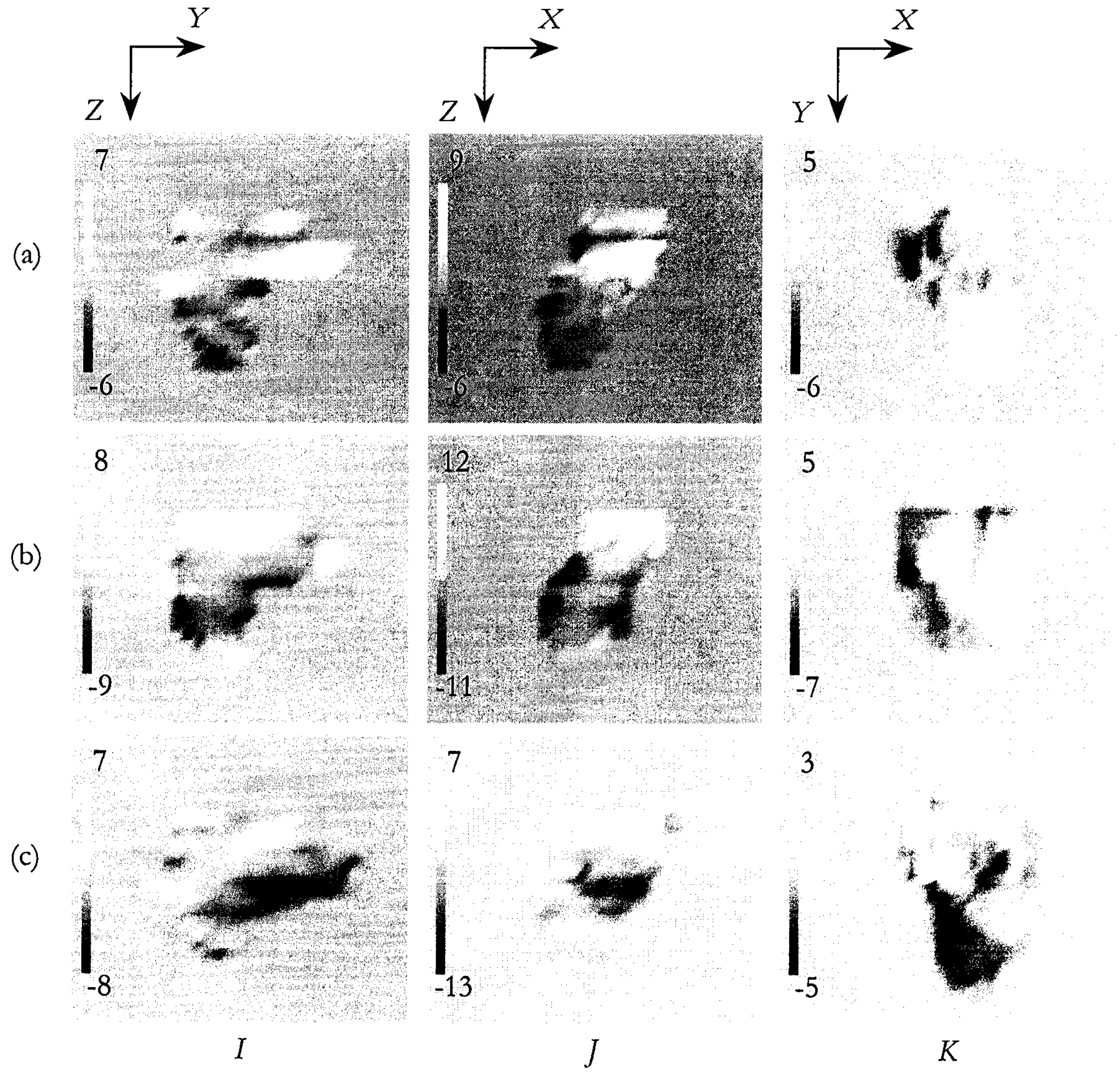

Figure 52. Subtracted ray-traced volumes for patient 2 along each orthogonal direction (I, J, K). The resulting images, obtained from subtraction of the (1) MR and SA, (2) SA and (3) MR and MRA ray-traced images from the reference ray-traced image, are given in rows (a), (b) and (c) respectively. An underestimation in target volume is illustrated by the positive pixel values whereas an overestimation is illustrated by the negative pixel values.

location (treatment isocentre) are less considerable than the ones obtained with the first patient. Nonetheless, these differences are still greater than 1 mm which is considered a clinically significant distance scale in radiosurgery [34].

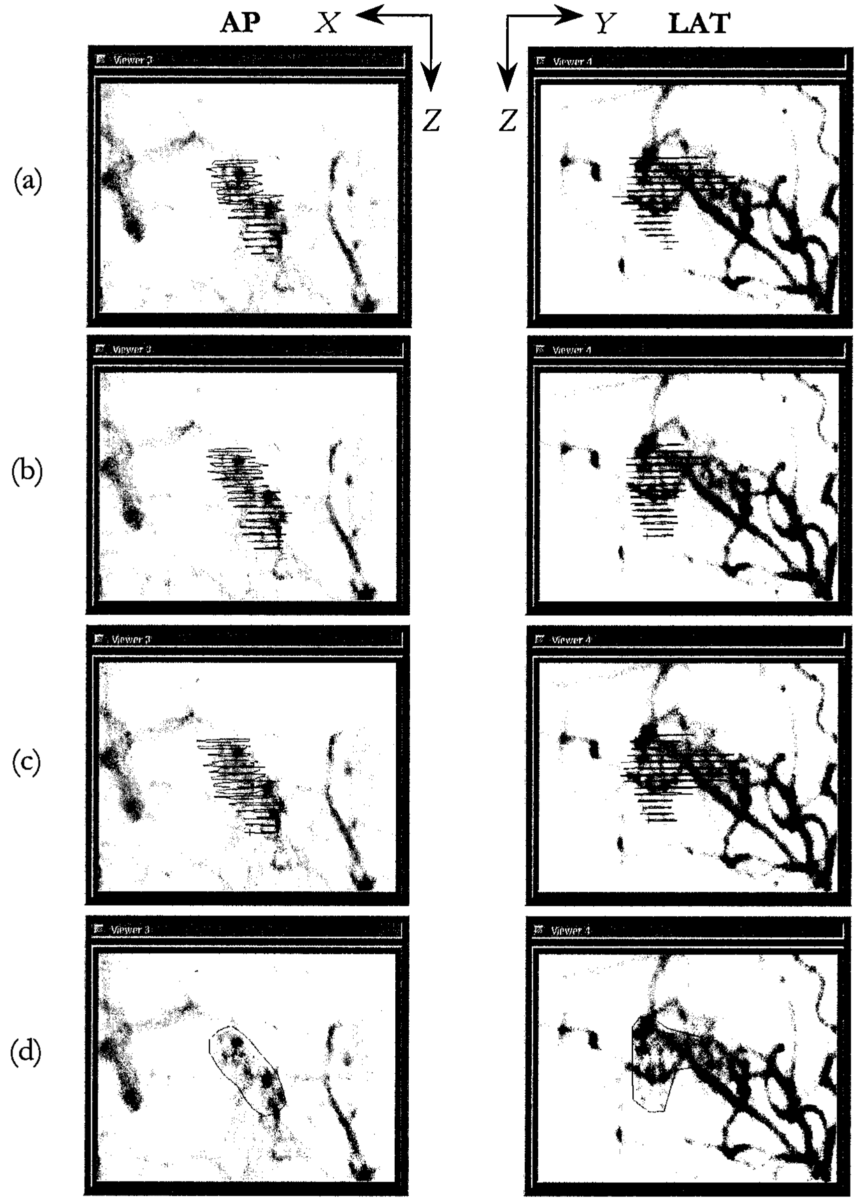

Figure 53. Comparison of contours on SA images. The contours drawn with (a) MRA, MR and SA, (b) MR and SA, (c) MRA and MR, (d) SA are shown for both views.

The projection images are illustrated in Figure 52. In Figure 53, the differences in target contour projections are more apparent on the LAT SA images. When MR and SA images were employed for target delineation, undercoverage was prevalent (Figure 54). As can be seen in the figure, the MRA images provided additional vascular information on the location and shape of the target. Figure 52a illustrates the underestimation and overestimation in target

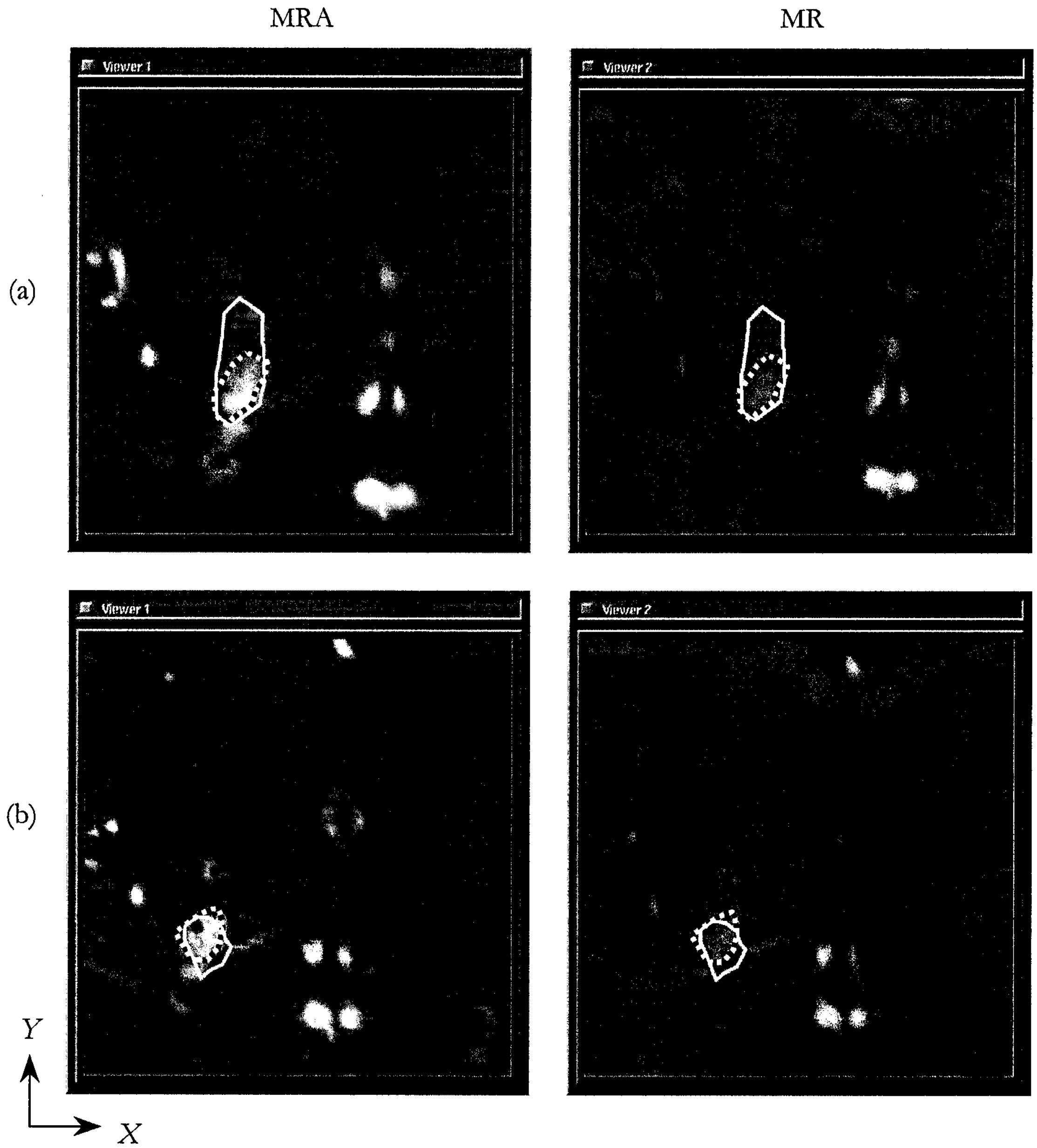

Figure 54. Comparison of contours on MRA and MR images. The contours drawn with (1) MRA, MR and SA and (2) MR and SA are illustrated as full and dashed lines respectively for two slices (a) and (b).

volume mostly in the upper *Y* and the lower *X* regions respectively. When the MRA and MR images were employed for the delineation process, overestimation was prevalent (Table 3). Figure 55 illustrates regions of underestimation and overestimation. Considerable

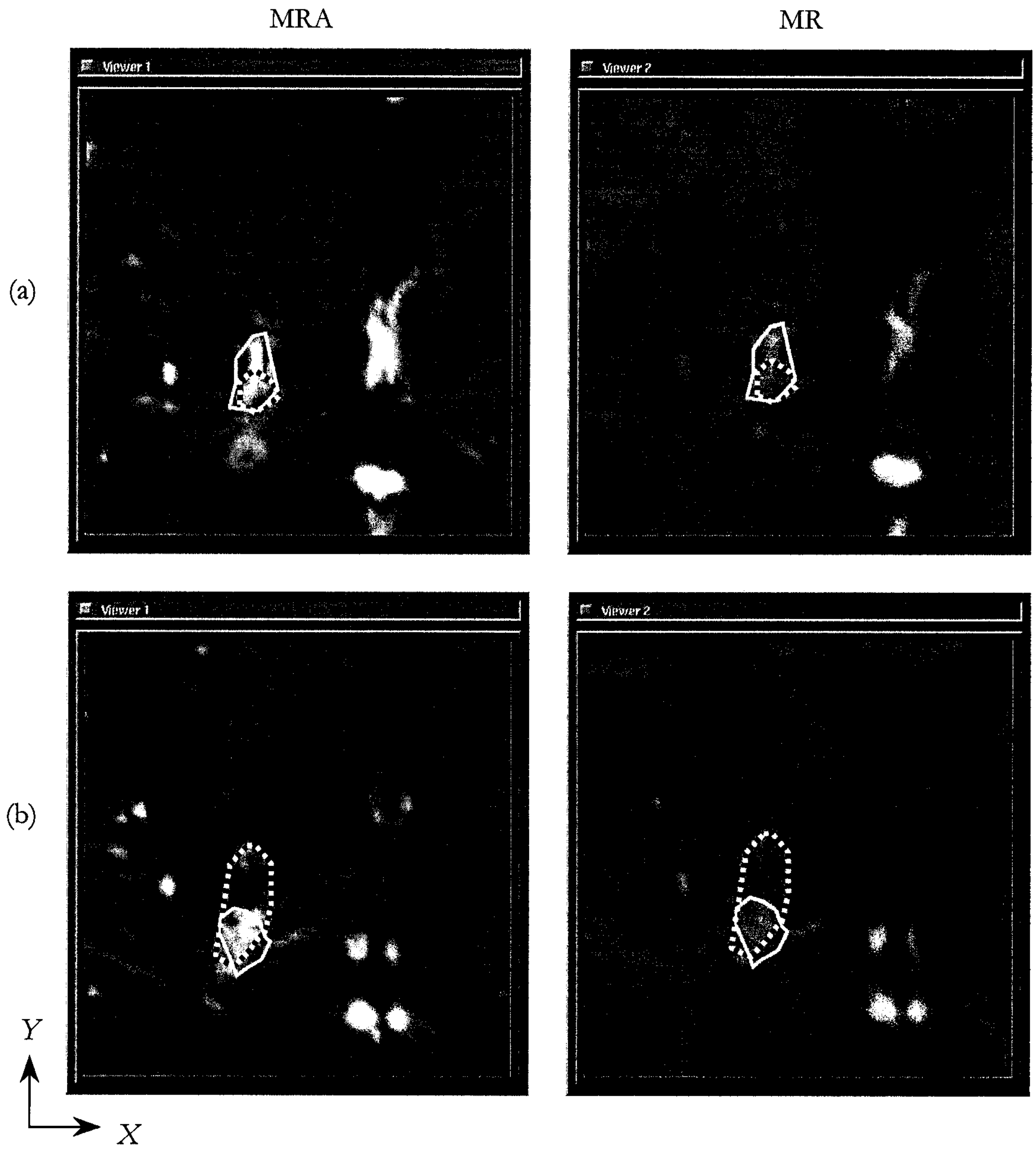

Figure 55. Comparison of contours on MRA and MR images. The contours drawn with (1) MRA, MR and SA and (2) MRA and MR are illustrated as full and dashed lines respectively for two slices (a) and (b).

underestimation in target volume was obtained in the lower Z and upper Y region, as can be seen in Figure 52c and Figure 55. The overestimation, on the other hand, is mostly observed in the upper Y region in the centre of the Z target extent. The SA images were therefore

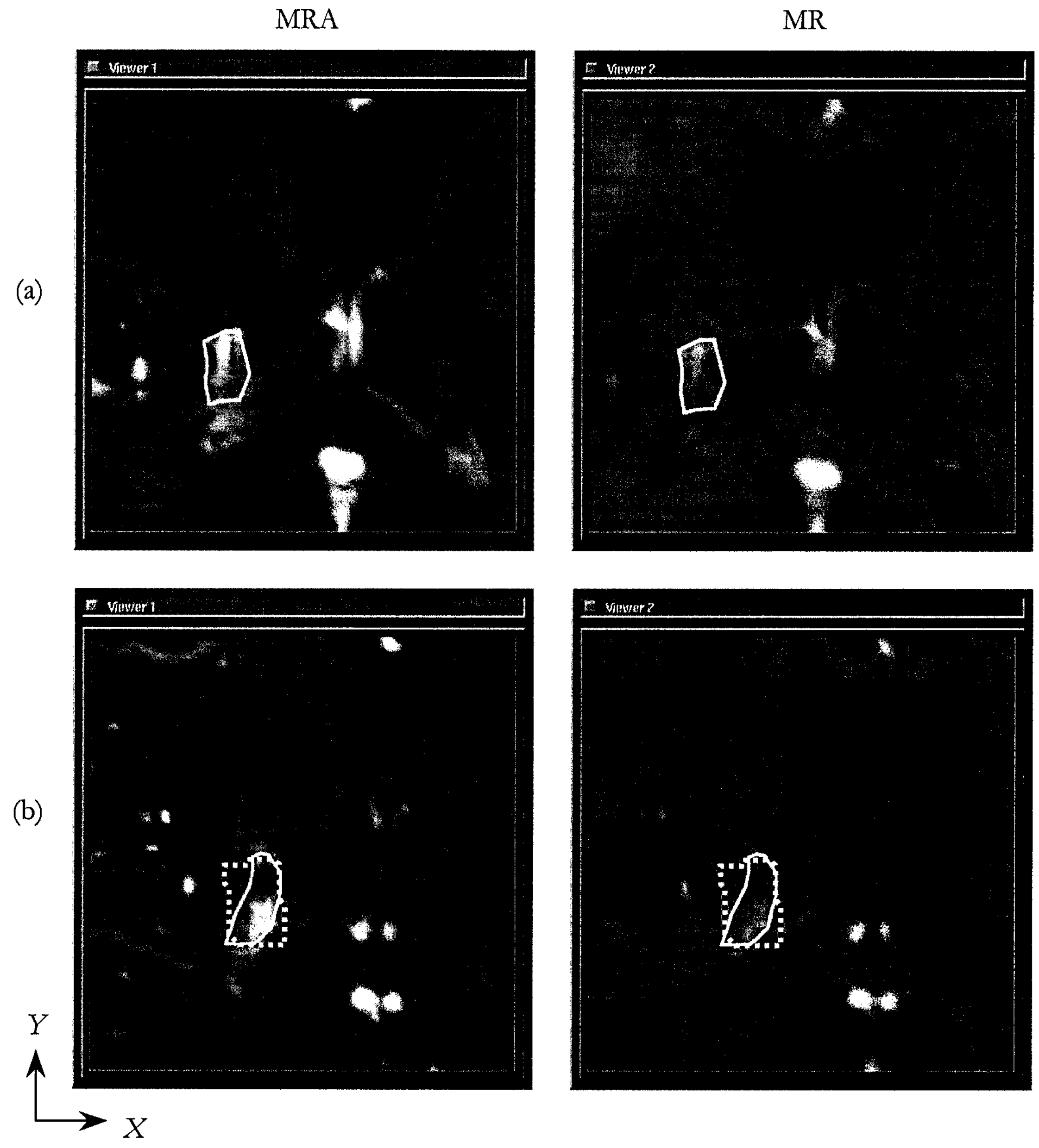

Figure 56. Comparison of contours on MRA and MR images. The contours drawn with (1) MRA, MR and SA and (2) SA are illustrated as full and dashed lines respectively for two slices (a) and (b). Slice (a) does not contain contours drawn with SA images only.

useful in the delineation process and helped guide the physician in the region of the lesion.

The results of the backprojection of the target contours drawn on the SA images are not promising since considerable underestimation and overestimation of the target volume are visualised in Figure 56. Figure 52b shows that the majority of the underestimation is located in the lower Z region, whereas the overestimation, in general, surrounds the target. In the image shown in Figure 56a, no contours were backprojected from the SA images and therefore considerable underestimation is obtained. This also confirms the target location shift in the Z direction given in Table 4. Figure 56b, on the other hand, illustrates overestimation of the target. This illustrates the limitations of SA contour backprojection technique.

For this patient, all modalities were useful for the definition of the target volume. The SA images guided the physician in the region of the lesion and the MRA images provided 3D vascular information not presented on the MR images. Since all modalities were equally employed for target delineation, the interactivity of the fusion system was useful. Considerable differences in the coverage of the target volume and sparing of healthy tissue were observed between the different combinations of imaging modalities.

4.4 Patient 3

This patient had undergone neurosurgery prior to radiosurgery. As mentioned in the previous chapter, metal clips were inserted in the region of the AVM which produced artefacts on MR/MRA images. Due to these artefacts and to the absence of vasculature information provided by MR images, the target could not be delineated on MR alone. On the MRA images, however, a portion of the target, which was not visible on the MR images, was visible in regions surrounding the artefacts. The SA images were therefore the most useful in the target delineation process. The target volume comparison results are given in Table 5. As can be seen in the table, an underestimation of the target volume is quite apparent when MRA and SA are not employed together. The MRA images therefore supplied additional information on the 3D shape and extent of the target and were useful complements to the SA images. In Table 6, the centre of mass of the target volume obtained with MRA, MR and SA is compared to the centre of mass of the target volumes obtained with (1) MR, (2) MR and SA, (3) SA, (4) MRA and MR as well as to the previously determined target location (treatment isocentre). As can be seen in the table, there are considerable differences between these values. These results illustrate the usefulness of image fusion for target localisation and delineation.

The projection images described in Section 4.1 are illustrated in Figure 57. The figure

Table 5. Target volumes for patient 3. The reference volume is the one obtained with MRA, MR and SA. The overestimation and underestimation of target volumes for other modality combinations are given in columns 2 and 3. For this patient, the AVM was not visible on MR alone.

Modalities employed	Volume (cm^3)	% Volume
MRA, MR and SA		
Reference	0.636	100.0
MR		
Overestimation	-----	-----
Underestimation	-----	-----
MR and SA		
Overestimation	0.093	14.6
Underestimation	0.579	91.0
SA		
Overestimation	0.051	8.0
Underestimation	0.544	85.5
MRA and MR		
Overestimation	0.023	3.6
Underestimation	0.586	92.1

Table 6. Target locations for patient 3. The volume obtained with MRA, MR and SA is considered to be the reference. The centre of mass of each volume was determined in order to evaluate the differences in target location. The reference target location is also compared to the previously determined target location (treatment isocentre). For this patient, the AVM was not visible on MR alone.

Target localisation	Target location (x,y,z) in mm	RMS difference in mm
MRA, MR and SA (reference)	(76.8, 59.4, 110.9)	0.0
MR	-----	-----
MR and SA	(76.4, 53.3, 110.4)	6.1
SA	(76.1, 54.1, 111.0)	5.3
MRA and MR	(76.0, 60.3, 114.0)	3.3
Previously determined location	(76.5, 57.3, 112.5)	2.7

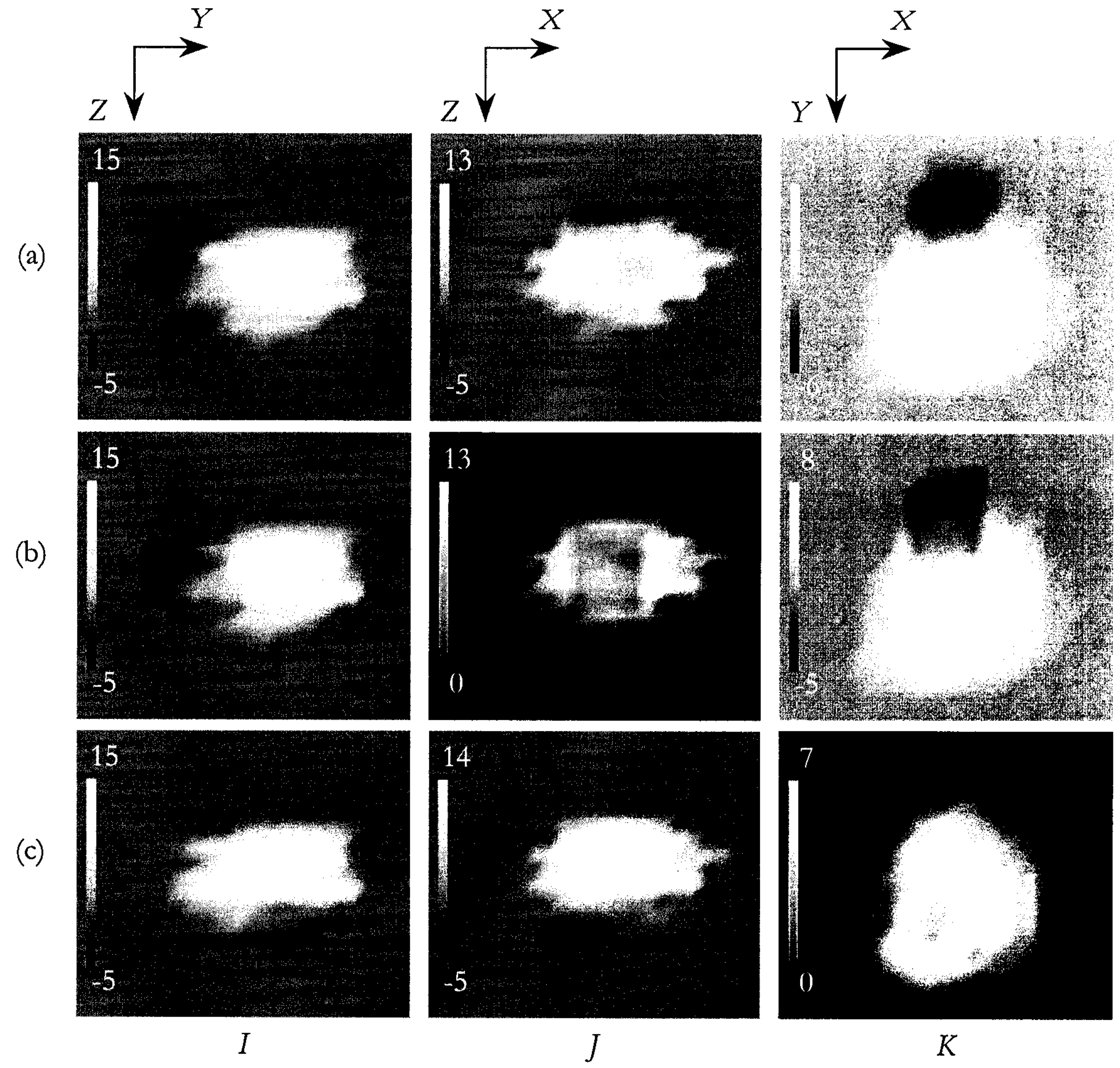

Figure 57. Subtracted ray-traced volumes for patient 3 along each orthogonal direction (I, J, K). The resulting images, obtained from subtraction of the (1) MR and SA, (2) SA and (3) MR and MRA ray-traced images from the reference ray-traced image, are given in rows (a), (b) and (c) respectively. An underestimation in target volume is illustrated by the positive pixel values whereas an overestimation is illustrated by the negative pixel values.

confirms the results of Table 5, which states that underestimation, illustrated by the positive pixel differences, is prevalent over overestimation, illustrated by the negative pixel differences. As can be seen in Figure 58 to Figure 61, the information provided by the modalities greatly influences the target delineation process. For this patient, the contours drawn with MRA, MR and SA images cover a greater area than the ones drawn with (1) MR and SA, (2) MRA and

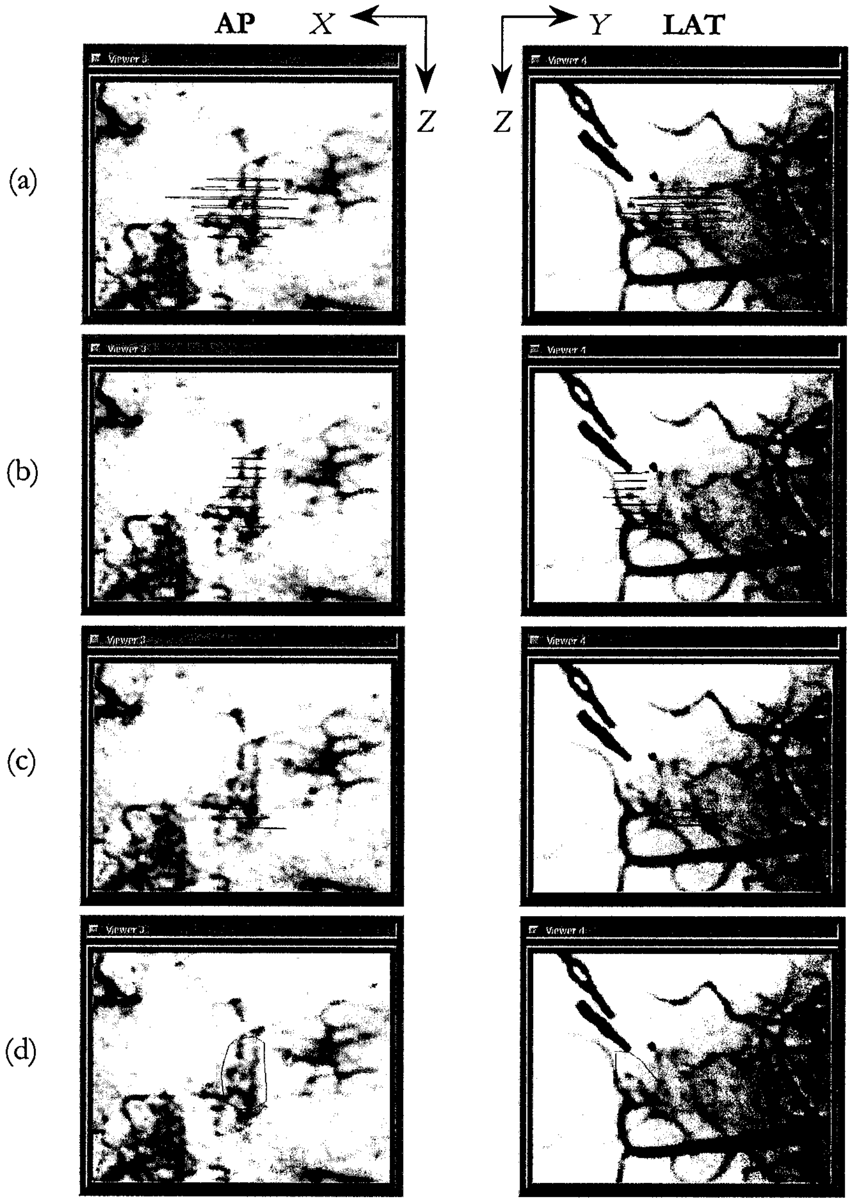

Figure 58. Comparison of contours on SA images. The contours drawn with (a) MRA, MR and SA, (b) MR and SA, (c) MRA and MR and (d) SA are shown for the AP and LAT views.

MR and (3) SA images. As can be seen in Figure 57a, the contours drawn with MR and SA greatly underestimate the target volume along X and along the upper Y region. This can also be seen in Figure 58b. The MRA images therefore provide vascular information which is not present on the MR and SA images. This can also be observed in Figure 59 in which additional

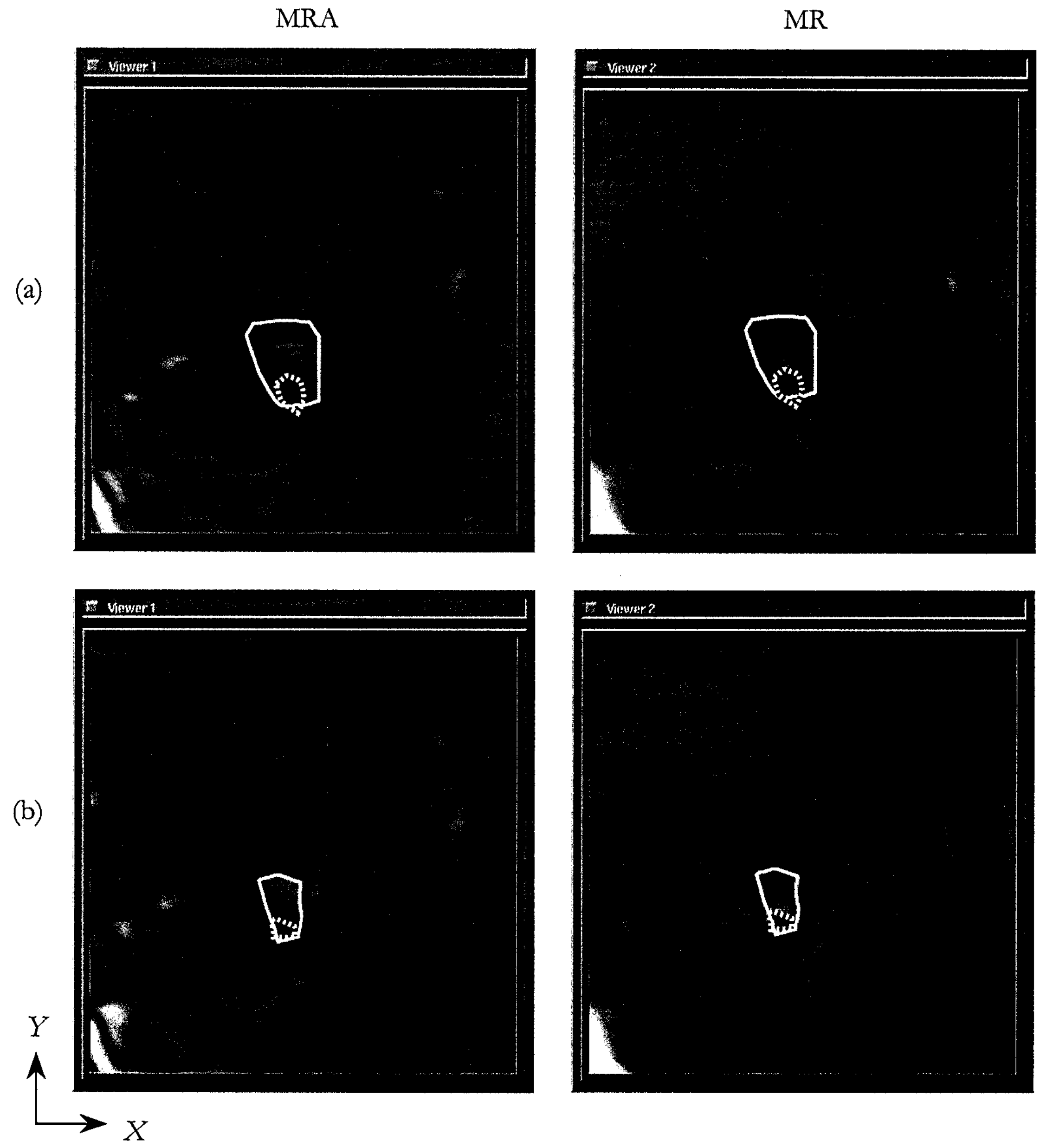

Figure 59. Comparison of contours on MRA and MR images. The contours drawn with (1) MRA, MR and SA and (2) MR and SA are illustrated as full and dashed lines respectively for two slices (a) and (b).

tissue was included in the target volume along *X* and along the upper *Y* region when all modalities were employed. The contours in Figure 59 also confirm the results obtained in Table 6 in which the centre of mass (COM) of the target volume obtained with MR and SA

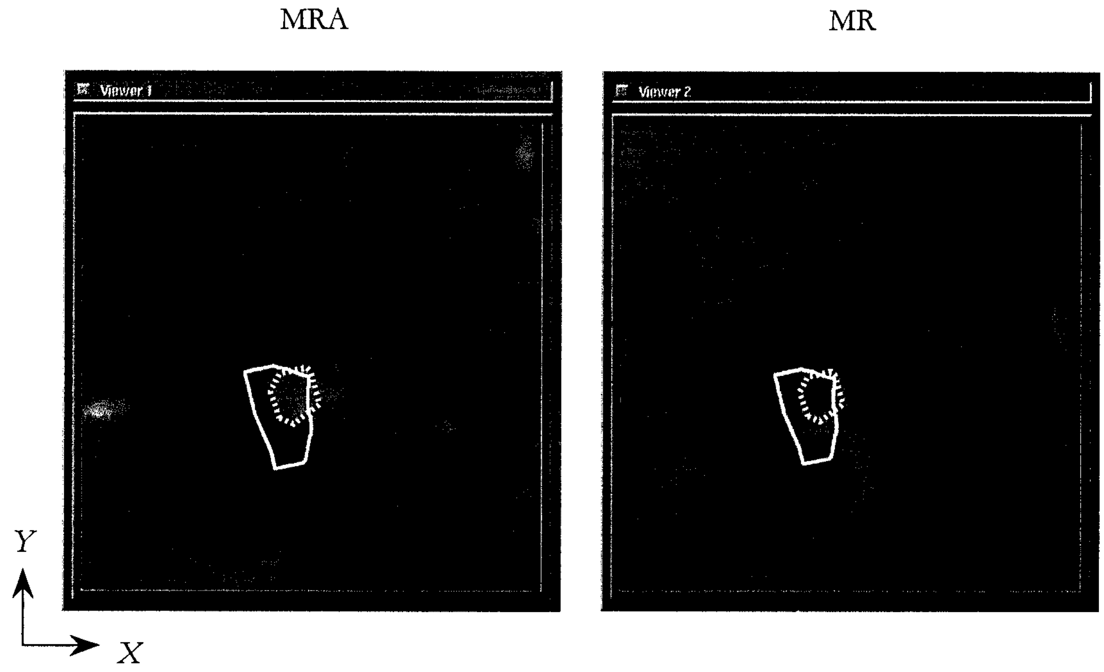

Figure 60. Comparison of contours on MRA and MR images. The contours drawn with (1) MRA, MR and SA and (2) MRA and MR are illustrated as full and dashed lines respectively.

images is shifted by a considerable amount of 6.1 mm towards the lower *Y* region compared to that of the reference COM. An underestimation of 91% target volume and a target location shift of 6.1 mm can have a considerable impact on the outcome of the radiosurgery treatment.

When MRA and MR images were employed, a considerable underestimation of the target volume along *X* and *Y* (Figure 57c), due to the MR artefacts, illustrates the limitations of MRA/MR images and the usefulness of SA images, especially when a patient had undergone neurosurgery with the insertion of permanent clips prior to radiosurgery (Figure 60). Figure 57c also illustrates an overestimation of the target volume in the upper *Z* region, resulting in a slight overestimation of 3.6% of the target volume (Table 5). Figure 58c also illustrates the shift in the target volume COM mostly towards the upper *Z* region, resulting in a total target location shift of 3.3 mm (Table 6). As can be observed in Figure 58d and Figure 61, the backprojection of contours drawn on SA images results in a considerable underestimation of the target volume along *X* and a slight overestimation along the lower *Y* direction. This is

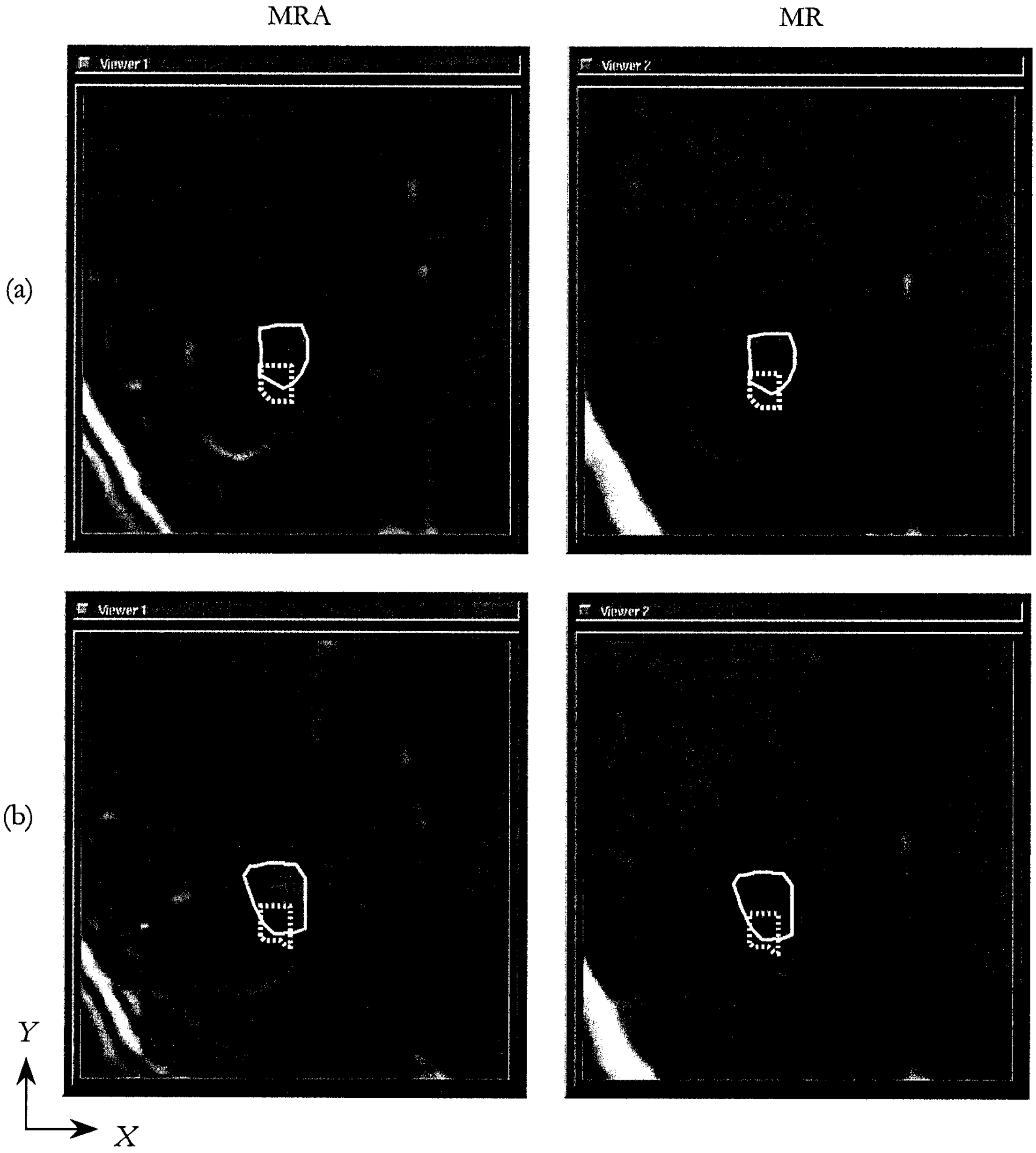

Figure 61. Comparison of contours on MRA and MR images. The contours drawn with (1) MRA, MR and SA and (2) SA are illustrated as full and dashed lines respectively for two slices (a) and (b).

confirmed in Figure 57b and in Table 5 and Table 6. Figure 61 also illustrates the shift in the target volume COM in the Y direction compared to that of the reference COM.

For this patient, all modalities have provided useful information not observed on other modalities. The MRA images have augmented the target volume when used in parallel with the SA images. The MR artefacts, however, greatly reduced the potential information provided by the MR modalities. For this patient, the interactivity provided by the fusion system was quite useful due to the presence of the image artefacts on the MR images. Without all modalities within this interactive system, considerable undercoverage of the target volume is obtained and the treatment plan would result in a treatment which would miss a large portion of the target. The shift in the COM of the target volumes can have a considerable impact on the outcome of the radiosurgery treatment.

4.5 Summary

The usefulness of employing all modalities for target volume definition has been presented in this chapter. Differences of up to 92.1% and 39.4% have been obtained for underestimation and overestimation of the target volume, respectively. Not employing all modalities for the delineation process seems to result in considerable underestimation of target volumes. Differences in target location are considerable when all modalities are not employed for the target localisation and delineation process.

For the first patient, overestimation was not an issue. Underestimation of the target volume was prevalent. The MRA images, which were the most useful images for the delineation process, increased the target volume which is in agreement with the results obtained by Bednarz *et al.* [18], which state that plans based on SA images do not completely cover the nidus as defined by the MRA images alone. The SA images were misleading when the MRA images were not employed for the delineation process. For this patient, the use of all imaging modalities within the interactive system was useful, since without it, considerable underestimation of the target volume was obtained.

For the second patient, all modalities were useful for the definition of the target volume. The SA images guided the physician in the surrounding region of the lesion and the MRA images provided additional vascular information. As a result, the fusion system had a great impact on the coverage of the target volume and sparing of healthy tissue.

For the third patient, due to prior surgery and the insertion of permanent clips which caused artefacts in the MR images, the SA images were most useful, however, the MRA images presented additional information as to the shape and the size of the target. Due to the MR artefacts, the interactivity of the fusion system was useful for 3D delineation. Not employing all imaging modalities within the fusion system resulted in considerable underestimation of the target volume.

Chapter 5

Implications of Image Fusion for Treatment Planning

5.1 Introduction

This chapter presents the dosimetric implications of employing multiple modalities for the drawing of the target contours. The treatments delivered to the three patients presented in Chapter 3 were evaluated. The dose distributions were computed for the previously determined isocentre position and cone size and were evaluated with respect to volumes (drawn with MRA, MR and SA images) determined in the previous chapter. Cumulative DVHs were computed in order to quantify the conformity of the treatment plan to the target volume. An acceptable treatment plan, employing the information given by the target DVH and healthy tissue DVH, (1) must cover close to 100% of the target volume and (2) must not include a healthy tissue volume superior to that of the covered target volume at the prescription isodose line. In order to evaluate the dosimetric implications of image fusion, an optimised treatment plan was determined employing the reference target contours and compared to the delivered plan.

5.2 Patient 1

5.2.1 Treatment

This patient was treated with a single isocentre using a 1.75 cm cone at (77.3, 63.3, 92.5) mm in frame space, and a dose of 20 Gy was prescribed to the 80% isodose line. The dose distribution was computed and overlaid on the reference target contours (Figure 62). As can be seen in Figure 62a, no target contour is present and therefore the treated area contained only healthy tissue. In Figure 62b, c and d, the extremities of the target along Y extent as well as the upper X region of the target have not been covered by the delivered treatment plan. The computed DVH, given in Figure 63, illustrates that 36% of the reference target volume is within the 80% (prescription) isodose surface. The volume of healthy tissue irradiated within the 80% isodose surface is 3% of the target volume. Since the plan covers only 36% of the target volume, it would have been considered unacceptable for the reference target contours and the treatment plan would have been modified. These results are in agreement with those obtained by Kondziolka *et al.* [64], which state that AVMs appear more spherical on SA images and are often irradiated with only one isocentre. This patient study is another example of the limitations of target localisation and delineation without image fusion.

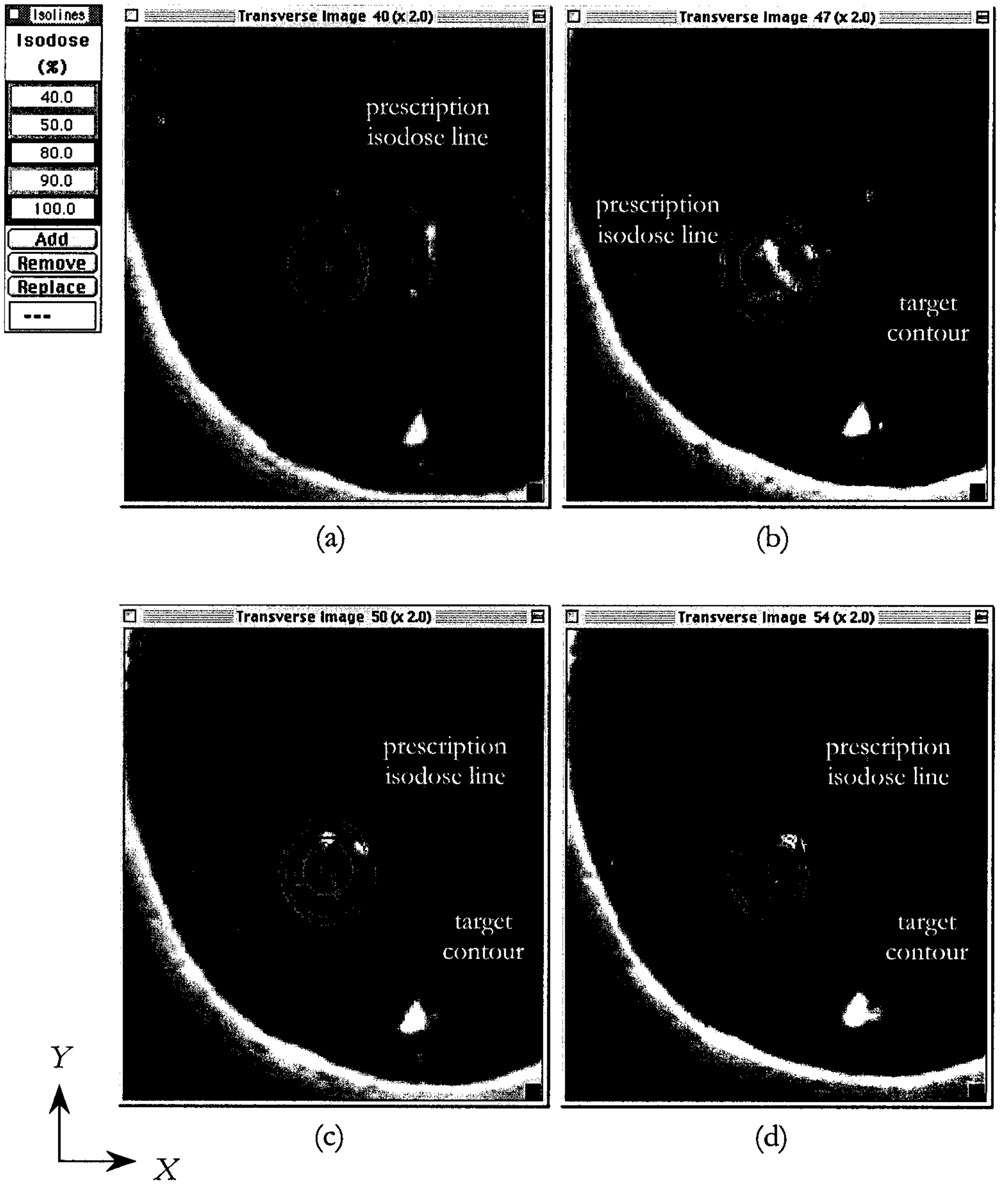

Figure 62. Comparison of isodose lines and reference target contours for the delivered treatment plan for patient 1. The target contour and prescription isodose line are shown by the full and dashed arrows respectively. As can be seen in (a), the treated area contains only healthy tissue. In (b), (c) and (d), the extremities of the target along Y as well as the upper X region of the target was excluded from the treatment.

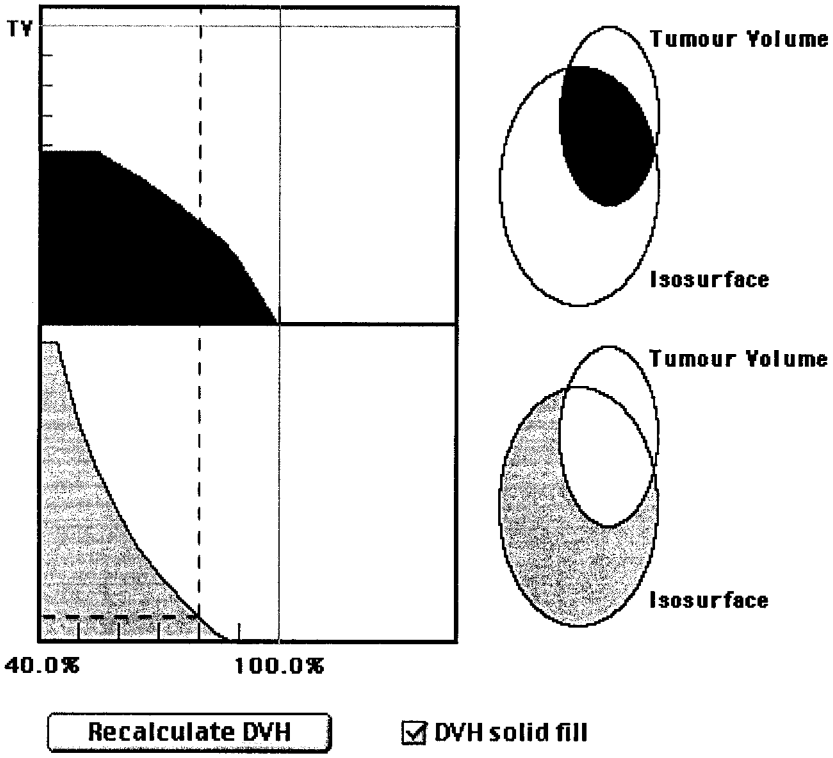

Figure 63. Cumulative dose volume histograms (target and surrounding healthy tissue) for the delivered treatment plan for patient 1. Only 36% of the target volume received a dose equal to or greater than the prescription dose at the 80% isodose surface. The volume of healthy tissue irradiated within the 80% isodose surface is 3% of the target volume.

5.2.2 Optimised treatment

Treatment plan optimisation was performed, employing the reference target contours, to improve the treatment plan. For this patient, eight isocentres were employed to increase the conformity of the dose to the complexly shaped target volume. These results confirm those obtained by Kondziolka *et al.* [64] which showed that between 2 and 10 isocentres were required to increase dose conformity when MRA images were used for target definition. The isocentre positions and cone sizes are given in Table 7. As can be seen in Figure 64, the conformity of the dose to the target volume greatly increased with the use of the eight isocentres. The extremities of the target along *Y* as well as the upper *X* region of the target volume, which was excluded in the delivered treatment plan, were consequently covered with the optimised plan. Since the 50% isodose surface conforms well to the target volume, the prescription isodose surface was chosen to be the 50% surface. The computed DVH is given in Figure 65. As can be seen, 100% of the target volume is within the 50% (prescription) isodose surface and the volume of healthy tissue irradiated within the 50% isodose surface is 73% of the target volume. This plan has therefore greatly increased the conformity of the dose to the target volume.

Table 7. Isocentre positions and cone sizes for optimised and delivered treatment plans for patient 1.

Plan	Location (x,y,z) in mm	Cone size in cm
Optimised		
Isocentre 1	(82.2, 61.9, 89.8)	2.25
Isocentre 2	(81.7, 72.4, 91.5)	0.75
Isocentre 3	(71.7, 68.8, 91.5)	0.75
Isocentre 4	(74.0, 59.1, 96.2)	0.50
Isocentre 5	(91.4, 60.1, 88.7)	1.00
Isocentre 6	(86.2, 51.1, 86.7)	0.50
Isocentre 7	(70.7, 59.7, 86.7)	0.50
Isocentre 8	(77.2, 51.2, 83.9)	0.50
Delivered treatment		
Isocentre 1	(77.3, 63.3, 92.5)	1.75

5.3 Patient 2

5.3.1 Treatment

This patient was treated with a single isocentre at (77.9, 80.7, 91.4) mm in frame space using a 1.25 cm cone, and a dose of 20 Gy was prescribed to the 80% isodose line. The dose distribution was computed and overlaid on the reference target contours Figure 66. As can be seen in Figure 66a, the lower X and Y region was not covered by the treatment plan. In Figure 66b and c, the lower Y region of the target was not covered, whereas in Figure 66d, the treated area contains only healthy tissue. The computed DVH, given in Figure 67, illustrates

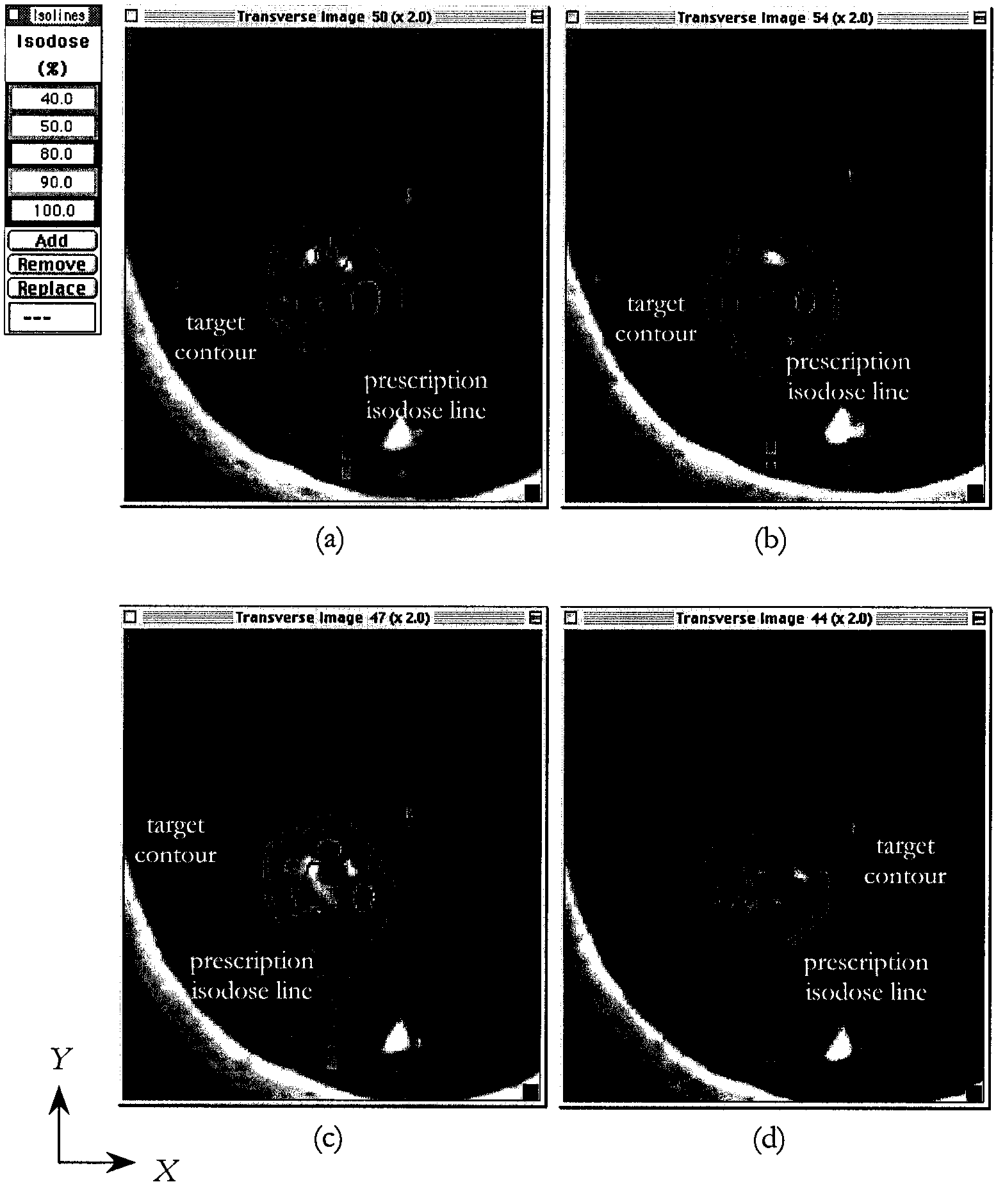

Figure 64. Comparison of isodose lines and reference target contours for the optimised treatment plan for patient 1. The target contour and prescription isodose line are shown by the full and dashed arrows respectively. The extremities of the target along Y as well as the upper X region of the target, which was excluded in the delivered treatment plan, is covered by the optimised plan.

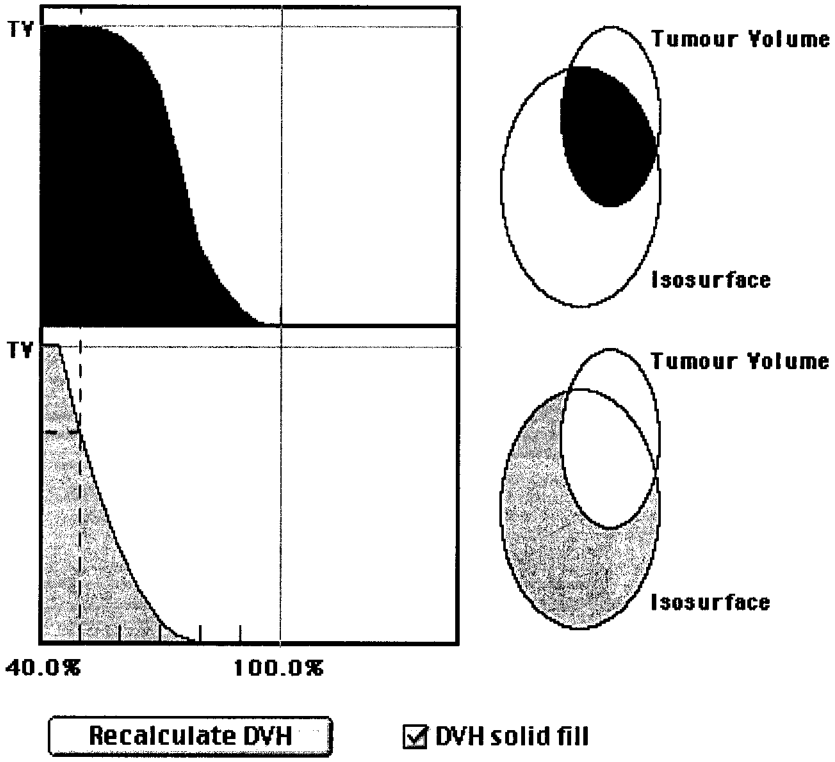

Figure 65. Cumulative dose volume histograms (target and surrounding healthy tissue) for the optimised treatment plan for patient 1. 100% of the target volume is within the 50% (prescription) isodose surface. The volume of healthy tissue irradiated within the 50% isodose surface is 73% of the target volume.

that 50% of the reference target volume is within the 80% (prescription) isodose surface. The volume of healthy tissue irradiated within the 80% isodose surface is 40% of the target volume. If this information were provided prior to the treatment, this plan would have been considered unacceptable since only 50% of the target volume is covered. These results once again confirm those obtained by Kondziolka *et al.* [64] stating that AVMs appear more spherical on SA images.

5.3.2 Optimised treatment

Treatment plan optimisation was performed in order to increase the conformity of the dose to the target volume. For this patient, four isocentres were sufficient to improve the dose distributions by increasing the dose conformity within the acceptable limits. The number of

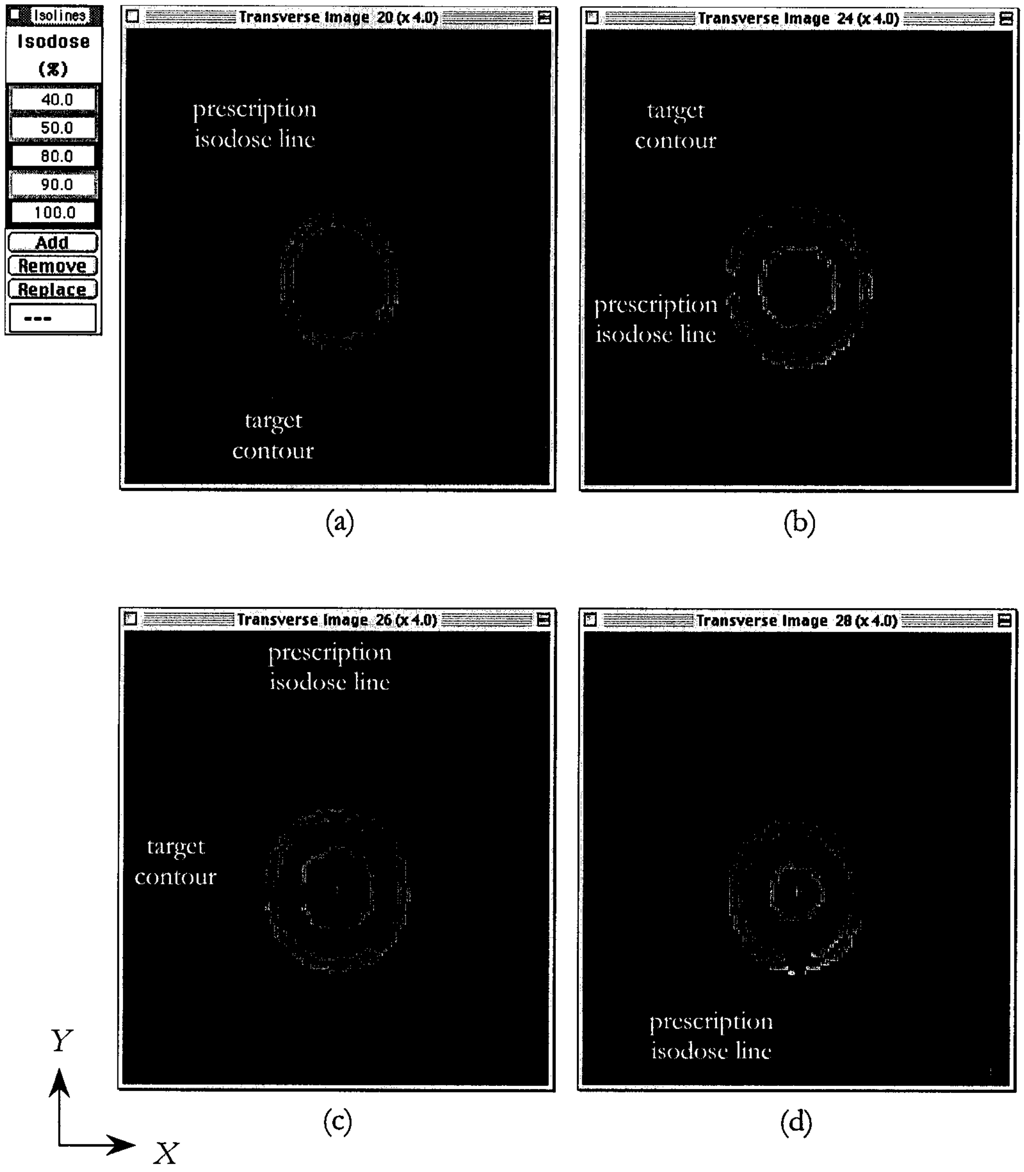

(a) (b)

(c) (d)

Figure 66. Comparison of isodose lines and reference target contours for the delivered treatment plan for patient 2. The target contour and prescription isodose line are shown by the full and dashed arrows respectively. As can be seen in (a), the lower X and lower Y region of the target was not covered by the plan. In (b) and (c), the lower Y region of the target was not covered. In (d), the treated area contains only healthy tissue.

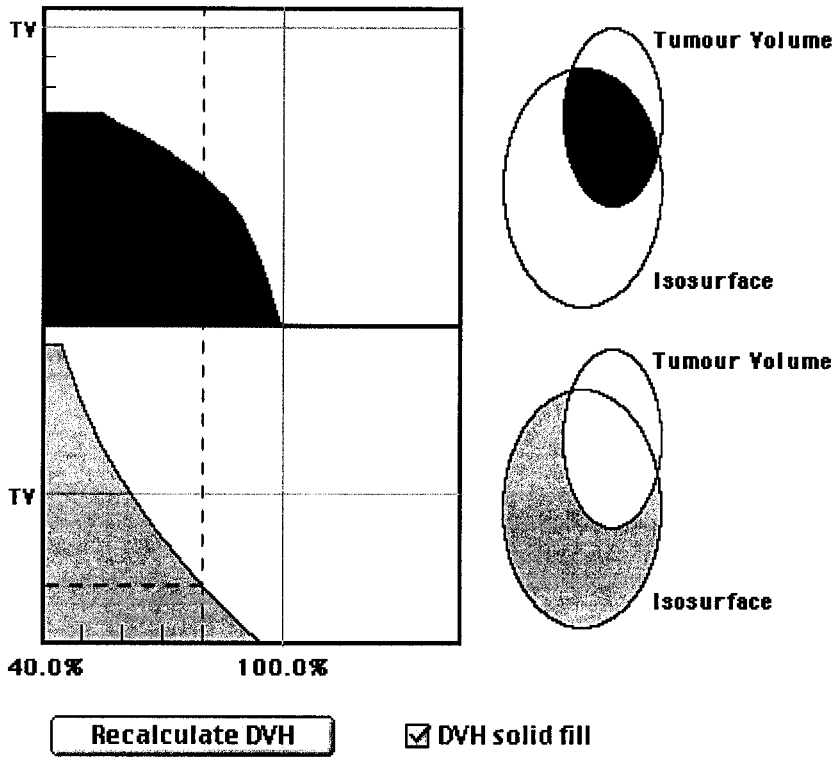

Figure 67. Cumulative dose volume histograms (target and surrounding healthy tissue) for the delivered treatment plan for patient 2. Only 50% of the target volume received a dose equal to or greater than the prescription dose at the 80% isodose surface. The volume of healthy tissue irradiated within the 80% isodose surface is 40% of the target volume.

Table 8. Isocentre positions and cone sizes for optimised and delivered treatment plans for patient 2.

Plan	Location (x,y,z) in mm	Cone size in cm
Optimised		
Isocentre 1	(74.2, 78.2, 100.4)	0.75
Isocentre 2	(76.2, 75.5, 93.8)	0.75
Isocentre 3	(79.2, 86.8, 91.4)	0.75
Isocentre 4	(78.4, 79.0, 89.8)	0.50
Delivered treatment		
Isocentre 1	(77.9, 80.7, 91.4)	1.25

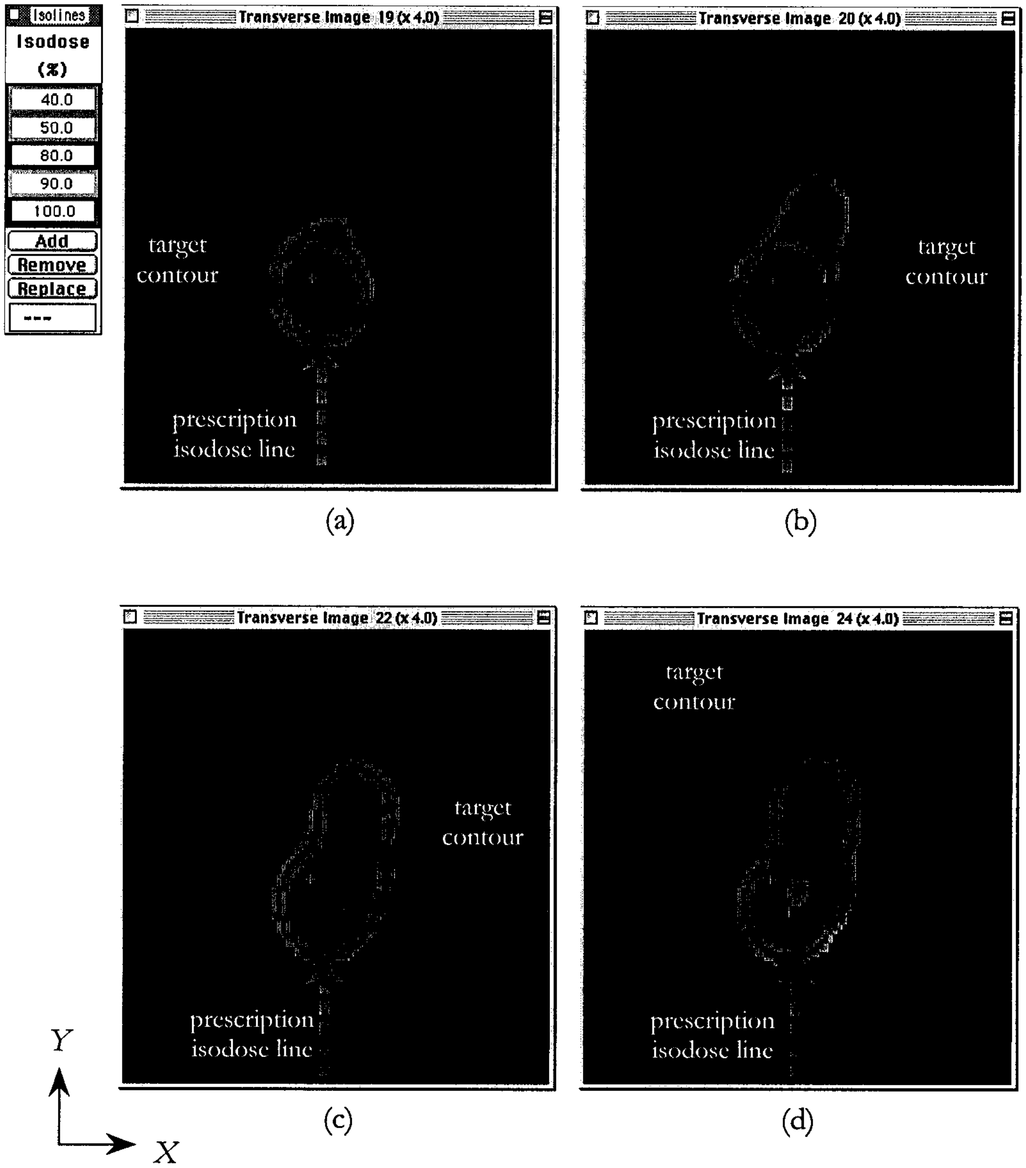

Figure 68. Comparison of isodose lines and reference target contours for the optimised treatment plan for patient 2. The target contour and prescription isodose line are shown by the full and dashed arrows respectively. The regions untreated with the delivered treatment plan are treated with the optimised treatment plan.

isocentres required to increase dose conformity is within the range obtained by Kondziolka *et al.* [64]. The isocentre positions and cone sizes are given in Table 8. Figure 68 shows the increase in the conformity of the dose to the target volume. The four isocentres have treated the areas untreated with the delivered treatment plan. Since 50% isodose surface conforms well to the target volume, it was chosen as the prescription isodose surface. The computed DVH, given in Figure 69, illustrates that 98% of the target volume is within the 50% (prescription) isodose surface and that the volume of healthy tissue irradiated within the 50% isodose surface is 97% of the target volume, which is within the acceptable limits.

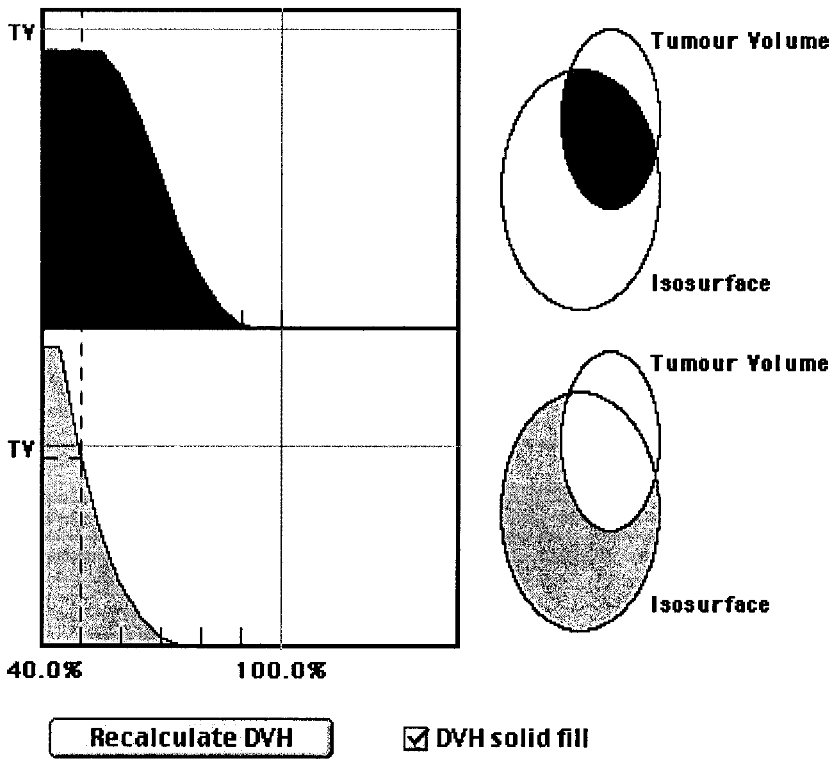

Figure 69. Cumulative dose volume histograms (target and surrounding healthy tissue) for the optimised treatment plan for patient 2. 98% of the target volume is within the 50% (prescription) isodose surface. The volume of healthy tissue irradiated within the 50% isodose surface is 97% of the target volume.

5.4 Patient 3

5.4.1 Treatment

This patient was treated with a single isocentre at (76.5, 57.3, 112.5) mm in frame space using a 1.25 cm cone, and a dose of 20 Gy was prescribed to the 85% isodose line. The dose distribution was computed and overlaid on the reference target contours (Figure 70). As can be seen in the figure, the upper Y region of the target was excluded from the treatment. On the image shown in Figure 70d, the treated area contains only healthy tissue. The computed DVH, given in Figure 71, illustrates that 57% of the reference target volume is within the 85% (prescription) isodose surface. The volume of healthy tissue irradiated within the 85% isodose surface is 29% of the target volume. Since the plan covers only 57% of the target volume, it would have been considered unacceptable for the reference target contours and the treatment plan would have been modified. These results once again confirm those obtained by Kondziolka *et al.* [64]. This illustrates the dosimetric consequences due to the limitations of localisation and delineation methods when image fusion is not employed.

5.4.2 Optimised treatment

Treatment plan optimisation was performed in order to verify if the treatment plan could have been greatly improved if the reference target contours would have been provided. For this patient, three isocentres were employed to increase the conformity of the dose to the target volume. The isocentre positions and cone sizes are given in Table 9. As can be seen in Figure 72, the conformity of the dose to the target volume is greater for the optimised treatment plan than for the treatment delivered to the patient (Figure 70). The upper Y region of the target volume, which was excluded in the delivered treatment plan, is now covered with the optimised plan. When more than one isocentre is employed, the dose is prescribed at lower isodose surfaces than that when one isocentre is used since the maximum dose is usually located near the intersection region of the cones and therefore does not conform to the target volume. For this patient, the 50% isodose surface conformed well to the target volume and therefore was chosen as the prescription surface. The computed DVH, given in Figure 73, illustrates that 98% of the target volume is within the 50% (prescription) isodose surface. The volume of healthy tissue irradiated within the 50% isodose surface is 91% of the target volume. The plan was therefore greatly improved with the use of multiple isocentres and the reference target contours.

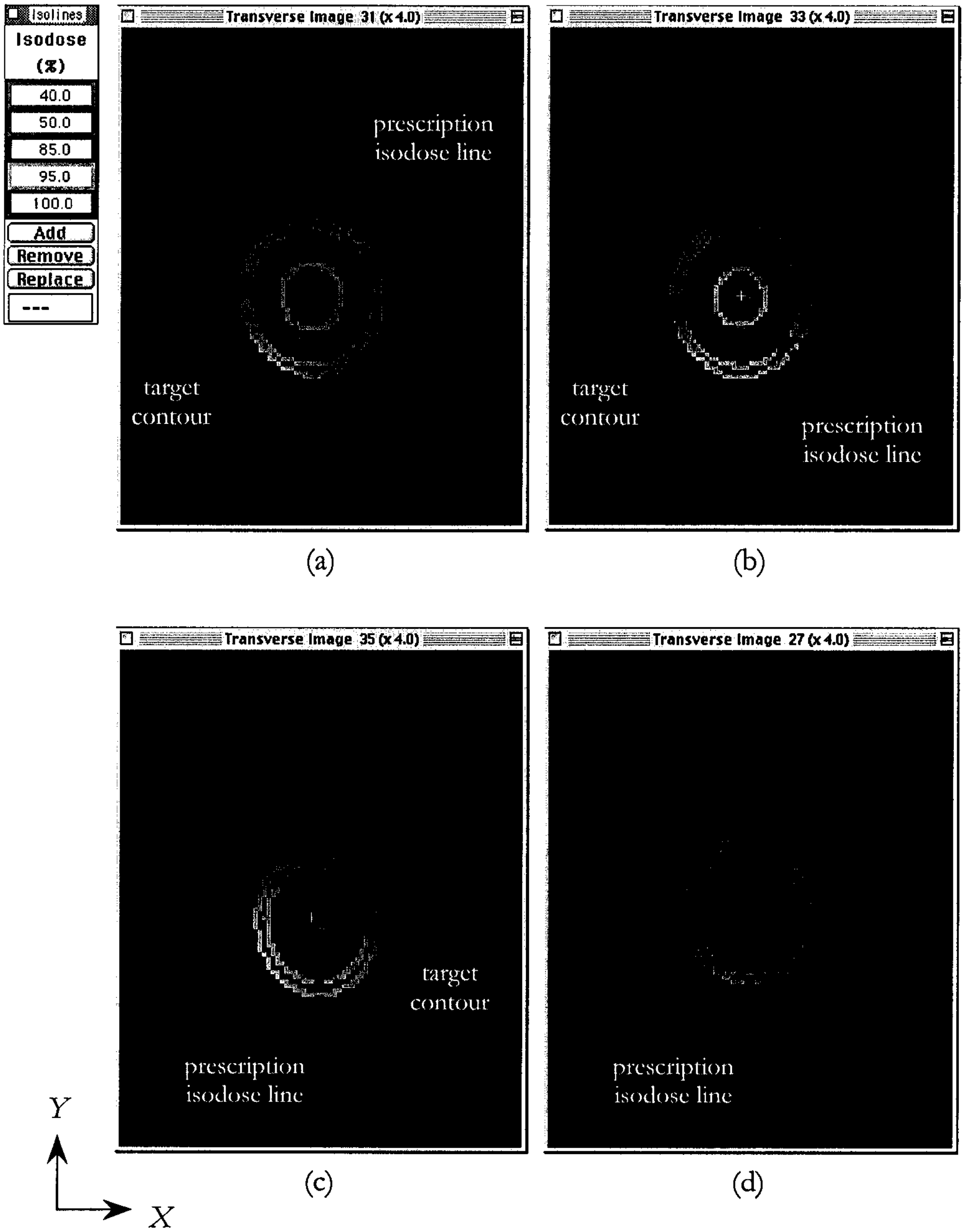

(a) (b)

(c) (d)

Figure 70. Comparison of isodose lines and reference target contours for the delivered treatment plan for patient 3. The target contour and prescription isodose line are shown by the full and dashed arrows respectively. As can be seen in (a), (b) and (c), the upper *Y* region of the target was excluded from the treatment. In d), there is no target contour, and yet, a part of the treated volume is present.

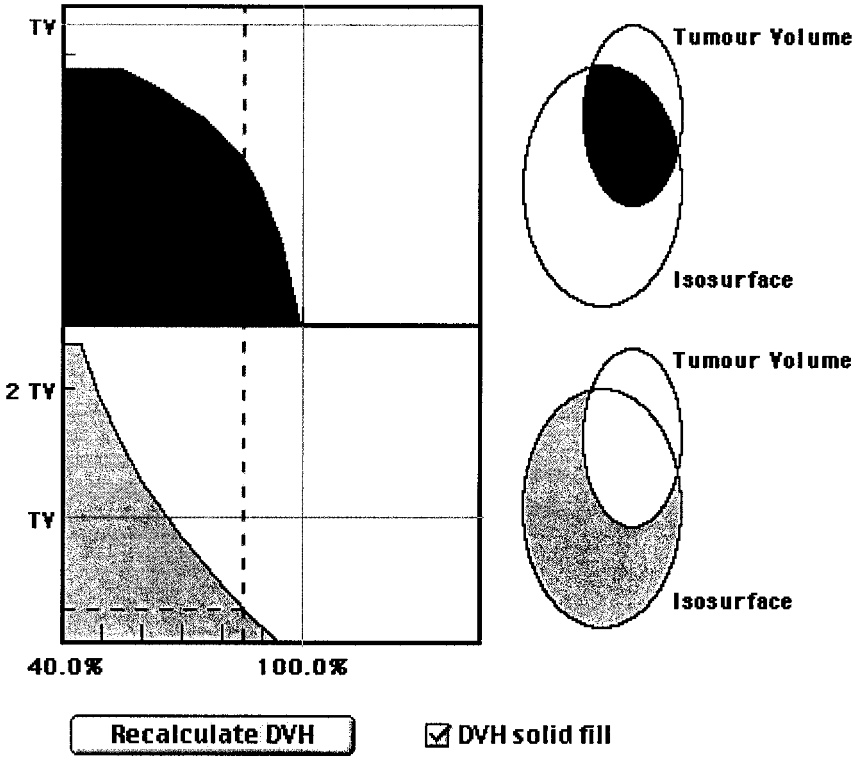

Figure 71. Cumulative dose volume histograms (target and surrounding healthy tissue) for the delivered treatment plan for patient 3. Only 57% of the target volume received a dose equal to or greater than the prescription dose at the 85% isodose surface. The volume of healthy tissue irradiated within the 85% isodose surface is 29% of the target volume.

Table 9. Isocentre positions and cone sizes for optimised and delivered treatment plans for patient 3.

Plan	Location (x,y,z) in mm	Cone size in cm
Optimised		
Isocentre 1	(73.7, 63.0, 111.7)	0.75
Isocentre 2	(77.2, 56.4, 111.4)	0.75
Isocentre 3	(81.5, 61.1, 111.4)	0.50
Delivered treatment		
Isocentre 1	(76.5, 57.3, 112.5)	1.25

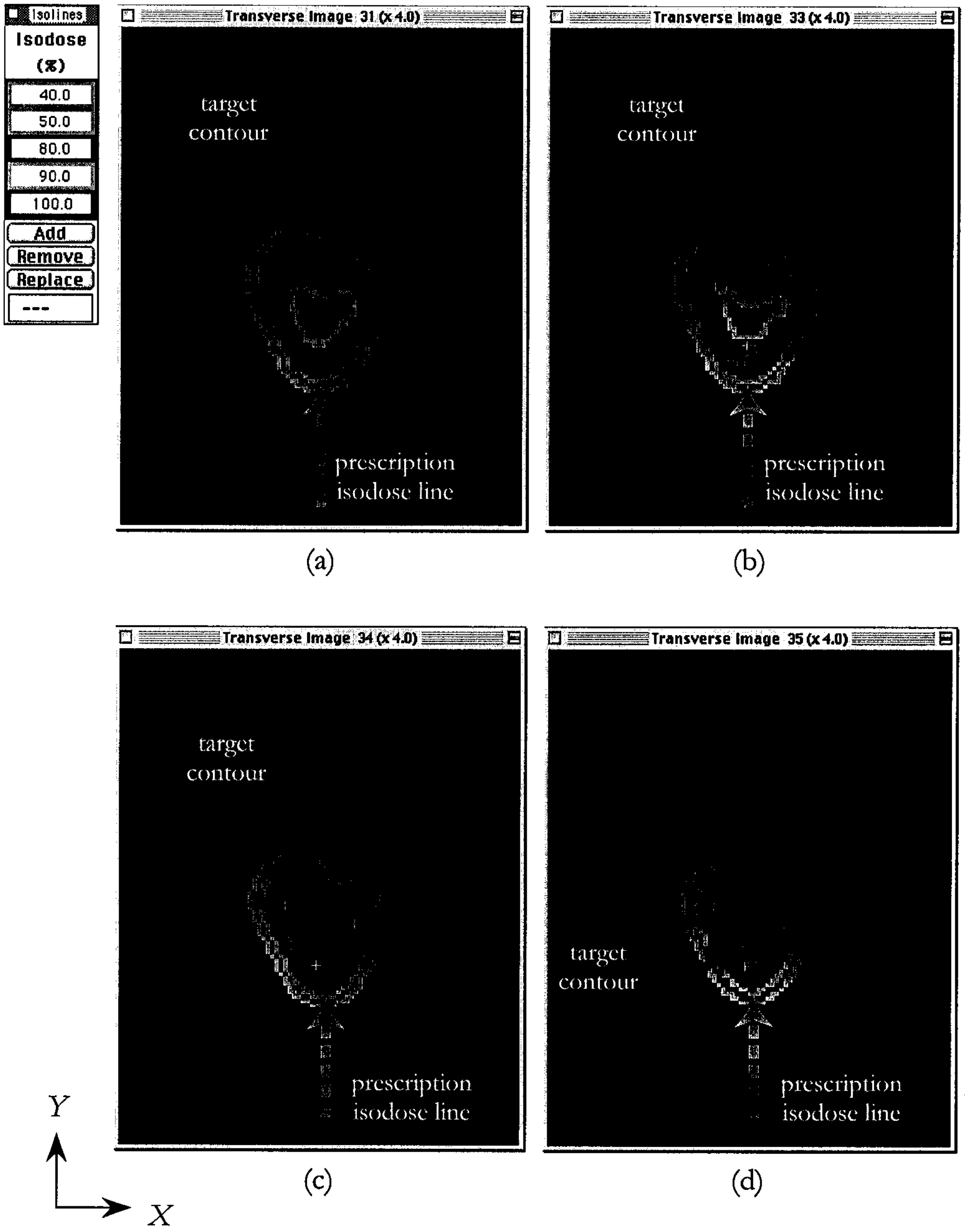

Figure 72. Comparison of isodose lines and reference target contours for the optimised treatment plan for patient 3. The target contour and prescription isodose line are shown by the full and dashed arrows respectively. The upper *Y* region of the target, which was excluded in the delivered treatment plan, is covered by the optimised plan.

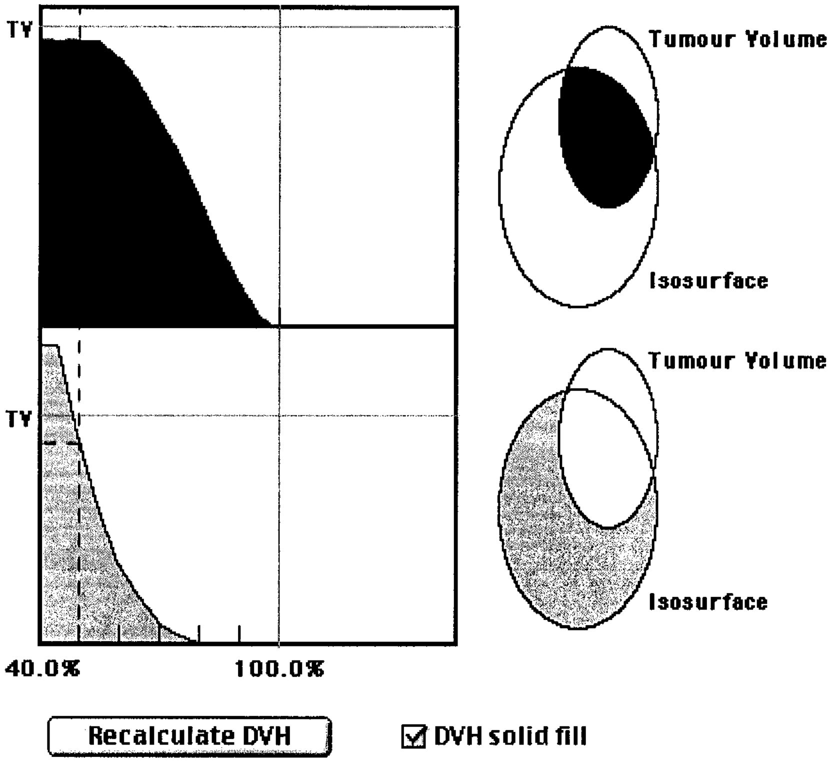

Figure 73. Cumulative dose volume histograms (target and surrounding healthy tissue) for the optimised treatment plan for patient 3. 98% of the target volume is within the 50% (prescription) isodose surface. The volume of healthy tissue irradiated within the 50% isodose surface is 91% of the target volume.

5.5 Summary

In this chapter, the dosimetric implications of including image fusion in the localisation and delineation process have been presented. By employing the reference target contours drawn with MRA, MR and SA images, the delivered treatment plan of the three patients, which included one isocentre, was found not to cover the majority of the target volume. The computed DVHs showed that 36%, 50% and 57%, of the target volume was covered for patient 1, 2 and 3 respectively. If the reference target contours had been provided prior to the treatment, modifications would have been made to the plan in order to increase the target coverage. This shows the limitations of localising and delineating the target without image fusion.

With the reference target contours provided, optimised treatment plans were determined for the three patients. For the first patient, due to the irregular shape of the target, eight isocentres were needed for the treatment plan to be within acceptable limits. For the second patient, four isocentres were employed to cover the target and to spare healthy tissue. For the third patient, three isocentres were needed in order to cover the majority of the target volume and to spare the surrounding healthy tissue. With the optimised plans, the computed DVHs showed a great improvement in target coverage and healthy tissue sparing. These results are in accordance with those obtained by by Kondziolka *et al.* [64] which state that 1) AVMs appear more spherical on SA images and 2) the number of isocentres required to increase dose conformity can increase to as many as ten isocentres.

Chapter 6

Conclusions

6.1 Summary

A multimodality image fusion and localisation system has been developed for radiosurgery treatments of arteriovenous malformations (AVM). Within this system, tools have been developed for:

I. Fusion of 3D datasets (MRA/CTA & MR/CT) in order to combine vascular and anatomical information.

II. Simulation of projections through the 3D datasets described in (I) above employing the projection geometry of the SA images. A comparison between the numerically simulated 2D images and the SA images, as well as the projection of the contours drawn on the MRA dataset onto the SA images, provide a visual check of potential errors that may be introduced during MRA localisation and definition of the AVM.

Since organ contours are drawn on the MRA images, simultaneously visualised on their MR/CT counterparts, and projected onto the SA images for visual feedback, the system allows users to incorporate both vascular and anatomical information in the three-dimensional target localisation and delineation process.

The developed tools have been validated. The 3D MRA/MR/CT localisation process was validated by comparing the results obtained with the developed system to those obtained with a clinically used in-house treatment planning software [76, 77]. This localisation process presented an average difference in distance between points of 0.7 ± 0.2 mm and of 0.7 ± 0.3 mm for the initial images and reformatted images respectively. This comparison was established with prominent anatomical features. Since the fiducial markers are user selected, the target locations are expected to differ slightly between the two systems. The accuracy of the SVD algorithm in the determination of the SA projection geometry was evaluated to be 0.02 mm on the localiser box face closest to the image plane where the error is the greatest. The uncertainty introduced by the user in the selection of the image fiducial markers was evaluated to be 0.3 mm on the SA localiser box face closest to the image plane. A phantom was designed and employed to validate the entire procedure.

Ray-tracing was performed through the MRA and the resulting images were compared to the SA images in Chapter 3. For the first patient, the images correlated well in the vicinity of the AVM as well as in the surrounding region of the AVM. However, a greater target volume was suggested by the ray-traced MRA images. For the second patient, the vessels in the vicinity of the AVM in the ray-traced images correlated well with those on the SA images. However, vessels in the region surrounding the AVM did not correlate well visually which can be due to a MR artefact or another image artefact. For the third patient, the AVM was not clearly visible on the ray-traced images. However, the vessels in the region surrounding the AVM of the ray-traced MRA images correlated well visually with those on the SA images.

The fourth chapter presented results indicating the utility of image fusion for target volume definition. Underestimation and overestimation of target volumes have been as large as 92.1% and 39.4% respectively. Not employing all modalities for the delineation process seems to result in considerable underestimation of target volumes. Differences in target location are considerable when all modalities are not employed for the target localisation and delineation process. For the first patient, the MRA images, which increased the target volume, were most useful for the delineation process. The SA images were misleading when the MRA images were not employed for the delineation process. The use of all imaging modalities within the interactive system was useful. Without it, considerable underestimation of the target volume would have been obtained. For the second patient, all modalities were useful for the definition of the target volume. The SA images guided the physician in the surrounding region of the lesion. The MRA images provided additional vascular information. For the third patient, the SA images were most useful since MR artefacts were present due the insertion of permanent clips in previous surgery, however, the MRA images did present additional information as to the shape and the size of the target. Due to the MR artefacts, the interactivity of the fusion system was useful for 3D delineation. As a result, the fusion system has a great impact on the coverage of the target volume and sparing of healthy tissue.

The dosimetric implications of image fusion for target localisation and delineation have been presented in Chapter 5. For all three patients, the position of the isocentre as well as the size of the cone for the delivered treatment were shown to be unacceptable for the reference target contours, which were drawn with MRA, MR and SA images. The plans did not cover the majority of the target. The computed DVHs showed that 36%, 50% and 57%, of the target volume was covered for patient 1, 2 and 3 respectively. Modifications would have been made to the plan in order to increase the target coverage if the target contours had been provided prior to the treatment, which shows the limitations of localising and delineating the target without image fusion. By employing the reference target contours, optimised treatment plans were determined for the three patients. Due to the irregular shape of the target of the first patient, eight isocentres were needed for the treatment plan to be within acceptable limits. For the second patient, four isocentres were employed to cover the target and to spare healthy tissue. For the third patient, three isocentres were needed in order to cover the majority of the target volume and to spare the surrounding healthy tissue. With the optimised plans, the computed DVHs showed a great improvement in target coverage, yet acceptable healthy tissue sparing.

6.2 Future work

A potential improvement to the system is to automate the fiducial marker selection for the SA, MR/CT images in order to increase the efficiency of the process. Another potential improvement is to incorporate an anatomical fusion tool in order to optimise anatomy matching between the 3D datasets.

A study including more patients that had previously undergone radiosurgery for AVMs would be useful in order to increase the statistics of the findings presented in this thesis. A further study on target volumes as well as on the dosimetric implications of the target volumes obtained with image fusion would be useful in the determination of the role of MRA for radiosurgery of AVMs.

A quantitative study on the correlation of the ray-traced MRA images and the SA images would quantify the relation between the datasets. Since SA images have phase information (arterial phase, venous phase) and MRA images do not, an anatomical comparison of the images might reveal extra information in the MRA images.

References

[1] G. Hademenos, Massoud, Tarik F., *The Physics of Cerebrovascular Diseases: Biophysical Mechanisms of Development, Diagnosis and Therapy*. New York: AIP Press, Springer-Verlag, 1998.

[2] A. Luessenhop, "Natural History of Cerebral Arteriovenous Malformations," in *Intracranial Arteriovenous Malformations, Current Neurosurgical Practise*, C. Wilson, Stein, BM., Ed. Baltimore: Williams and Wilkins, 1984, pp. 12-23.

[3] V. B. Graves and T. A. Duff, "Intracranial arteriovenous malformations. Current imaging and treatment," *Investigative Radiology*, vol. 25, pp. 952-960, 1990.

[4] B. E. Pollock, "Stereotactic radiosurgery for arteriovenous malformations," *Neurosurg Clin N Am*, vol. 10, pp. 281-290, 1999.

[5] R. C. Wallace and E. C. Bourekas, "Brain arteriovenous malformations," *Neuroimaging Clin N Am*, vol. 8, pp. 383-399, 1998.

[6] A. Nanda, "Controversies in neurosurgery: microsurgery versus radiosurgery for arteriovenous malformations--introduction," *Clin Neurosurg*, vol. 45, pp. 11-12, 1999.

[7] P. J. Porter, A. Y. Shin, A. S. Detsky, L. Lefaive, and M. C. Wallace, "Surgery versus stereotactic radiosurgery for small, operable cerebral arteriovenous malformations: a clinical and cost comparison," *Neurosurgery*, vol. 41, pp. 757-764; discussion 764-766, 1997.

[8] D. L. Barrow, "Controversies in neurosurgery: microsurgery versus radiosurgery for arteriovenous malformations--the case for microsurgery," *Clin Neurosurg*, vol. 45, pp. 13-17, 1999.

[9] J. P. Deveikis, "Endovascular therapy of intracranial arteriovenous malformations. Materials and techniques," *Neuroimaging Clin N Am*, vol. 8, pp. 401-424, 1998.

[10] D. Bourque, "Static conformal fields in stereotactic radiosurgery," in *Medical Physics Unit.* Montreal: McGill, 1997, pp. 140.

[11] E. B. Podgorsak, A. Olivier, M. Pla, P. Y. Lefebvre, and J. Hazel, "Dynamic stereotactic radiosurgery," *International Journal of Radiation Oncology, Biology, Physics*, vol. 14, pp. 115-126, 1988.

[12] P. P. Kesava and P. A. Turski, "MR angiography of vascular malformations," *Neuroimaging Clinics of North America*, vol. 8, pp. 349-370, 1998.

[13] W. A. Friedman, "Radiosurgery versus surgery for arteriovenous malformations: the case for radiosurgery," *Clin Neurosurg*, vol. 45, pp. 18-20, 1999.

[14] T. L. Ellis, W. A. Friedman, F. J. Bova, P. S. Kubilis, and J. M. Buatti, "Analysis of treatment failure after radiosurgery for arteriovenous malformations," *J Neurosurg*, vol. 89, pp. 104-110, 1998.

[15] P. Gallina, L. Merienne, J. F. Meder, M. Schlienger, D. Lefkopoulos, and J. J. Merland, "Failure in radiosurgery treatment of cerebral arteriovenous malformations," *Neurosurgery*, vol. 42, pp. 996-1002; discussion 1002-1004, 1998.

[16] W. Y. Guo, B. Nordell, B. Karlsson, M. Soderman, M. Lindqvist, K. Ericson, A. Franck, I. Lax, and C. Lindquist, "Target delineation in radiosurgery for cerebral arteriovenous malformations. Assessment of the value of stereotaxic MR imaging and MR angiography," *Acta Radiol*, vol. 34, pp. 457-463, 1993.

[17] F. J. Bova and W. A. Friedman, "Stereotactic angiography: an inadequate database for radiosurgery?," *International Journal of Radiation Oncology, Biology, Physics*, vol. 20, pp. 891-895, 1991.

[18] G. Bednarz, B. Downes, M. Werner-Wasik, and R. H. Rosenwasser, "Combining stereotactic angiography and 3D time-of-flight magnetic resonance angiography in

treatment planning for arteriovenous malformation radiosurgery," *International Journal of Radiation Oncology, Biology, Physics*, vol. 46, pp. 1149-1154, 2000.

[19] J. Klisch, R. Strecker, J. Hennig, and M. Schumacher, "Time-resolved projection MRA: clinical application in intracranial vascular malformations," *Neuroradiology*, vol. 42, pp. 104-107, 2000.

[20] K. Takano, H. Utsunomiya, H. Ono, M. Okazaki, and A. Tanaka, "Dynamic contrast-enhanced subtraction MR angiography in intracranial vascular abnormalities," *European Radiology*, vol. 9, pp. 1909-1912, 1999.

[21] J. C. Steffens, J. Link, and M. Heller, "Contrast-enhanced magnetic resonance angiography of the cervical arteries. A review," *Invest Radiol*, vol. 33, pp. 573-577, 1998.

[22] G. Marchal, H. Bosmans, L. Van Fraeyenhoven, G. Wilms, P. Van Hecke, C. Plets, and A. L. Baert, "Intracranial vascular lesions: optimization and clinical evaluation of three-dimensional time-of-flight MR angiography," *Radiology*, vol. 175, pp. 443-448, 1990.

[23] Y. Suzuki and K. Matsumoto, "[Detection of the venous system of the skull base using three-dimensional CT angiography (3D-CTA): utility of the subtemporal approach]," *No Shinkei Geka - Neurological Surgery*, vol. 28, pp. 17-22, 2000.

[24] G. B. Anderson, D. E. Steinke, K. C. Petruk, R. Ashforth, and J. M. Findlay, "Computed tomographic angiography versus digital subtraction angiography for the diagnosis and early treatment of ruptured intracranial aneurysms," *Neurosurgery*, vol. 45, pp. 1315-1320; discussion 1320-1322, 1999.

[25] T. Okuyama, K. Saito, A. Hirano, A. Takahashi, T. Inagaki, and S. Inamura, "[Improvement of MRA and 3D-CTA does away with the need for cerebral angiography in many cerebral aneurysm operations]," *No Shinkei Geka - Neurological Surgery*, vol. 26, pp. 607-612, 1998.

[26] H. Tanaka, Y. Numaguchi, S. Konno, D. A. Shrier, D. K. Shibata, and U. Patel, "Initial experience with helical CT and 3D reconstruction in therapeutic planning of cerebral AVMs: comparison with 3D time-of-flight MRA and digital subtraction angiography," *Journal of Computer Assisted Tomography*, vol. 21, pp. 811-817, 1997.

[27] R. P. Levy, R. W. Schulte, K. A. Frankel, G. K. Steinberg, M. P. Marks, B. Lane, L. H. Heilbronn, H. J. Meinass, R. A. Galindo, J. D. Slater, and J. M. Slater, "Computed tomography slice-by-slice target-volume delineation for stereotactic proton irradiation of large intracranial arteriovenous malformations: an iterative approach using angiography, computed tomography, and magnetic resonance imaging," *Int J Radiat Oncol Biol Phys*, vol. 35, pp. 555-564, 1996.

[28] V. S. Khoo, E. J. Adams, F. Saran, J. L. Bedford, J. R. Perks, A. P. Warrington, and M. Brada, "A Comparison of clinical target volumes determined by CT and MRI for the radiotherapy planning of base of skull meningiomas," *International Journal of Radiation Oncology, Biology, Physics*, vol. 46, pp. 1309-1317, 2000.

[29] R. J. Amdur, D. Gladstone, K. A. Leopold, and R. D. Harris, "Prostate seed implant quality assessment using MR and CT image fusion," *International Journal of Radiation Oncology, Biology, Physics*, vol. 43, pp. 67-72, 1999.

[30] J. P. Lattanzi, D. A. Fein, S. W. McNeeley, A. H. Shaer, B. Movsas, and G. E. Hanks, "Computed tomography-magnetic resonance image fusion: a clinical evaluation of an innovative approach for improved tumor localization in primary central nervous system lesions," *Radiation Oncology Investigations*, vol. 5, pp. 195-205, 1997.

[31] K. Kagawa, W. R. Lee, T. E. Schultheiss, M. A. Hunt, A. H. Shaer, and G. E. Hanks, "Initial clinical assessment of CT-MRI image fusion software in localization of the prostate for 3D conformal radiation therapy," *International Journal of Radiation Oncology, Biology, Physics*, vol. 38, pp. 319-325, 1997.

[32] H. Y. Lau, K. Kagawa, W. R. Lee, M. A. Hunt, A. H. Shaer, and G. E. Hanks, "Short communication: CT-MRI image fusion for 3D conformal prostate radiotherapy: use in

patients with altered pelvic anatomy," *British Journal of Radiology*, vol. 69, pp. 1165-1170, 1996.

[33] E. Podgorsak, Podgorsak, MB., "Stereotactic Irradiation," in *The Modern Technology of Radiation Oncology*, J. V. Dyk, Ed. Madison: Medical Physics Publishing, 1999, pp. 1072.

[34] M. C. Schell, Bova, F.J., Larson, D.A., Leavitt, D.D., Lutz, W.R., Podgorsak, E.B., Wu, A., "Stereotactic Radiosurgery," , Woodbury AAPM Report No. 54, June 1995.

[35] D. R. Blatt, W. A. Friedman, and F. J. Bova, "Modifications based on computed tomographic imaging in planning the radiosurgical treatment of arteriovenous malformations," *Neurosurgery*, vol. 33, pp. 588-595; discussion 595-596, 1993.

[36] J. I. Fabrikant, R. P. Levy, G. K. Steinberg, M. H. Phillips, K. A. Frankel, J. T. Lyman, M. P. Marks, and G. D. Silverberg, "Charged-particle radiosurgery for intracranial vascular malformations," *Neurosurg Clin N Am*, vol. 3, pp. 99-139, 1992.

[37] A. Macovski, *Medical Imaging Systems.* Englewood Cliffs: Prentice-Hall, 1983.

[38] J. T. Bushberg, Seibert, J. A., Leidholdt, E. M., Boone, J. M., *The Essential Physics of Medical Imaging.* Baltimore: Williams and Wilkins, 1994.

[39] M. O. Leach, "Spatially Localised Nuclear Magnetic Resonance," in *The Physics of Medical Imaging, Medical Science*, S. Webb, Ed. New York: IOP, 1988, pp. 633.

[40] V. S. Khoo, D. P. Dearnaley, D. J. Finnigan, A. Padhani, S. F. Tanner, and M. O. Leach, "Magnetic resonance imaging (MRI): considerations and applications in radiotherapy treatment planning," *Radiother Oncol*, vol. 42, pp. 1-15, 1997.

[41] G. Bednarz, M. B. Downes, B. W. Corn, W. J. Curran, and H. W. Goldman, "Evaluation of the spatial accuracy of magnetic resonance imaging-based stereotactic target localization for gamma knife radiosurgery of functional disorders," *Neurosurgery*, vol. 45, pp. 1156-1161; discussion 1161-1163, 1999.

[42] C. Maurer, G. B. Aboutanos, B. M. Dawant, S. Gadamsetty, R. A. Margolin, R. J. Maciunas, and J. M. Fitzpatrick, "Effect of geometrical distortion correction in MR on image registration accuracy," *J Comput Assist Tomogr*, vol. 20, pp. 666-679, 1996.

[43] D. Dean, J. Kamath, J. L. Duerk, and E. Ganz, "Validation of object-induced MR distortion correction for frameless stereotactic neurosurgery," *IEEE Trans Med Imaging*, vol. 17, pp. 810-816, 1998.

[44] L. Walton, A. Hampshire, D. M. Forster, and A. A. Kemeny, "A phantom study to assess the accuracy of stereotactic localization, using T1-weighted magnetic resonance imaging with the Leksell stereotactic system," *Neurosurgery*, vol. 38, pp. 170-176; discussion 176-178, 1996.

[45] J. Michiels, H. Bosmans, P. Pelgrims, D. Vandermeulen, J. Gybels, G. Marchal, and P. Suetens, "On the problem of geometric distortion in magnetic resonance images for stereotactic neurosurgery," *Magn Reson Imaging*, vol. 12, pp. 749-765, 1994.

[46] C. J. Bakker, M. A. Moerland, R. Bhagwandien, and R. Beersma, "Analysis of machine-dependent and object-induced geometric distortion in 2DFT MR imaging," *Magn Reson Imaging*, vol. 10, pp. 597-608, 1992.

[47] R. J. Maciunas, J. M. Fitzpatrick, S. Gadamsetty, and C. R. Maurer, Jr., "A universal method for geometric correction of magnetic resonance images for stereotactic neurosurgery," *Stereotact Funct Neurosurg*, vol. 66, pp. 137-140, 1996.

[48] D. S. Cohen, J. H. Lustgarten, E. Miller, A. G. Khandji, and R. R. Goodman, "Effects of coregistration of MR to CT images on MR stereotactic accuracy," *J Neurosurg*, vol. 82, pp. 772-779, 1995.

[49] B. K. Rutt, "Vascular System MR Imaging," presented at the 1992 AAPM Summer School on The Physics of MRI, Banff, Alberta, Canada, 1992.

[50] M. J. Graves, "Magnetic resonance angiography," *Br J Radiol*, vol. 70, pp. 6-28, 1997.

[51] P. A. Tercier, P. Coucke, H. Fankhauser, R. O. Mirimanoff, A. Uske, and J. F. Valley, "Transfer of information between angiographic films and CT images: a technique to control the drawing of target volumes," *Radiother Oncol*, vol. 45, pp. 263-269, 1997.

[52] T. S. Chung, J. Y. Joo, S. K. Lee, D. Chien, and G. Laub, "Evaluation of cerebral aneurysms with high-resolution MR angiography using a section-interpolation technique: correlation with digital subtraction angiography," *Ajnr: American Journal of Neuroradiology*, vol. 20, pp. 229-235, 1999.

[53] D. M. Cash, M. G. Palmisano, and R. L. Galloway, "Surgically appropriate MIPs of tomographic angiograms," *Proceedings of the First Joint BMES/EMBS Conference*, vol. 2, pp. 1153, 1999.

[54] M. G. Palmisano, R. L. Galloway, and R. J. Maciunas, "Modified maximum intensity projections for surgical guidance," *Proceedings of SPIE the International Society for Optical Engineering*, vol. 3031, pp. 643-650, 1997.

[55] C. Labisch, T. Aalders, V. Seifert, and F. E. Zanella, "3D-visualisation of intracranial vascular malformations by CT-angiography (CT-A) for neurosurgical operation planning in comparison to conventional DSA," *CAR '96 Computer Assisted Radiology. Proceedings of the International Symposium on Computer and Communication Systems for Image Guided Diagnosis and Therapy. Elsevier.*, 1996.

[56] E. P. Wilkinson, R. Shahidi, B. Wang, D. P. Martin, J. R. Adler, Jr., and G. K. Steinberg, "Remote-rendered 3D CT angiography (3DCTA) as an intraoperative aid in cerebrovascular neurosurgery," *Computer Aided Surgery*, vol. 4, pp. 256-263, 1999.

[57] M. A. Melgar, L. Zamorano, Z. Jiang, M. Guthikonda, V. Gordon, and F. G. Diaz, "Three-dimensional magnetic resonance angiography in the planning of aneurysm surgery," *Computer Aided Surgery*, vol. 2, pp. 11-23, 1997.

[58] C. J. Henri, D. L. Collins, and T. M. Peters, "Multimodality image integration for stereotactic surgical planning," *Medical Physics*, vol. 18, pp. 167-177, 1991.

[59] M. H. Phillips, K. A. Frankel, J. T. Lyman, J. I. Fabrikant, and R. P. Levy, "Heavy charged-particle stereotactic radiosurgery: cerebral angiography and CT in the treatment of intracranial vascular malformations," *International Journal of Radiation Oncology, Biology, Physics*, vol. 17, pp. 419-426, 1989.

[60] M. H. Phillips, M. Kessler, F. Y. Chuang, K. A. Frankel, J. T. Lyman, J. I. Fabrikant, and R. P. Levy, "Image correlation of MRI and CT in treatment planning for radiosurgery of intracranial vascular malformations," *International Journal of Radiation Oncology, Biology, Physics*, vol. 20, pp. 881-889, 1991.

[61] D. Petereit, M. Mehta, P. Turski, A. Levin, C. Strother, C. Mistretta, R. Mackie, M. Gehring, S. Kubsad, and T. Kinsella, "Treatment of arteriovenous malformations with stereotactic radiosurgery employing both magnetic resonance angiography and standard angiography as a database," *International Journal of Radiation Oncology, Biology, Physics*, vol. 25, pp. 309-313, 1993.

[62] H. H. Ehricke, L. R. Schad, G. Gademann, B. Wowra, R. Engenhart, and W. J. Lorenz, "Use of MR angiography for stereotactic planning," *J Comput Assist Tomogr*, vol. 16, pp. 35-40., 1992.

[63] D. J. Warren, N. Hoggard, L. Walton, M. W. Radatz, A. A. Kemeny, D. M. Forster, I. D. Wilkinson, and P. D. Griffiths, "Cerebral arteriovenous malformations: comparison of novel magnetic resonance angiographic techniques and conventional catheter angiography," *Neurosurgery*, vol. 48, pp. 973-82; discussion 982-3., 2001.

[64] D. Kondziolka, L. D. Lunsford, E. Kanal, and L. Talagala, "Stereotactic magnetic resonance angiography for targeting in arteriovenous malformation radiosurgery," *Neurosurgery*, vol. 35, pp. 585-90; discussion 590-1., 1994.

[65] S. K. Mukherji, R. G. Quisling, P. S. Kubilis, J. P. Finn, and W. A. Friedman, "Intracranial arteriovenous malformations: quantitative analysis of magnitude contrast MR angiography versus gradient-echo MR imaging versus conventional angiography," *Radiology*, vol. 196, pp. 187-93., 1995.

[66] M. Essig, R. Engenhart, M. V. Knopp, M. Bock, J. Scharf, J. Debus, F. Wenz, H. Hawighorst, L. R. Schad, and G. van Kaick, "Cerebral arteriovenous malformations: improved nidus demarcation by means of dynamic tagging MR-angiography," *Magn Reson Imaging*, vol. 14, pp. 227-33, 1996.

[67] M. J. Dobson, R. W. Hartley, R. Ashleigh, Y. Watson, and J. M. Hawnaur, "MR angiography and MR imaging of symptomatic vascular malformations," *Clin Radiol*, vol. 52, pp. 595-602., 1997.

[68] R. I. Farb, C. McGregor, J. K. Kim, M. Laliberte, J. A. Derbyshire, R. A. Willinsky, P. W. Cooper, D. G. Westman, G. Cheung, M. L. Schwartz, J. A. Stainsby, and G. A. Wright, "Intracranial arteriovenous malformations: real-time auto-triggered elliptic centric-ordered 3D gadolinium-enhanced MR angiography--initial assessment," *Radiology*, vol. 220, pp. 244-51., 2001.

[69] Y. Bercier, Patrocinio, H., Belanger, P., Hristov, D., "Multimodality Image Fusion and Localisation Environment for Radiosurgery Treatments of Large AVMs," presented at The XIIIth International Conference on The Use of Computers in Radiation Therapy, Heidelberg, Germany, 2000.

[70] Y. Bercier, Patrocinio, H., Belanger, P., Hristov, H., "Multimodality image fusion for radiosurgery localisation of large AVMs," presented at The World Congress on Medical Physics and Boimedical Engineering, Chicago, Illinois, 2000.

[71] Y. Bercier, Hristov, D., "Correlation of DSA and MRA projection images for radiosurgery localization of arteriovenous malformations," presented at 19th annual European Society for Therapeutic Radiology & Oncology, Istanbul, Turkey, 2000.

[72] J. Zhang, M. F. Levesque, C. L. Wilson, R. M. Harper, J. Engel, Jr., R. Lufkin, and E. J. Behnke, "Multimodality imaging of brain structures for stereotactic surgery," *Radiology*, vol. 175, pp. 435-441, 1990.

[73] W. H. Press, Teukolsky, S.A., Vetterling, W.T., Flannery, B.P., *Numerical Recipes in C: The Art of Scientific Computing*, Second ed. Cambridge: Press Syndicate of the University of Cambridge, 1992.

[74] R. L. Siddon, "Fast calculation of the exact radiological path for a three-dimensional CT array," *Med Phys*, vol. 12, pp. 252-255, 1985.

[75] G. W. Sherouse, K. Novins, and E. L. Chaney, "Computation of digitally reconstructed radiographs for use in radiotherapy treatment design," *Int J Radiat Oncol Biol Phys*, vol. 18, pp. 651-658, 1990.

[76] G. B. Pike, E. B. Podgorsak, T. M. Peters, C. Pla, and A. Olivier, "Three-dimensional isodose distributions in stereotactic radiosurgery," *Stereotact Funct Neurosurg*, vol. 55, pp. 519-524, 1990.

[77] G. B. Pike, E. B. Podgorsak, T. M. Peters, C. Pla, A. Olivier, and L. Souhami, "Dose distributions in radiosurgery," *Med Phys*, vol. 17, pp. 296-304, 1990.

[78] A. J. Luessenhop, "Cranial Arteriovenous Malformations," in *Operative Neurosurgical Techniques: Indications, Methods and Results*, vol. II, W. H. S. H.H. Schmidek, Ed. Philadelphia: W. B. Saunders, 1988.

Bibliography

Page numbers are indicated in brackets at the end of each reference.

R. J. Amdur, D. Gladstone, K. A. Leopold, and R. D. Harris, "Prostate seed implant quality assessment using MR and CT image fusion," *International Journal of Radiation Oncology, Biology, Physics*, vol. 43, pp. 67-72, 1999. [8]

G. B. Anderson, D. E. Steinke, K. C. Petruk, R. Ashforth, and J. M. Findlay, "Computed tomographic angiography versus digital subtraction angiography for the diagnosis and early treatment of ruptured intracranial aneurysms," *Neurosurgery*, vol. 45, pp. 1315-1320; discussion 1320-1322, 1999. [7, 8]

C. J. Bakker, M. A. Moerland, R. Bhagwandien, and R. Beersma, "Analysis of machine-dependent and object-induced geometric distortion in 2DFT MR imaging," *Magn Reson Imaging*, vol. 10, pp. 597-608, 1992. [14]

D. L. Barrow, "Controversies in neurosurgery: microsurgery versus radiosurgery for arteriovenous malformations--the case for microsurgery," *Clin Neurosurg*, vol. 45, pp. 13-17, 1999. [5]

G. Bednarz, B. Downes, M. Werner-Wasik, and R. H. Rosenwasser, "Combining stereotactic angiography and 3D time-of-flight magnetic resonance angiography in treatment planning for arteriovenous malformation radiosurgery," *International Journal of Radiation Oncology, Biology, Physics*, vol. 46, pp. 1149-1154, 2000. [7, 8, 20, 22-24, 72, 81, 95]

G. Bednarz, M. B. Downes, B. W. Corn, W. J. Curran, and H. W. Goldman, "Evaluation of the spatial accuracy of magnetic resonance imaging-based stereotactic target localization for gamma knife radiosurgery of functional disorders," *Neurosurgery*, vol. 45, pp. 1156-1161; discussion 1161-1163, 1999. [14]

Y. Bercier, Hristov, D., "Correlation of DSA and MRA projection images for radiosurgery localization of arteriovenous malformations," presented at 19th annual European Society for Therapeutic Radiology & Oncology, Istanbul, Turkey, 2000. [25]

Y. Bercier, Patrocinio, H., Belanger, P., Hristov, D., "Multimodality Image Fusion and Localisation Environment for Radiosurgery Treatments of Large AVMs," presented at The XIIIth International Conference on The Use of Computers in Radiation Therapy, Heidelberg, Germany, 2000. [25]

Y. Bercier, Patrocinio, H., Belanger, P., Hristov, H., "Multimodality image fusion for radiosurgery localisation of large AVMs," presented at The World Congress on Medical Physics and Boimedical Engineering, Chicago, Illinois, 2000. [25]

D. R. Blatt, W. A. Friedman, and F. J. Bova, "Modifications based on computed tomographic imaging in planning the radiosurgical treatment of arteriovenous malformations," *Neurosurgery*, vol. 33, pp. 588-595; discussion 595-596, 1993. [11]

D. Bourque, "Static conformal fields in stereotactic radiosurgery," in *Medical Physics Unit.* Montreal: McGill, 1997, pp. 140. [7]

F. J. Bova and W. A. Friedman, "Stereotactic angiography: an inadequate database for radiosurgery?," *International Journal of Radiation Oncology, Biology, Physics*, vol. 20, pp. 891-895, 1991. [7, 11, 12]

J. T. Bushberg, Seibert, J. A., Leidholdt, E. M., Boone, J. M., *The Essential Physics of Medical Imaging.* Baltimore: Williams and Wilkins, 1994. [13, 14]

D. M. Cash, M. G. Palmisano, and R. L. Galloway, "Surgically appropriate MIPs of tomographic angiograms," *Proceedings of the First Joint BMES/EMBS Conference*, vol. 2, pp. 1153, 1999. [20]

D. S. Cohen, J. H. Lustgarten, E. Miller, A. G. Khandji, and R. R. Goodman, "Effects of coregistration of MR to CT images on MR stereotactic accuracy," *J Neurosurg*, vol. 82, pp. 772-779, 1995. [14]

T. S. Chung, J. Y. Joo, S. K. Lee, D. Chien, and G. Laub, "Evaluation of cerebral aneurysms with high-resolution MR angiography using a section-interpolation technique: correlation with digital subtraction angiography," *Ajnr: American Journal of Neuroradiology*, vol. 20, pp. 229-235, 1999. [20]

D. Dean, J. Kamath, J. L. Duerk, and E. Ganz, "Validation of object-induced MR distortion correction for frameless stereotactic neurosurgery," *IEEE Trans Med Imaging*, vol. 17, pp. 810-816, 1998. [14]

J. P. Deveikis, "Endovascular therapy of intracranial arteriovenous malformations. Materials and techniques," *Neuroimaging Clin N Am*, vol. 8, pp. 401-424, 1998. [5]

M. J. Dobson, R. W. Hartley, R. Ashleigh, Y. Watson, and J. M. Hawnaur, "MR angiography and MR imaging of symptomatic vascular malformations," *Clin Radiol*, vol. 52, pp. 595-602., 1997. [20, 21, 23]

H. H. Ehricke, L. R. Schad, G. Gademann, B. Wowra, R. Engenhart, and W. J. Lorenz, "Use of MR angiography for stereotactic planning," *J Comput Assist Tomogr*, vol. 16, pp. 35-40., 1992. [20, 23, 24]

T. L. Ellis, W. A. Friedman, F. J. Bova, P. S. Kubilis, and J. M. Buatti, "Analysis of treatment failure after radiosurgery for arteriovenous malformations," *J Neurosurg*, vol. 89, pp. 104-110, 1998. [7]

M. Essig, R. Engenhart, M. V. Knopp, M. Bock, J. Scharf, J. Debus, F. Wenz, H. Hawighorst, L. R. Schad, and G. van Kaick, "Cerebral arteriovenous malformations: improved nidus demarcation by means of dynamic tagging MR-angiography," *Magn Reson Imaging*, vol. 14, pp. 227-33, 1996. [20, 21, 23]

J. I. Fabrikant, R. P. Levy, G. K. Steinberg, M. H. Phillips, K. A. Frankel, J. T. Lyman, M. P. Marks, and G. D. Silverberg, "Charged-particle radiosurgery for intracranial vascular malformations," *Neurosurg Clin N Am*, vol. 3, pp. 99-139, 1992. [11]

R. I. Farb, C. McGregor, J. K. Kim, M. Laliberte, J. A. Derbyshire, R. A. Willinsky, P. W. Cooper, D. G. Westman, G. Cheung, M. L. Schwartz, J. A. Stainsby, and G. A. Wright, "Intracranial arteriovenous malformations: real-time auto-triggered elliptic centric-ordered 3D gadolinium-enhanced MR angiography--initial assessment," *Radiology*, vol. 220, pp. 244-51., 2001. [20, 23]

W. A. Friedman, "Radiosurgery versus surgery for arteriovenous malformations: the case for radiosurgery," *Clin Neurosurg*, vol. 45, pp. 18-20, 1999. [7]

P. Gallina, L. Merienne, J. F. Meder, M. Schlienger, D. Lefkopoulos, and J. J. Merland, "Failure in radiosurgery treatment of cerebral arteriovenous malformations," *Neurosurgery*, vol. 42, pp. 996-1002; discussion 1002-1004, 1998. [7]

M. J. Graves, "Magnetic resonance angiography," *Br J Radiol*, vol. 70, pp. 6-28, 1997. [15, 16]

V. B. Graves and T. A. Duff, "Intracranial arteriovenous malformations. Current imaging and treatment," *Investigative Radiology*, vol. 25, pp. 952-960, 1990. [2, 3, 6, 8, 10, 14]

W. Y. Guo, B. Nordell, B. Karlsson, M. Soderman, M. Lindqvist, K. Ericson, A. Franck, I. Lax, and C. Lindquist, "Target delineation in radiosurgery for cerebral arteriovenous malformations. Assessment of the value of stereotaxic MR imaging and MR angiography," *Acta Radiol*, vol. 34, pp. 457-463, 1993. [7, 11, 15, 16]

G. Hademenos, Massoud, Tarik F., *The Physics of Cerebrovascular Diseases: Biophysical Mechanisms of Development, Diagnosis and Therapy*. New York: AIP Press, Springer-Verlag, 1998. [2, 3, 5, 6, 7]

C. J. Henri, D. L. Collins, and T. M. Peters, "Multimodality image integration for stereotactic surgical planning," *Medical Physics*, vol. 18, pp. 167-177, 1991. [20, 29, 37, 38, 71]

K. Kagawa, W. R. Lee, T. E. Schultheiss, M. A. Hunt, A. H. Shaer, and G. E. Hanks, "Initial clinical assessment of CT-MRI image fusion software in localization of the prostate for 3D conformal radiation therapy," *International Journal of Radiation Oncology, Biology, Physics*, vol. 38, pp. 319-325, 1997. [8]

P. P. Kesava and P. A. Turski, "MR angiography of vascular malformations," *Neuroimaging Clinics of North America*, vol. 8, pp. 349-370, 1998. [7, 8, 11, 15, 16]

V. S. Khoo, D. P. Dearnaley, D. J. Finnigan, A. Padhani, S. F. Tanner, and M. O. Leach, "Magnetic resonance imaging (MRI): considerations and applications in radiotherapy treatment planning," *Radiother Oncol*, vol. 42, pp. 1-15, 1997. [14]

V. S. Khoo, E. J. Adams, F. Saran, J. L. Bedford, J. R. Perks, A. P. Warrington, and M. Brada, "A Comparison of clinical target volumes determined by CT and MRI for the radiotherapy planning of base of skull meningiomas," *International Journal of Radiation Oncology, Biology, Physics*, vol. 46, pp. 1309-1317, 2000. [8]

J. Klisch, R. Strecker, J. Hennig, and M. Schumacher, "Time-resolved projection MRA: clinical application in intracranial vascular malformations," *Neuroradiology*, vol. 42, pp. 104-107, 2000. [7, 20]

D. Kondziolka, L. D. Lunsford, E. Kanal, and L. Talagala, "Stereotactic magnetic resonance angiography for targeting in arteriovenous malformation radiosurgery," *Neurosurgery*, vol. 35, pp. 585-90; discussion 590-1., 1994. [20, 23, 98, 100, 103, 107, 108, 113]

C. Labisch, T. Aalders, V. Seifert, and F. E. Zanella, "3D-visualisation of intracranial vascular malformations by CT-angiography (CT-A) for neurosurgical operation planning in comparison to conventional DSA," *CAR '96 Computer Assisted Radiology. Proceedings of the International Symposium on Computer and Communication Systems for Image Guided Diagnosis and Therapy. Elsevier.*, 1996. [20]

J. P. Lattanzi, D. A. Fein, S. W. McNeeley, A. H. Shaer, B. Movsas, and G. E. Hanks, "Computed tomography-magnetic resonance image fusion: a clinical evaluation of an innovative approach for improved tumor localization in primary central nervous system lesions," *Radiation Oncology Investigations*, vol. 5, pp. 195-205, 1997. [8]

H. Y. Lau, K. Kagawa, W. R. Lee, M. A. Hunt, A. H. Shaer, and G. E. Hanks, "Short communication: CT-MRI image fusion for 3D conformal prostate radiotherapy: use in patients with altered pelvic anatomy," *British Journal of Radiology*, vol. 69, pp. 1165-1170, 1996. [8]

M. O. Leach, "Spatially Localised Nuclear Magnetic Resonance," in *The Physics of Medical Imaging, Medical Science*, S. Webb, Ed. New York: IOP, 1988, pp. 633. [14, 15]

R. P. Levy, R. W. Schulte, K. A. Frankel, G. K. Steinberg, M. P. Marks, B. Lane, L. H. Heilbronn, H. J. Meinass, R. A. Galindo, J. D. Slater, and J. M. Slater, "Computed tomography slice-by-slice target-volume delineation for stereotactic proton irradiation of large intracranial arteriovenous malformations: an iterative approach using angiography, computed tomography, and magnetic resonance imaging," *Int J Radiat Oncol Biol Phys*, vol. 35, pp. 555-564, 1996. [7, 10, 11]

A. J. Luessenhop, "Cranial Arteriovenous Malformations," in *Operative Neurosurgical Techniques: Indications, Methods and Results*, vol. II, W. H. S. H.H. Schmidek, Ed. Philadelphia: W. B. Saunders, 1988. [61]

A. Luessenhop, "Natural History of Cerebral Arteriovenous Malformations," in *Intracranial Arteriovenous Malformations, Current Neurosurgical Practise*, C. Wilson, Stein, BM., Ed. Baltimore: Williams and Wilkins, 1984, pp. 12-23. [2, 4, 5, 6]

R. J. Maciunas, J. M. Fitzpatrick, S. Gadamsetty, and C. R. Maurer, Jr., "A universal method for geometric correction of magnetic resonance images for stereotactic neurosurgery," *Stereotact Funct Neurosurg*, vol. 66, pp. 137-140, 1996. [14]

A. Macovski, *Medical Imaging Systems*. Englewood Cliffs: Prentice-Hall, 1983. [13]

G. Marchal, H. Bosmans, L. Van Fraeyenhoven, G. Wilms, P. Van Hecke, C. Plets, and A. L. Baert, "Intracranial vascular lesions: optimization and clinical evaluation of three-dimensional time-of-flight MR angiography," *Radiology*, vol. 175, pp. 443-448, 1990. [7, 8]

C. Maurer, G. B. Aboutanos, B. M. Dawant, S. Gadamsetty, R. A. Margolin, R. J. Maciunas, and J. M. Fitzpatrick, "Effect of geometrical distortion correction in MR on image registration accuracy," *J Comput Assist Tomogr*, vol. 20, pp. 666-679, 1996. [14]

M. A. Melgar, L. Zamorano, Z. Jiang, M. Guthikonda, V. Gordon, and F. G. Diaz, "Three-dimensional magnetic resonance angiography in the planning of aneurysm surgery," *Computer Aided Surgery*, vol. 2, pp. 11-23, 1997. [20]

J. Michiels, H. Bosmans, P. Pelgrims, D. Vandermeulen, J. Gybels, G. Marchal, and P. Suetens, "On the problem of geometric distortion in magnetic resonance images for stereotactic neurosurgery," *Magn Reson Imaging*, vol. 12, pp. 749-765, 1994. [14]

S. K. Mukherji, R. G. Quisling, P. S. Kubilis, J. P. Finn, and W. A. Friedman, "Intracranial arteriovenous malformations: quantitative analysis of magnitude contrast MR angiography versus gradient-echo MR imaging versus conventional angiography," *Radiology*, vol. 196, pp. 187-93., 1995. [20, 21, 23]

A. Nanda, "Controversies in neurosurgery: microsurgery versus radiosurgery for arteriovenous malformations--introduction," *Clin Neurosurg*, vol. 45, pp. 11-12, 1999. [3, 5, 7]

T. Okuyama, K. Saito, A. Hirano, A. Takahashi, T. Inagaki, and S. Inamura, "[Improvement of MRA and 3D-CTA does away with the need for cerebral angiography in many cerebral aneurysm operations]," *No Shinkei Geka - Neurological Surgery*, vol. 26, pp. 607-612, 1998. [7, 8]

M. G. Palmisano, R. L. Galloway, and R. J. Maciunas, "Modified maximum intensity projections for surgical guidance," *Proceedings of SPIE the International Society for Optical Engineering*, vol. 3031, pp. 643-650, 1997. [20]

D. Petereit, M. Mehta, P. Turski, A. Levin, C. Strother, C. Mistretta, R. Mackie, M. Gehring, S. Kubsad, and T. Kinsella, "Treatment of arteriovenous malformations with stereotactic radiosurgery employing both magnetic resonance angiography and standard angiography as a database," *International Journal of Radiation Oncology, Biology, Physics*, vol. 25, pp. 309-313, 1993. [20, 23, 24]

M. H. Phillips, K. A. Frankel, J. T. Lyman, J. I. Fabrikant, and R. P. Levy, "Heavy charged-particle stereotactic radiosurgery: cerebral angiography and CT in the treatment of intracranial vascular malformations," *International Journal of Radiation Oncology, Biology, Physics*, vol. 17, pp. 419-426, 1989. [20, 24]

M. H. Phillips, M. Kessler, F. Y. Chuang, K. A. Frankel, J. T. Lyman, J. I. Fabrikant, and R. P. Levy, "Image correlation of MRI and CT in treatment planning for radiosurgery of intracranial vascular malformations," *International Journal of Radiation Oncology, Biology, Physics*, vol. 20, pp. 881-889, 1991. [20, 24]

G. B. Pike, E. B. Podgorsak, T. M. Peters, C. Pla, A. Olivier, and L. Souhami, "Dose distributions in radiosurgery," *Med Phys*, vol. 17, pp. 296-304, 1990. [50, 115]

G. B. Pike, E. B. Podgorsak, T. M. Peters, C. Pla, and A. Olivier, "Three-dimensional isodose distributions in stereotactic radiosurgery," *Stereotact Funct Neurosurg*, vol. 55, pp. 519-524, 1990. [50, 115]

E. Podgorsak, Podgorsak, MB., "Stereotactic Irradiation," in *The Modern Technology of Radiation Oncology*, J. V. Dyk, Ed. Madison: Medical Physics Publishing, 1999, pp. 1072. [8, 10, 17, 19]

E. B. Podgorsak, A. Olivier, M. Pla, P. Y. Lefebvre, and J. Hazel, "Dynamic stereotactic radiosurgery," *International Journal of Radiation Oncology, Biology, Physics*, vol. 14, pp. 115-126, 1988. [7, 17, 18, 19]

B. E. Pollock, "Stereotactic radiosurgery for arteriovenous malformations," *Neurosurg Clin N Am*, vol. 10, pp. 281-290, 1999. [2, 7, 11]

P. J. Porter, A. Y. Shin, A. S. Detsky, L. Lefaive, and M. C. Wallace, "Surgery versus stereotactic radiosurgery for small, operable cerebral arteriovenous malformations: a clinical and cost comparison," *Neurosurgery*, vol. 41, pp. 757-764; discussion 764-766, 1997. [5, 7]

W. H. Press, Teukolsky, S.A., Vetterling, W.T., Flannery, B.P., *Numerical Recipes in C: The Art of Scientific Computing*, Second ed. Cambridge: Press Syndicate of the University of Cambridge, 1992. [33, 34, 39]

B. K. Rutt, "Vascular System MR Imaging," presented at the 1992 AAPM Summer School on The Physics of MRI, Banff, Alberta, Canada, 1992. [14, 15, 16]

M. C. Schell, Bova, F.J., Larson, D.A., Leavitt, D.D., Lutz, W.R., Podgorsak, E.B., Wu, A., "Stereotactic Radiosurgery," , Woodbury AAPM Report No. 54, June 1995. [9, 83]

G. W. Sherouse, K. Novins, and E. L. Chaney, "Computation of digitally reconstructed radiographs for use in radiotherapy treatment design," *Int J Radiat Oncol Biol Phys*, vol. 18, pp. 651-658, 1990. [40, 43]

R. L. Siddon, "Fast calculation of the exact radiological path for a three-dimensional CT array," *Med Phys*, vol. 12, pp. 252-255, 1985. [40, 42, 43]

J. C. Steffens, J. Link, and M. Heller, "Contrast-enhanced magnetic resonance angiography of the cervical arteries. A review," *Invest Radiol*, vol. 33, pp. 573-577, 1998. [7]

Y. Suzuki and K. Matsumoto, "[Detection of the venous system of the skull base using three-dimensional CT angiography (3D-CTA): utility of the subtemporal approach]," *No Shinkei Geka - Neurological Surgery*, vol. 28, pp. 17-22, 2000. [7]

H. Tanaka, Y. Numaguchi, S. Konno, D. A. Shrier, D. K. Shibata, and U. Patel, "Initial experience with helical CT and 3D reconstruction in therapeutic planning of cerebral AVMs: comparison with 3D time-of-flight MRA and digital subtraction angiography," *Journal of Computer Assisted Tomography*, vol. 21, pp. 811-817, 1997. [7, 8, 13, 16]

K. Takano, H. Utsunomiya, H. Ono, M. Okazaki, and A. Tanaka, "Dynamic contrast-enhanced subtraction MR angiography in intracranial vascular abnormalities," *European Radiology*, vol. 9, pp. 1909-1912, 1999. [7, 8, 20]

P. A. Tercier, P. Coucke, H. Fankhauser, R. O. Mirimanoff, A. Uske, and J. F. Valley, "Transfer of information between angiographic films and CT images: a technique to control the drawing of target volumes," *Radiother Oncol*, vol. 45, pp. 263-269, 1997. [19, 24]

R. C. Wallace and E. C. Bourekas, "Brain arteriovenous malformations," *Neuroimaging Clin N Am*, vol. 8, pp. 383-399, 1998. [3, 6]

L. Walton, A. Hampshire, D. M. Forster, and A. A. Kemeny, "A phantom study to assess the accuracy of stereotactic localization, using T1-weighted magnetic resonance imaging with the Leksell stereotactic system," *Neurosurgery*, vol. 38, pp. 170-176; discussion 176-178, 1996. [14]

D. J. Warren, N. Hoggard, L. Walton, M. W. Radatz, A. A. Kemeny, D. M. Forster, I. D. Wilkinson, and P. D. Griffiths, "Cerebral arteriovenous malformations: comparison of novel magnetic resonance angiographic techniques and conventional catheter angiography," *Neurosurgery*, vol. 48, pp. 973-82; discussion 982-3., 2001. [20, 22, 23]

E. P. Wilkinson, R. Shahidi, B. Wang, D. P. Martin, J. R. Adler, Jr., and G. K. Steinberg, "Remote-rendered 3D CT angiography (3DCTA) as an intraoperative aid in cerebrovascular neurosurgery," *Computer Aided Surgery*, vol. 4, pp. 256-263, 1999. [20]

J. Zhang, M. F. Levesque, C. L. Wilson, R. M. Harper, J. Engel, Jr., R. Lufkin, and E. J. Behnke, "Multimodality imaging of brain structures for stereotactic surgery," *Radiology*, vol. 175, pp. 435-441, 1990. [29]